Fluid-Structure Interaction and Gyroscopic Sensing in Flapping, Flexing Bio-Inspired Wings

Annika Eberle

A dissertation

submitted in partial fulfillment of the

requirements for the degree of

Doctor of Philosophy

University of Washington

2015

Reading Committee:

Per G. Reinhall, Chair

Thomas L. Daniel, Chair

James J. Riley

Program Authorized to Offer Degree:

Mechanical Engineering

University of Washington

Abstract

Fluid-Structure Interaction and Gyroscopic Sensing
in Flapping, Flexing Bio-Inspired Wings

Annika Eberle

Co-Chairs of the Supervisory Committee:

Per G. Reinhall
Department of Mechanical Engineering

Thomas L. Daniel
Department of Biology

Flying animals use the flexibility of their wings to perform impressive aerodynamic maneuvers that are not yet achievable using engineered systems. Since insects do not possess muscles within their wings, these animals must depend on the passive interactions between wing flexibility, wing actuation, and fluid-structure interaction to determine wing shape. As a result, insect wings serve as useful models for understanding the biological principles that govern the design of flexible-winged flyers. This work investigates two key aspects of insect wing flexibility: fluid-structure interaction and gyroscopic sensing. First, to explore the relationship between wing

flexibility and fluid-structure interaction, a 2D wing model was developed by coupling a vortex particle method to a finite element model. For a range of actuation frequencies and flexural stiffnesses that are relevant for insect flight, we show that peak lift and thrust forces coincide with the structural resonance of the system. Second, to understand the mechanism(s) that might allow insect wings to serve as gyroscopic sensors, a 3D structural dynamics model of a flapping, flexing, and rotating wing was created along with a robotic model for validation. We show that the rotation of an insect's body might induce torsion in the wing, which could stimulate an insect's mechanoreceptors and trigger reflexive responses to body rotations. Since halteres, the quintessential examples of biological gyroscopes, are dumbbell-shaped structures that were derived from hind wings, evolution suggests that wings and halteres likely possess similar gyroscopic sensing capabilities. To understand more about gyroscopic sensing in nature, we used analytical and finite element models to re-examine haltere dynamics. Finally, we used quasi-steady aerodynamics and rigid body dynamics to investigate how the aerodynamic and gyroscopic forces differ for halteres and wings. These results provide the first combined experimental and computational evidence that wings may serve as both flight-force actuators and gyroscopic sensors.

TABLE OF CONTENTS

List of Figures iii

List of Tables vii

Chapter 1. Introduction 1

1.1 Fluid-structure interaction 2
1.2 Gyroscopic sensing 3
1.3 Problem Statement 5
1.3.1 Research questions: fluid-structure interaction in insect wings 5
1.3.2 Research questions: gyroscopic sensing in wings and halteres 6

Chapter 2. LITERATURE REVIEW 7

2.1 Aeroelastic studies on wings and fins 7
2.1.1 Airfoil flexibility and propulsive efficiency 7
2.1.2 Hydrodynamic resonance and propulsive efficiency 9
2.1.3 Inertial-elastic forces and insect wing deformation 9
2.2 Gyroscopic sensing in insect flight 10
2.2.1 Insect halteres as gyroscopic sensors 10
2.2.2 Antennae as gyroscopic sensors 12
2.2.3 Insect wings as gyroscopic sensors 12

Chapter 3. FLUID-STRUCTURE INTERACTION IN INSECT WINGS 14

3.1 Abstract 14
3.2 Introduction 15
3.3 Methodology 17
3.3.1 Finite element model and mechanical parameters 17
3.3.2 Ideal flow model of the fluid 19
3.3.3 Coupled fluid–solid model 22
3.3.4 Non-dimensional parameters 22
3.3.5 Model validation, convergence testing, and simulations 24
3.4 Results and discussion 26
3.4.1 Coupled model results: frequency versus stiffness 26
3.4.2 Coupled model results: frequency versus phase 27
3.4.3 Relative importance of fluid loading 28
3.4.4 Importance of structural resonance 31
3.5 Conclusions 32
3.6 Acknowledgments 34

Chapter 4. INSECT WINGS AS GYROSCOPIC SENSORS 35

4.1 Abstract 35
4.2 Introduction 36
4.3 Materials and methods 39
4.3.1 Computational model of insect wing structural dynamics 39

4.3.2 Robotically actuated model with position tracking 45
4.3.3 Robotically actuated model with strain measurement 46
4.4 Results 47
4.4.1 Torsional deformation emerges in the computational model 47
4.4.2 Wing tip deformation reveals torsion in both computational and physical models .. 51
4.4.3 Torsion is reflected in wing strain 52
4.5 Discussion 57
4.5.1 Insect wings undergo torsion during body rotations 57
4.5.2 Changes in wing strain could stimulate mechanosensors 58
4.6 Conclusions 59
4.7 Acknowledgements 60
4.8 Data Accessibility 60

Chapter 5. HALTERES AS TORSIONAL GYROSCOPES 61

5.1 Introduction 61
5.2 Materials and Methods 63
5.2.1 Analytical Model in MATLAB 64
5.2.2 Finite Element Model in COMSOL 67
5.3 Results 69
5.3.1 Haltere model undergoes torsion due to spatial gradient in Coriolis force 69
5.3.2 Haltere torsion depends largely on the mass distribution of the bulb 71
5.3.3 Gyroscopic forces induce changes in length-wise normal strain 73
5.4 Discussion and Conclusions 75
5.4.1 Halteres likely undergo torsion when they are flapped and rotated 75
5.4.2 Sensitivity to mass distribution has implications for haltere evolution 75
5.5 Acknowledgements 76

Chapter 6. AERODYNAMIC VS. GYROSCOPIC FORCES ON WINGS AND HALTERES . 77

6.1 Introduction 77
6.2 Materials and Methods 78
6.2.1 Wing model 79
6.2.2 Haltere model 81
6.3 Results and Discussion 82
6.3.1 Ratio of Coriolis to aerodynamic moments on wings increases with span and decreases with flapping frequency 83
6.3.2 Coriolis to aerodynamic moments on wings increases with angular velocity 85
6.3.3 Ratio of Coriolis to aerodynamic moments on halteres is larger than for wings 85
6.4 Conclusions 86

Chapter 7. Conclusions 88

REFERENCES 92

APPENDIX 1: Supplementary Material for Fluid-Structure Interaction Model 100

APPENDIX 2: Supplementary Material for Flapping, Rotating Wing Model 115

APPENDIX 3: Supplementary Material for Low-Order Haltere Model 132

LIST OF FIGURES

Figure 1.1. Chordwise flexural stiffness versus chord length 3
Figure 1.2. Anatomy of an insect haltere 4
Figure 1.3. Anatomy of an insect wing 4
Figure 2.1. Coefficient of thrust (left) and propulsive efficiency (right) 8
Figure 2.2. Propulsive efficiency of an elliptical fin in water versus Strouhal number 9
Figure 2.3. Locations of haltere campaniform sensilla magnified. 11
Figure 3.1. A diagram of the fluid-structure interaction model setup 18
Figure 3.2. The relative tip displacement (ξ), coefficient of lift (C_l), and coefficient of thrust (C_t) plotted versus convective time, τ 24
Figure 3.3. The log10 of the effective stiffness (R) plotted against the reduced frequency (k) for the relative tip displacement (ξ), coefficient of lift (C_l), and coefficient of thrust (C_t) as phase of actuation varies from (a) 0 rad to (b) $\pi/2$ rad to (c) π rad 27
Figure 3.4. The heave-pitch actuation phase (φ) plotted against the reduced frequency (k) for the relative tip displacement (ξ), coefficient of lift (C_l), and coefficient of thrust (C_t) as effective stiffness varies from (a) 378 to (b) 1840 to (c) 3780 29
Figure 3.5. The $\log_{10}$ of the effective stiffness (R) plotted against the reduced frequency (k) for the displacement ratio (Δ), lift ratio (L^*), and thrust ratio (T^*) as phase of actuation varies from (a) 0 rad to (b) $\pi/2$ rad to (c) π rad 30
Figure 3.6. The heave-pitch actuation phase (φ) plotted against the reduced frequency (k) for the displacement ratio (Δ), lift ratio (L^*), and thrust ratio (T^*), as effective stiffness varies from (a) 378 to (b) 1840 to (c) 3780 31
Figure 4.1. Insect halteres and wings possess campaniform sensilla 37
Figure 4.2. Diagram of the computational wing model 40
Figure 4.3. Diagram of the robotically actuated wing setup 46
Figure 4.4. The displacements of the left and right wingtips of computational model. .. 48
Figure 4.5. Torsion emerges in the computational model 50

Figure 4.6. The difference between the displacement of the left and right endpoints of the wing, ΔD, versus time, t, for flapping alone and flapping and rotating with periodic angular velocity 54
Figure 4.7. The shear strain at the quarter span along the mid chord ε_{xy} versus time, t, for flapping alone and flapping and rotating with periodic angular velocity 55
Figure 4.8. The normal strain along the span wise direction, ε_{yy}, on either side of the wing's chord (lift side - solid; right side - dashed) near the base of a model wing versus time, t, for flapping alone and flapping and rotating with periodic angular velocity. 56
Figure 5.1. Some insect species possess halteres, dumbbell-shaped mechanosensory structures that are used to detect body dynamics. 62
Figure 5.2. Diagram of our haltere model (a) with three types of mass distributions: a single point mass (b), a symmetric distribution of eccentric masses (c), and an asymmetric distribution of eccentric masses (d) 64
Figure 5.3. COMSOL model of a haltere 68
Figure 5.4. Out-of-plane bending (blue lines) and torsion angles (green and red lines) for haltere flapping under constant body rotation about the z-axis. 70
Figure 5.5. Haltere torsion is induced by a spatial gradient in the Coriolis force 71
Figure 5.6. Out-of-plane bending (solid line in a) and torsion angles (dash-dot line in a) from the symmetric COMSOL model 72
Figure 5.7. The length-wise normal strain (strain XX) measured at one location on the side of the haltere 74
Figure 6.1. Program diagram for simplified model of inertial and aerodynamic forces on an insect wing and haltere 79
Figure 6.2. Comparison of inertial and aerodynamic moments generated by rigid moth- and fly-like wings 83
Figure 6.3. The ratio of the amplitudes of the Coriolis and aerodynamic moments for wings varies with wingspan and flapping frequency, f_{flap} 84
Figure 6.4. The ratio of the amplitudes of the Coriolis and aerodynamic moments for wings varies with wingspan and angular velocity, ω_c 85

Figure 6.5. The ratio of the amplitudes of the Coriolis and aerodynamic moments for halteres varies with length and flapping frequency, f_{flap} 86
Figure S1. Program diagram for coupled fluid-solid model. 101
Figure S2. Experimental setup used to determine wing damping..... 103
Figure S3. Time-series plot of the velocity of an excised *Manduca sexta* wing tip in response to a slight perturbation at the wing tip (recorded using a laser vibrometer).103
Figure S4. Coefficient of lift of rigid inclined plate generated by model (dashed) versus theoretical value (solid) for several angles of attack..... 104
Figure S5. Comparison between lift computed by the fluid model alone and lift from Theodorsen's model for a plate being pitched and heaved under small amplitudes about the leading edge. 106
Figure S6. Differences in the coupled coefficient of lift, C_l, as the velocity field smoothing parameter, d, varies for three frequencies of oscillation 107
Figure S7. Differences in the lift ratio, L^*, as the velocity field smoothing parameter, d, varies for three frequencies of oscillation 108
Figure S8. Tip displacement of the model and the analytical solution for a beam undergoing vertical ground motions (heaving) at the leading edge..... 110
Figure S9. Comparison between tip displacement as computed by the model (dashed red) and by the analytical solution (solid black) for a beam undergoing vertical ground motions (heaving) at the leading edge near the resonant frequency..... 111
Figure S10. Relative error in the tip displacement of the solid model (as compared to the smallest time step) varies as time step size changes for a plate being pitched and heaved about the leading edge at three frequencies of oscillation..... 112
Figure S11. Relative error in the tip displacement of the solid model varies with element size as time step changed linearly with element size 113
Figure S12. Relative error in the coefficient of lift, C_l, as computed with the fluid model at varying time step sizes for a plate being pitched and heaved about the leading edge at three frequencies of oscillation..... 114
Figure S13. Computing the difference of two signals in the frequency domain 120

Figure S14. The difference between the displacement of the left (D_L) and right (D_R) endpoints of the wing, ΔD, versus time, t, for flapping alone (a,d) and flapping and rotating with periodic angular velocity (b,e)..... 122

Figure S15. The shear strain at the quarter span along the mid chord ε_{xy} versus time, t, for flapping alone (a,d) and flapping and rotating with periodic angular velocity (b,e) 123

Figure S16. The normal strain along the span wise direction, ε_{yy}, on either side of the wing's chord (lift side - solid; right side - dashed) near the base of a model wing versus time, t, for flapping alone (a,d) and flapping and rotating with periodic angular velocity (b,e) 124

Figure S17. Computational results for the difference in the amplitudes of the FFTs for shear strain at the quarter span along the mid chord ε_{xy} between flapping alone and flapping and rotating with periodic angular velocity 125

Figure S18. Spatiotemporal patterns of strain emerge in the computational model when the wing is flapped 128

Figure S19. Spatiotemporal patterns of strain emerge in the computational model when the wing is flapped under constant angular velocity of 800°/s about the z-axis 129

Figure S20. Spatiotemporal patterns of strain emerge in the computational model when the wing is flapped under periodic angular velocity about the z-axis 130

Figure S21. Differences between the spatiotemporal patterns of strain while the wing is flapped versus flapped under periodic angular velocity about the z-axis 131

Figure S22. Model validation: out-of-plane displacement, φ, versus input flapping angle, γ, as computed using our haltere model (solid) versus results from Thompson *et al* (2008) (dashed) 134

Figure S23. Convergence of COMSOL haltere model as reported by the relative difference in the torsion displacements of the haltere bulb, |z| 135

Figure S24. The torsion angle amplitude, |Y(f)|, versus frequency for the COMSOL haltere model under flapping alone. 135

LIST OF TABLES

Table 3.1. Non-dimensional parameters of interest 23
Table 4.1. List of symbols 41

ACKNOWLEDGEMENTS

The work described in this dissertation would not have been possible without the support of my collaborators and my family and friends. First, I would like to acknowledge my committee co-chairs, Dr. Per Reinhall and Dr. Thomas Daniel, for their excellent guidance and mentorship. I would also like to thank the other members of my committee, Dr. James Riley, Dr. Alberto Aliseda, and Dr. Christine Luscombe, for taking the time to review my work and for providing insightful comments and discussion.

I am also grateful for the many outstanding professors and scholars that I have learned from at Harvey Mudd College and the University of Washington. I would like to thank Dr. Lori Bassman for first introducing me to engineering research as an undergraduate and for supporting me in applying to graduate school. I am also very grateful to Dr. Minoru Taya and Dr. Nate Sniadecki who share my passion for biomechanics and bio-inspired design and who first encouraged me to come to the University of Washington. I would also like to thank Dr. Minrou Taya and Dr. Liz Van Volkenburgh for their support on my first graduate research project studying plant tendrils. It has been an honor to learn from the entire distinguished faculty at the University of Washington and I am especially grateful to Dr. Thomas Daniel for introducing me to comparative biomechanics and for inviting me to work in his lab.

This work would not have been possible without the support of my family and friends. I would like to thank all of the current and former Daniel Lab, especially Brad Dickerson for sharing his knowledge of biology with me. I would also like to acknowledge Dr. Steve Brunton and Dr. Bing Brunton for insightful comments and discussions and for being excellent role models. I would also like to thank my husband, Mark, my sister, Louisa, and my parents, Kim and Brian, for all of their patience, support, and encouragement.

Finally, it is with profound admiration that I thank the many scientists and engineers that have preceded me in this field. I am grateful for their many insights and discoveries and I am excited to build upon their work.

DEDICATION

I dedicate this work to my husband, Mark.

Chapter 1. INTRODUCTION

Human-engineered flying systems traditionally use rigid wings for lift generation because flexible wings can be difficult to design and control. However, animals regularly use flexible wings to propel themselves. In recent years, many researchers have determined that animals can achieve improved performance and control with flexible wings. While some animals actively control wing shape via wing muscles, insects do not have any muscles beyond the base of their wings so their wing shape is determined passively. This work focuses on the latter, where wing deformation is determined passively and emerges from the flexibility of the wing, the actuation parameters at the root, and the fluid-structure interaction of the wing with air.

By investigating the biological principles that govern wing flexibility in a natural system, like an insect, I hope to inspire novel engineering solutions for applications in micro air vehicles and wind energy. In turn, by using engineering tools to explore biological systems, this work also increases our understanding of biology.

My research comprises three main projects related to the flexibility of flapping, flexing bio-inspired wings: 1) fluid-structure interaction in insect wings, 2) gyroscopic sensing in insect wings, and 3) inertial sensing in halteres, gyroscopic sensory organs derived from wings. First, I examine the extent to which the fluid forces (*i.e.* air resistance) acting on a model insect wing change the shape of the wing and thereby modify the flight forces it develops (see Chapter 3). Second, I use a bio-inspired insect wing to explore whether insects can monitor the structural dynamics of the wing to sense body rotations during a turning maneuver (see Chapter 4). Finally, I explore the implications of the evolutionary sensing capabilities of the prototypical biological gyroscope, the haltere (Chapters 5 and 6).

The dynamics of elastic deformation are key to all of these projects. In the case of wings, elastic deformations provide advantages for flight performance but they may also be sensed and can potentially be used for flight control. For halteres, on the other hand, elastic deformations are primarily used for sensing capabilities and have little impact on flight forces.

1.1 FLUID-STRUCTURE INTERACTION

The deformation of natural wings results from the interaction between forces imposed by the fluid surrounding the wing, the wing's material properties (*e.g.* mass and stiffness distributions), and the actuation of the wing. When an animal, such as an insect, does not possess any intrinsic wing muscles, these forces passively interact to produce the spatial and temporal patterns of wing movement and shape. Inertial forces result from the resistance of the wing to changes in its velocity; aerodynamic forces result from the fluid surrounding the wing; and elastic forces govern the deformation of the solid wing and connecting structure that is subject to these body and surface forces. The complex interactions between these aerodynamic and inertial/elastic forces essentially define the field of aeroelasticity (Bisplinghoff 1962). However, we do not yet have a clear understanding of the principles that govern the mechanical design of flexible wings for the dual role of efficient propulsion and inertial sensing. This issue is a primary motivation for the research undertaken here.

The coupling of the inertial/elastic forces with the aerodynamic forces can in some circumstances lead to an instability that can destroy the structure (*e.g.* flutter), much like the famous example of the Tacoma Narrows Bridge (Bisplinghoff *et al* 1996). Thus, understanding the aeroelastic nature of animal wings may not only inform the biological principles behind wing compliance but might also provide design criteria that can be applied to improve engineered systems. However, since insects have different wing flexibilities (see figure 1.1) and actuation frequencies, it can be difficult to extract the biological principles that govern the use of flexible wings in insect flight.

My research on fluid-structure interactions focuses on how the structural and fluid dynamics of and around a wing change with actuation frequency and wing flexibility. Through the development and analysis of a computational model of a two-dimensional wing section, I found that fluid forces do not dramatically change wing shape and thereby modify flight forces (*i.e.* wing deformation is dominated by the actuation of the wing base, not the fluid loads imposed upon it). This result indicates that the fluid and structural dynamics of the wing can be modeled separately, which could result in significant computational savings when developing models of flexible wing designs.

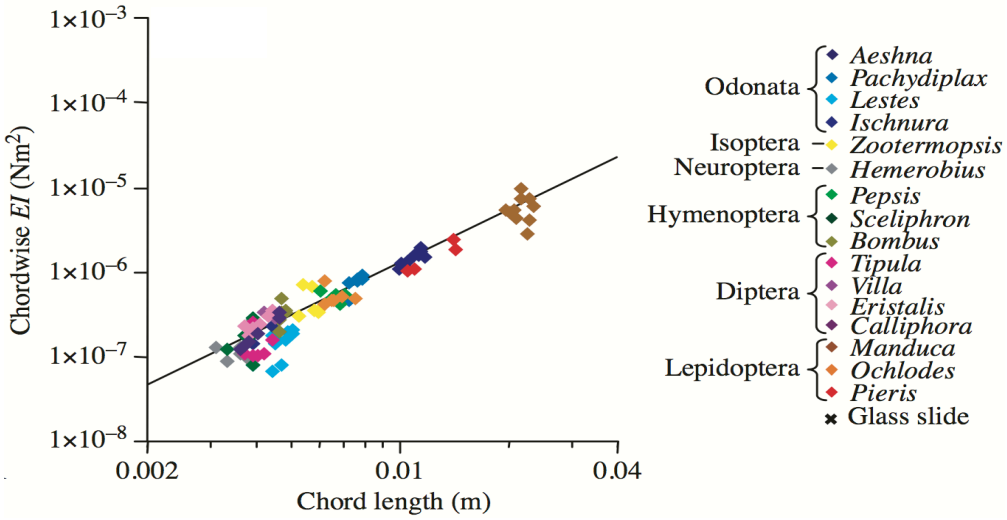

Figure 1.1. Chordwise flexural stiffness versus chord length for 16 insect species (from Combes and Daniel 2003c).

1.2 GYROSCOPIC SENSING

Insects perform very fast rotational maneuvers during flight (Hedrick 2009) and they are often not able to use their visual system to detect these rotations because it reacts too slowly (Land and Collett 1974, Sandeman and Markl 1980, Fuller *et al* 2014b). While an animal's visual system may be tuned to perform different tasks, these adaptations often require tradeoffs between spatial and temporal resolution (Theobald *et al* 2010). In order to supplement their visual system, some insects use modified hind wing structures called halteres (figure 1.2). During quick turns, the animals use these dumbbell-shaped structures to sense the gyroscopic forces that are imposed on them (Pringle 1948, Nalbach 1993, Fox and Daniel 2008, Thompson *et al* 2008). By moving these structures in a rotating reference frame, the halteres experience gyroscopic forces that relate to the rotation rate of the insect's body: a Coriolis force (*i.e.* a force that acts tangentially to the rotation) and a centrifugal force (*i.e.* a force that acts radially and pulls towards the center of the rotation). Insects with halteres are thought to capture the information carried by these forces by sensing changes in haltere curvature (Pringle 1948, Nalbach 1993, Thompson *et al* 2008, Fox *et al* 2010).

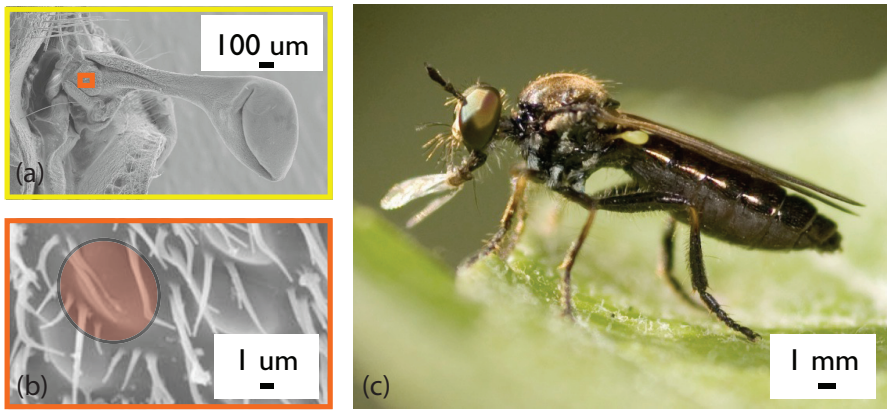

Figure 1.2. Anatomy of an insect haltere: (a) SEM image of a robber fly haltere by Brad Dickerson, (b) SEM image of a crane fly campaniform sensilla from Fox and Daniel 2008, and (c) photograph of a robber fly with yellow haltere by Armin Hinterwirth.

Halteres, however, are specific to only two insect orders. Thus, we ask: how might other insects sense their body rotations? Since halteres evolved from insect wings, it is not surprising that wings have similar sensory organs to halteres (figure 1.3; Dickerson *et al* 2014). Given that halteres and wings both 1) experience gyroscopic forces, and 2) possess mechanosensing capabilities, we propose the novel hypothesis that wings could potentially act as gyroscopic sensors.

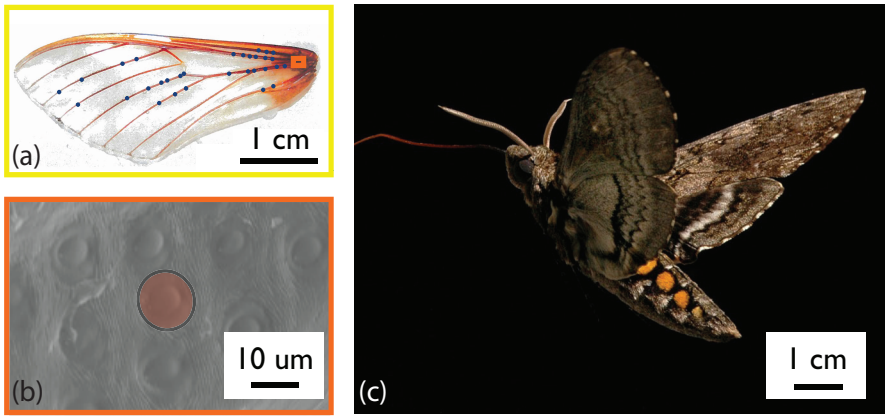

Figure 1.3. Anatomy of an insect wing: (a) diagram by Brad Dickerson showing locations of campaniform sensilla on the dorsal side of hawkmoth wings, (b) SEM image of campaniform sensilla at the base of a hawkmoth wing, and (c) photograph of a hawkmoth by Armin Hinterwirth.

In fact, recent work using behavioral, elctrophysiological, and anatomical evidence suggests that wings might indeed serve as gyroscopic sensors (Dickerson *et al* 2014). However, would detecting changes in the structural dynamics of a flapping, rotating wing alone be enough for an insect to detect its body rotations?

The gyroscopic sensing aspect of my research focuses on understanding how the dynamics of wing deformations change during rotational maneuvers and then examining how these changes might be used to inform an insect about its body dynamics. Results from experimental and computational models indicate that when wings both flap and rotate, they exhibit a new dynamic mode: torsion. This mode results in spatiotemporal changes in wing strain, which could be monitored by the wing's mechanosensors and thereby used for flight control.

1.3 Problem Statement

My research draws on engineering methods to develop general principles for understanding how the fluid and structural dynamics of insect wings change with wing flexibility and thereby impact flight performance and sensing capabilities. I am also interested in understanding the mechanism that may have driven the evolution of gyroscopic sensing capabilities in insect halteres. Here I provide the research questions that I address in each of these areas.

1.3.1 *Research questions: fluid-structure interaction in insect wings (Chapter 3)*

In Chapter 3, I address two key questions related to how fluid-structure interactions in insect wings change are affected by changes in the actuation frequency, phase of actuation between pitch and heave, and flexibility of the wing:

1) How does flight performance, as measured by coefficients of lift and thrust, vary with frequency and phase of actuation, along with wing stiffness?

2) Over a range of flapping frequencies, phases of pitch-heave actuation, and wing flexibilities, how much does aerodynamic forcing cause the wing to bend and thereby affect flight forces?

My purpose here is to identify parameter regions in which coupling may not play a crucial role in developing flight forces. Since the parameter space that we desire to explore is quite

large, I seek to design an efficient algorithm and approach to allow further exploration of this problem. Ultimately, this model will inform how the mechanical design of wings can be tuned for effective force generation (or wind energy extraction).

1.3.2 *Research questions: gyroscopic sensing in wings and halteres (Chapters 4-5)*

In Chapters 4-5, I explore three questions relating to how the flexibility of insect wings and halteres might be used to inform the animal about its body dynamics:

1) How do the structural dynamics of wings change when they are subject to body rotations?
2) How do the gyroscopic dynamics of a wing compare to those of a haltere?
3) How does the mass distribution of halteres and wings impact their ability to act as biological gyroscopes?

In the case of gyroscopic sensing, my purpose is 1) to identify whether the signals generated by the variation in wing dynamics are large enough to be detected by the wings' mechanosensors, and 2) to compare the gyroscopic dynamics of wings and halteres. In order to study these issues, I created computational models of a flapping, rotating wings and halteres using low-order numerical models and more complex finite element models. I also verified the wing models by developing a robotically actuated experimental setup. The goals of this work are 1) to identify whether halteres and wings might use a similar sensory mechanism as would be suggested by their evolutionary history, and 2) to determine if wing and haltere strain might be used to detect angular velocity and thereby be used for flight control.

Chapter 2. LITERATURE REVIEW

Since fluid-structure interaction and gyroscopic sensing are two related, but disparate, domains, I structured the literature review accordingly. The first section focuses on those aspects of wing aeroelasticity that are most relevant for the fluid-structure interaction component of my work. The second section covers prior work on gyroscopic sensing in insect wings and halteres.

2.1 AEROELASTIC STUDIES ON WINGS AND FINS

While some of the first studies of the aerodynamics of swimming and flying animals were performed in the early 1970s (Wu 1971, Weis-Fogh 1973, Lighthill 1973), we still do not completely understand the biological principles that govern the design of compliant wings and fins. In recent years, the field of biologically oriented aeroelasticity has expanded, and active research areas can be generally broken down into three areas: experimental investigations of live animals, robotic actuations of engineered structures, and computational or analytical modeling. Within these three areas of research, several phenomena have been shown to be important for the operation of flexible wings and fins. First, flexible wings and fins have been shown to increase performance over their rigid counterparts. Second, inertial forces appear to dominate the fluid forces in the case of insect flight. And, third, structural and hydrodynamic resonances have been shown to have a large impact on flight performance of wings and fins, respectively.

2.1.1 *Airfoil flexibility and propulsive efficiency*

Wing flexibility can profoundly affect the flight performance of natural (Mountcastle and Daniel 2009, 2010, Young *et al* 2009, Zhao *et al* 2010, Lee *et al* 2011, Nakata and Liu 2012) and engineered systems (Heathcote and Gursul 2007, Alben 2008, Lua *et al* 2010, Stanford *et al* 2011, Barannyk *et al* 2012, Leftwich *et al* 2012, Alben *et al* 2012). For example, through an experimental study of the hawkmoth *Manduca sexta*, Mountcastle and Daniel (2009) showed that a flexible wing was able to generate more lift-favorable momentum flux than a stiff wing. In addition, Barannyk *et al* 2012 showed that flexible airfoils outperform rigid ones (figure 2.1). In addition, several studies have shown that flight performance can be optimized at certain levels of flexibility, beyond which flight forces and/or efficiency decrease (Heathcote and Gursul 2007, Alben 2008, Lua *et al* 2010, Lee *et al* 2012, Nakata and Liu 2012).

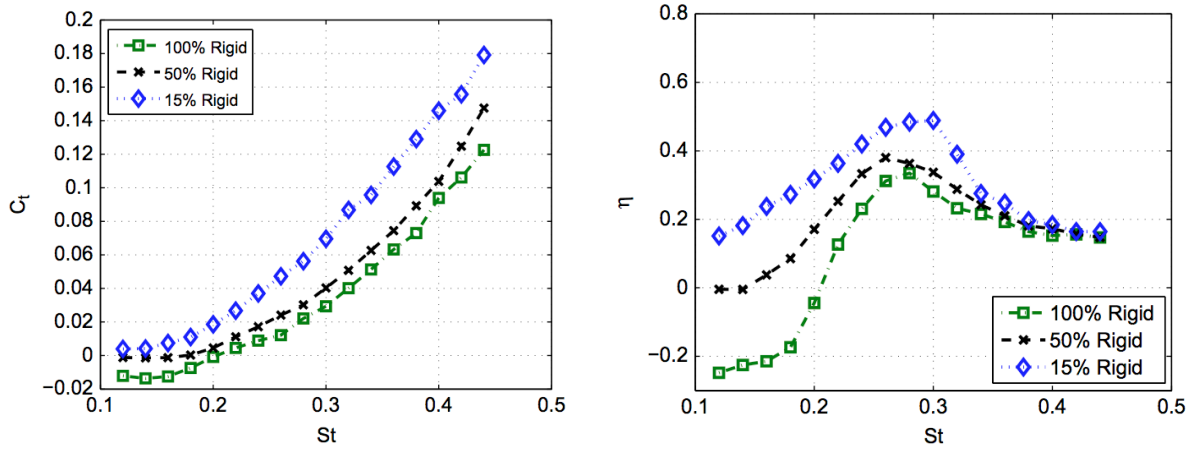

Figure 2.1. Coefficient of thrust (left) and propulsive efficiency (right) versus Strouhal number for three plates of varying flexibility oscillating in water (from Barannyk *et al* 2012).

Several studies have also showed that the optimal frequency for maximizing the propulsive efficiency of flexible wings is 0.33 to 0.6 of the natural frequency of the wing (Zhu 2007, Vanella *et al* 2009, Yin and Luo 2010, Ramananarivo *et al* 2011, Kang *et al* 2011, Michelin and Smith 2009). In addition, Kang *et al* (2011) derived several scaling laws that govern the generation of propulsive forces and found that they are maximized at the resonant frequency of the wing.

Since the flexibility of a wing can increase flight performance, it is not surprising that aspects of flight control, like phase of actuation and angle of attack, can be tuned to achieve optimum flight performance. For example, Zhao *et al* (2010) performed an experimental investigation of flapping wings with several different flexibilities and showed that the angle of attack can be tuned to achieve optimum efficiency for several wing flexibilities. In addition, Mountcastle and Daniel (2010) performed a de-coupled analysis of the aerodynamics of a 2D wing and found that phase of wing actuation could be used to tune flight forces developed by a flexible, flapping wing. However, these studies were limited to a single frequency of actuation and explored a limited number of wing flexibilities.

2.1.2 *Hydrodynamic resonance and propulsive efficiency*

The ratio of the fluid density to solid density is about three orders of magnitude larger for fins in water as compared to wings in air. As a result, the relationship between flexibility and performance differs for flying and swimming animals. While fin flexibility is important to propulsive performance of fish in water (Lauder and Madden 2007), the hydrodynamic resonance seems to dominate over the structural resonance for the generation of maximum swimming forces on fins in water (Alben 2008, Barannyk *et al* 2012, Leftwich *et al* 2012, Moored *et al* 2012). However, when the hydrodynamic and structural resonances align, the propulsive efficiency of a flexible foil is maximized in water (figure 2.2; Moored *et al* 2012).

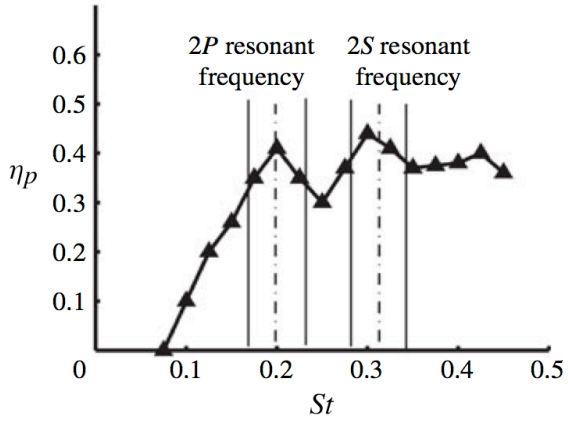

Figure 2.2. Propulsive efficiency of an elliptical fin in water versus Strouhal number (from Moored *et al* 2012). Dashed lines denote resonant frequencies found via linear stability analysis.

2.1.3 *Inertial-elastic forces and insect wing deformation*

Daniel and Combes (2002) used an analytical approach to show that the inertial-elastic forces generated by a flapping, flexible wing are much larger than the fluid forces experienced by the wing. In addition, Fry *et al* (2003) used an experimental approach to verify that inertial forces dominate flight maneuvers in flies. These results demonstrate that, at least in some cases, the dynamics of the structure and the fluid could be modeled separately (*e.g.* without aeroelastic feedback). However, since these approaches were either based on a limited number of analytical solutions (Daniel and Combes 2002) or used experimental techniques that would make parameter

exploration difficult (Fry *et al* 2003), these studies were not able to explore a larger parameter space.

2.2 GYROSCOPIC SENSING IN INSECT FLIGHT

Pringle (1948) was one of the first researchers to describe a mechanism that would allow insects to use their mechanosensory systems to detect gyroscopic forces. By combining experimental measurements with analytical models, Pringle showed that dipteran halteres could detect small Coriolis forces using directionally sensitive mechanosensory cells, called campaniform sensilla. Since then research on gyroscopic sensing in insects has primarily focused on two sensory organs: halteres and antennae. However, since halteres are derived from wings, evolution would suggest that wings themselves might possess at least primordial gyroscopic sensing capabilities.

2.2.1 *Insect halteres as gyroscopic sensors*

Halteres, which are derived from an insect's hind wings, are small dumbbell-shaped structures that extend from the thorax of some insects. Insects that possess halteres flap both their wings and their halteres simultaneously by imposing musculoskeletal forcing via the thorax. When insects rotate their bodies while their halteres are flapping, the halteres encounter rotational, or gyroscopic, forces. Derham (1713) was the first to propose that halteres, which he called Poises, serve to stabilize flies:

> For the keeping the Body steady and upright in Flight, it generally holds true, (if I mistake not,) that all bipennated Insects have *Poises* joyn'd to the Body, under the hinder Part of their Wings; but such as have four Wings, or Wings with *Elytra*, none. If one of the Poises, or one of the lesser auxiliary Wings be cut off, the Insect will fly as if one Side overbalanced the other, until it falleth on the Ground; so if both be cut off, they will fly aukwardly, and unsteadily, manifesting the Defect of some necessary part. These *Poises*, or *Pointells* are, for the most Part, little Balls, set at the Top of a slender Stalk, which they can move every Way at pleasure. In some they stand alone, in others, (as in the whole *Flesh-Fly* Tribe,) they have little Covers or Shields, under which they lie and move. The Use, no doubt of these *Poises* and *secondary* lesser Wings is to poise the Body, and to obviate all the Vacillations thereof in Flight; serving to the Insect as the long Pole, laden at the Ends with Lead, doth the *Ropedancer*.

Even in the 18th century, Derham was able to observe the behavioral consequences of losing a haltere and he correctly concluded that the nature of the haltere's design must allow these structures to stabilize insect flight.

Since the 1700s, several biomechanical, behavioral, and neurological studies have shown that halteres respond to rotational perturbations by detecting small out-of-plane displacements (Fraenkel and Pringle 1938, Pringle 1948, Nalbach 1993, Fox and Daniel 2008, Thompson *et al* 2008). Insects detect these small out-of-plane deformations using mechanoreceptors, called campaniform sensilla, located at the base of each haltere (figure 2.3).

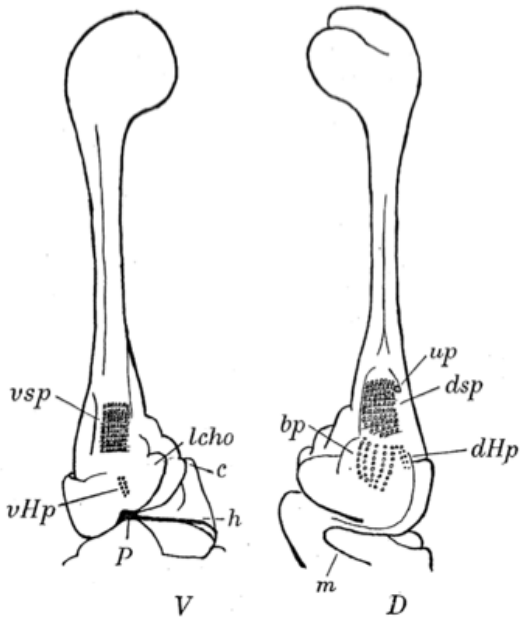

Figure 2.3. Locations of haltere campaniform sensilla magnified at 100x. Labels V and D denote the ventral and dorsal sides, respectively (Pringle 1948).

Campaniform sensilla are small dome-shaped structures that are innervated by a single neuron. When the campaniform sensilla are bent, they open an ion channel, which sends a signal to the animal's central nervous system. Sandeman and Markl (1980) showed that campaniform sensilla of flies (*Calliphora*) are capable of sensing perturbations to within 3 ms, which is about ten times faster than their visual system (Land and Collett 1974).

2.2.2 *Antennae as gyroscopic sensors*

Unlike halteres, which are specific to two insect orders (Diptera and Strepsiptera), all winged insects have a pair of antennae. As a result, some researchers have suggested that antennae might serve a similar sensory function to halteres. Using models, neurophysiological data, and behavioral experiments Sane *et al* (2007) showed that the basal segments of the antennae of the hawkmoth, *Manduca sexta*, are sensitive enough to detect small out-of-plane deformations that the antennae would undergo during rotations. Sane *et al* (2007) also showed that moths that had their antennae removed were much less stable (collided with walls more often) than moths with intact antennae. Thus, they concluded that the antennae of *Manduca sexta* are capable of sensing Coriolis forces and are essential for flight stability. Other work by Hinterworth and Daniel (2010) showed that while *Manduca sexta* respond to both visual and mechanical rotational perturbations, the mechanical response depends on the presence of an antennal mechanosensor, called the flagellum.

However, several researchers have questioned whether the magnitude of rotational perturbations that the antennae experience would be sufficient for these animals to detect. Taylor and Krapp (2007) showed that the absolute magnitude of the Coriolis forces on antennae are at least two orders of magnitude smaller than the forces experienced by halteres. As a result, it is uncertain whether these small oscillations would significantly deform the antennae, thereby allowing them to serve as gyroscopic sensors.

2.2.3 *Insect wings as gyroscopic sensors*

Since antennae may not be sufficient for gyroscopic control and halteres are specific to only two insect orders, what other structures might an insect use to detect body dynamics during flight? Since halteres are derived from wings and wings have the same sensory structures as halteres (figures 1.2 and 1.3; Dickerson *et al* 2014), evolution suggests that wings themselves may possess rudimentary versions of the sensory mechanisms that gave rise to gyroscopic sensing in halteres. As a result, we propose that wings could serve a similar sensory function to halteres.

Previous work on the concept of wings serving as gyroscopic sensors focused on anatomical, behavioral and electrophysiological studies carried out by Dickerson *et al* (2014). They showed that campaniform sensilla are not only present on the wings of the hawkmoth,

Manduca sexta, but also that the neurons innervating the campaniform sensilla on the wings show spike-timing similar to the neurons innervating the mechanosensors on halteres. Dickerson *et al* (2014) also demonstrated, via behavioral experiments on tethered hawkmoths, that the animals exhibit abdominal responses when their wings are subject to mechanical perturbations. The abdominal responses to mechanical wing perturbations were similar to other experiments done with visual and inertial pitch stimuli. As a result, insect wings might indeed serve as inertial sensors. However, Dickerson *et al* (2014) did not indicate how the mechanics of the wing might function to allow for such sensing capabilities.

Chapter 3. FLUID-STRUCTURE INTERACTION IN INSECT WINGS

As described in Chapter 1, the first goal of my work was to understand how the aerodynamic forces on insect wings change the shape of the wing thereby modify flight forces. In order to quantify the relative importance of fluid-structure interaction, my collaborators and I developed a computational model to explore how flight performance varied with wing oscillation dynamics and wing flexibility. This model allowed us to explore how a large variety of wing flexibilities and actuation dynamics impact the development of flight forces.

Our results show that the deformation of a flapping, flexing insect wing is dominated by the actuation of the wing base, rather than by the fluid loads imposed upon it. By investigating the biological principles that govern insect flight, we solidified a useful computational tool for engineers: the fluid and solid can be modeled separately for moderately large insect wings. In turn, by leveraging engineering tools, we revealed an interesting biological principle: the frequency and phase of wing actuation have considerable control authority over flight forces. This work was published in *Bioinspiration and Biomimetics* in May of 2014 (Eberle *et al* 2014).

3.1 ABSTRACT

Insect wings deform significantly during flight. As a result, wings act as aeroelastic structures wherein both the driving motion of the structure and the aerodynamic loading of the surrounding fluid potentially interact to modify wing shape. We explore two key issues associated with the design of compliant wings: over a range of driving frequencies and phases of pitch-heave actuation, how does wing stiffness influence (1) the lift and thrust generated and (2) the relative importance of fluid loading on the shape of the wing? In order to examine a wide range of parameters relevant to insect flight, we develop a computationally efficient, two-dimensional model that couples point vortex methods for fluid force computations with structural finite

element methods to model the fluid–structure interaction of a wing in air. We vary the actuation frequency, phase of actuation, and flexural stiffness over a range that encompasses values measured for a number of insect taxa (10–100 Hz; 0-π rad; 10^{-7}–10^{-5} Nm^2). We show that the coefficients of lift and thrust are maximized at the first and second structural resonant frequencies of the system. We also show that even in regions of structural resonance, fluid loading never contributes more than 20% to the development of flight forces.

3.2 INTRODUCTION

Flying animals perform phenomenal maneuvers using flexible wings. While the deformation of some animal wings (*e.g.* bird and bat wings) can be actively controlled via wing musculature, insect wings are entirely passive structures. Indeed, with flight muscles constrained to the wing base and thorax, insects have very little ability to actively control wing shape (Wootton 1992). As such, the passive mechanical properties of insect wings (*e.g.* stiffness, damping, and inertia), which can vary widely, determine how the wings respond to aerodynamic loads and actuation torques.

Flexural stiffness—a measure of wing compliance—varies by more than two orders of magnitude (*i.e.* chord-wise stiffness varies from 10^{-7} to 10^{-5} Nm^2) over a number of insect taxa (Combes and Daniel 2003c). In addition, actuation of the wing base is composed of pitching, sweeping, and heaving motions at certain species-specific frequencies (10–1000 Hz) with variable phases of actuation between these directions of motion (Greenewalt 1962). Given the lack of intrinsic musculature and the wide range of mechanical characteristics and dynamic controls, insect wings serve as ideal models for inspiring passive wing controls and for improving the performance of flexible aerodynamic structures in micro air vehicles or even wind energy extraction.

The domain of aeroelasticity has enjoyed a rich history in engineering where, traditionally, aerodynamic systems are designed to be just flexible enough to avoid instabilities that result from the complex reciprocal interactions between aerodynamic forces and elastic deformations (Bisplinghoff 1962). But recent research on wing flexibility highlights the possibility of tuning actuation parameters and flexibility for improved flight performance or control in both natural systems (Mountcastle and Daniel 2009, 2010, Young *et al* 2009, Zhao *et al* 2010, Lee *et al* 2011, Nakata and Liu 2012) and engineered systems (Heathcote and Gursul 2007, Alben 2008, Lua *et*

al 2010, Stanford *et al* 2011, Barannyk *et al* 2012, Leftwich *et al* 2012, Alben *et al* 2012). In addition, several studies indicate that structural and hydrodynamic resonances have a large impact on the propulsive efficiency of wings and fins (Kang *et al* 2011, Ramananarivo *et al* 2011, Moored *et al* 2012, Alben 2012, Dewey *et al* 2013). And, at least in the case of insect flight, inertial-elastic forces appear to dominate over fluid forces (Daniel and Combes 2002, Fry *et al* 2003, Yin and Luo 2010). As these results begin to reveal the principles that govern the performance of compliant wings and fins, researchers are also developing novel micro-air vehicles or Q2 underwater transport devices based on these results (Ellington 1999, Clark and Smits 2006, Bandyopadhyay *et al* 2008, Shyy *et al* 2010, Moored *et al* 2012, Nakata *et al* 2011, Ma *et al* 2013).

Unlike previous studies that have largely examined only one facet of wing movement, pitch or heave (Alben 2008, Michelin and Smith 2009, Kang *et al* 2011), or have been constrained to explore only phase, stiffness, or frequency alone (Daniel and Combes 2002, Zhu 2007, Mountcastle and Daniel 2010, Zhang *et al* 2010, Nakata and Liu 2012), this work uses an integrative approach to examine flight performance of a pitching and heaving wing over a broad range of frequencies, phases, and stiffnesses that are relevant to insect flight. Our approach models the fluid–structure interaction in an efficient manner so as to allow an exploration of the importance of fluid loading over a wide range of parameters. Many prior methods including experimental techniques (Dickinson and Gotz 1993, Clark and Smits 2006, Lauder and Madden 2007, Lentink *et al* 2008, Michelin and Smith 2009, Mountcastle and Daniel 2009, Dewey *et al* 2013) and full computational fluid dynamic solvers (Liu *et al* 1998, Sun and Tang 2002, Young *et al* 2009, Zhang *et al* 2010) are too time consuming to permit the exploration of such a vast parameter space. And, while some computationally efficient models do exist, they either do not couple the fluid to the solid (Mountcastle and Daniel 2010) or have a limited ability to capture wing bending (Toomey and Eldredge 2008, Vanella *et al* 2009, Eldredge *et al* 2010, Fitzgerald *et al* 2011). As a result, we developed a computationally efficient model that captures the fluid–structure interaction in a compliant insect wing using a finite element model coupled with a modified unsteady vortex particle model. Although the focus of this work is on insect wings, we could easily modify our model to explore wings of other shapes and sizes.

Here we seek to understand how the aeroelastic nature of insect flight depends on the wide range of parameters encountered in nature, particularly with regard to the actuation frequency of

the wing, the phase of actuation between pitch and heave, and the flexibility of the wing. Thus, for a range of actuation frequencies, phases of actuation, and flexural stiffnesses, we ask (1) how does flight performance—measured by coefficients of lift and thrust—vary and (2) how much does aerodynamic forcing cause the wing to bend and thereby affect flight forces? We identify parameter regions in which the coupling between fluid dynamic loading and inertial-elastic processes may not play a crucial role in developing flight forces and emergent wing bending. Ultimately, this approach will inform how the mechanical design of wings can be tuned for effective force generation (or wind energy extraction).

3.3 METHODOLOGY

To explore how flight performance varies over a range of actuation and material parameters relevant to insect flight, we developed a computationally efficient two-dimensional simulation of a wing by coupling a modified vortex particle model of the fluid with a nonlinear finite element model of the solid. We employed weak coupling to incorporate fluid–structure interaction by solving the fluid and solid models iteratively (see section S1 of the supplementary information for program diagram (available from stacks.iop.org/BB/9/000000/mmedia)). Although three-dimensional phenomena, including tip effects, span-wise momentum flux, and leading edge vortex generation have a substantial impact on the aerodynamics of flight (Ellington *et al* 1996, Dickinson *et al* 1999, Lentink and Dickinson 2009, Lentink *et al* 2009), we do not address those issues in this paper, largely because we focus on a two-dimensional model to explore a large parameter space associated with actuation dynamics and material properties.

In addition, while the fidelity of vortex methods in estimating flows and forces is limited relative to solvers of the Navier–Stokes equations, we chose this lower accuracy model as a more computationally efficient, but yet sufficiently accurate, approach to permit the exploration of a large range of wing motions and material properties.

3.3.1 *Finite element model and mechanical parameters*

We modeled the elastic deformation of an insect wing using finite element methods (Bathe and Wilson 1976). We simulated a single two-dimensional section of the wing as a constrained-free beam broken into several elements (figure 3.1a). We allowed both nodes of each wing element to

have one local degree of freedom: in-plane rotation. We also permitted the wing elements to rotate and translate in global coordinates.

We chose two-node Hermitian beam elements to describe the curvature of the wing section. This approach allowed each element of the wing to assume a shape described by third-order Hermite polynomials. To account for the large deformations of the wing during flight, we utilized an updated Lagrangian approach to revise the location of the wing elements in global coordinates and solved for their locations in the local coordinate system with small displacements. We assumed that the length of each element remained constant but allowed the nodes of the elements to rotate and translate in the x- and y-directions while undergoing local deformations. In order to ensure unconditional stability of the solution, we used the Newmark integration method with $\gamma = 0.5$ and $\beta = 0.25$ (*i.e.* average acceleration method) (Bathe and Wilson 1976). This approach allowed us to take larger time steps without impacting the stability of the numerical solution while allowing sufficient accuracy.

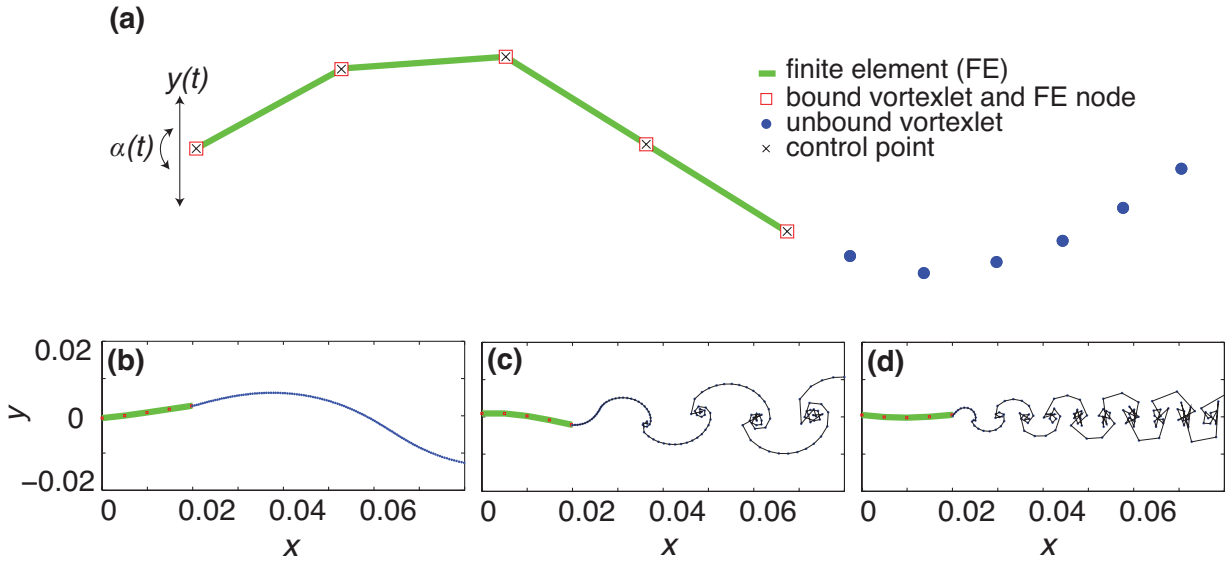

Figure 3.1. A diagram of the model setup (a) and the resulting wake structures for three actuation frequencies: (b) 10 Hz, (c) 25 Hz, and (d) 100 Hz.

We prescribed the vertical displacement (heave, $y(t)$) and in-plane rotation (pitch, $\alpha(t)$) at the leading edge of the wing as

$$y(t) = h_a \sin(2\pi f t) \quad (3.1)$$

$$\alpha(t) = \theta_a \sin(2\pi f t + \varphi) \quad (3.2)$$

where h_a is the amplitude of the vertical displacement, θ_a is the amplitude of the angular deflection, f is the frequency of actuation, φ is the phase of actuation, and t is time. We chose to fix $\theta_a = 0.001$ m and $h_a = 0.15$ rad so as to be consistent with prior values used for insect flight (Mountcastle and Daniel 2010). To perform a preliminary exploration of the importance of the phase of actuation between pitch and heave, we used a range of pitch-heave phases from $-\pi$ to π rad. We also explored actuation frequencies ranging from 10 to 100 Hz. Thus, we varied both phase and frequency of actuation to change the wing input dynamics.

We based the material and geometric properties of the wing model on experimentally measured values for wings of the hawkmoth, *Manduca sexta*. Flexural stiffness was the only material property that we varied and we used a range from 10^{-5} to 10^{-7} N m^2 according to values set forth in Combes and Daniel (2003c). We approximated wing shape as a rectangle with chord length, span and height of 0.02 m, 0.04 m, and 50 μm respectively, and density of 1200 kg m^{-3}.

Since wings are damped—both structurally and via the surrounding fluid—we also included damping in our solid model. The damping of insect wings is not well characterized so we performed an experiment with a laser vibrometer to measure the damping of an excised Manduca sexta wing in air (see section S2 of the supplementary information (available from stacks.iop.org/BB/9/000000/mmedia)). Our analysis revealed that the damping ratio is approximately 0.15 for the first mode of vibration so we implemented this damping ratio in the finite element model using Rayleigh damping. While we could have implemented damping using other approaches, the damping we measured should be proportional to the frequency of oscillation and correspond to changes in velocity. As a result, we implemented viscous damping proportional to the mass of the wing. In order to keep the simulations consistent as we varied stiffness, we implemented the damping such that the time of free decay was constant for all simulations.

3.3.2 *Ideal flow model of the fluid*

Wu (1971) and Lighthill (1975) were the first to demonstrate that fluid flow at the moderately high Reynolds numbers associated with the flight of large insects (103–104) is well described by inviscid flow theory. More recently, Ramamurti and Sandberg (2001) showed very good

agreement between an inviscid model and experimental data for the wing dynamics of the fruit fly Drosophila (Reynolds number around 102). Thus, we used a modified vortex particle method based on thin wing (infinitesimal thickness) inviscid flow theory following the method of Mountcastle and Daniel (2010).

According to this approach, we constructed a model of the fluid flow using vortexlets—point sources of vorticity represented as singularities but modified here according to Shukla and Eldredge (2007). The velocity of the flow $\{u_x(t),u_y(t)\}$ at every point $\{x, y\}$ in space was described by the strength, γ_i(t), and the position, $\{x_i, y_i\}$, of each vortexlet:

$$\left\{u_x(t),u_y(t)\right\}=\left\{-\sum_{i=1}^{N}\frac{\gamma_i(t)(y-y_i)}{2\pi(r^2+\delta^2)},\sum_{i=1}^{N}\frac{\gamma_i(t)(x-x_i)}{2\pi(r^2+\delta^2)}\right\} \tag{3.3}$$

$$r^2=\left(x-x_i\right)^2+\left(y-y_i\right)^2 \tag{3.4}$$

where N is the number of vortexlets, and δ^2 is a smoothing parameter that ensures a singularity does not occur in the computation of the velocity field. In order to allow the size of the wake structure to vary with actuation frequency, f, and wing flexural stiffness, EI, we set

$$\delta^2=0.1r_w^2 \tag{3.5}$$

$$r_w=c\ (5/N_e)\ U_{ref}/(f\,(EI\cdot 10^6)) \tag{3.6}$$

where c is the chord length of the wing section, N_e is the number of finite elements in the solid model, and U_{ref} is the free-stream velocity of the fluid. According to methods used in prior studies, we chose this value of δ^2 because it allowed for the formation of stable vortex patterns (Shukla and Eldredge 2007, Mountcastle and Daniel 2010). Even when we increased or decreased the smoothing parameter by a factor of five, our results remained within 5% of the values we report in section 3 (see section S3 of supplementary information for more details (available from stacks.iop.org/BB/9/000000/mmedia)).

At each time step, a vortex was shed into the wake and transported downstream according to the flow induced by the entire system of bound and shed vortexlets and the free-stream velocity. The entire velocity field was therefore the linear superposition of the free-stream velocity and the velocity induced by the system of bound and shed vortexlets (see figures 3.1b–d and the supplementary material (available from stacks.iop.org/BB/9/000000/mmedia)). To be consistent

with prior values used to model insect flight (Mountcastle and Daniel 2010), we prescribed the free-stream velocity to be 120 cm s^{-1}.

To solve for the unknown strengths of the vortexlets, we satisfied three conditions: the flow separated tangentially from the trailing edge (Kutta condition), no flow went through the wing (no-penetration condition), and the sum of all the vortexlet strengths at each time interval was zero (Kelvin's circulation theorem: conservation of total circulation). The non-penetration condition was achieved by setting the normal velocity of the solid model equal to the normal velocity of the fluid at control points co-located with every vortexlet on wing surface (see figure 3.1a). These conditions formed a system of linear equations that allowed us to determine the strengths of the bound vortexlets. We used these vortexlet strengths to solve for the steady pressure, P_s, and unsteady pressure, P_u, at every position, s_i, on the wing and at every time, t, using

$$P_s(s_i,t) = \rho U_{ref}\gamma(s_i,t) \tag{3.7}$$

$$P_u(s_i,t) = \rho\frac{d}{dt}\int_0^{s_i}\gamma(s,t)\,ds \approx \rho\Delta x\frac{d}{dt}\sum_{j=1}^{i}\gamma(s_j,t) \tag{3.8}$$

where ρ is the density of the fluid, U_{ref} is the free-stream velocity of the fluid, $\gamma(s_i,t)$ is the strength of the vortexlet at position s_i along the wing from leading to trailing edge at time t, and x is the length of each element of the wing (Bisplinghoff 1962, Katz and Plotkin 2001). We imposed these fluid pressures as the external forces acting on the solid model, thus coupling the fluid to the solid and allowing the relative displacement of the wing to be a combination of inertial-elastic forcing and fluid dynamic loading.

We also used the steady and unsteady pressures to compute values of lift and thrust per unit length according to

$$T = \Delta x\sum_{i=1}^{N_e}\left[P_s(s_i,t)+P_u(s_i,t)\right]\,n_{x_i} \tag{3.9}$$

$$L = \Delta x\sum_{i=1}^{N_e}\left[P_s(s_i,t)+P_u(s_i,t)\right]\,n_{y_i} \tag{3.10}$$

where N_e is the number of elements, and $n_{x,i}$ and $n_{y,i}$ are the components of the unit vector normal to the wing surface along the *x*- and *y*-directions. We used these values for lift and thrust forces to compute the coefficients of lift and thrust (table 3.1).

3.3.3 *Coupled fluid–solid model*

We executed the model in two modes (1) with the fluid and solid coupled (*i.e.* fluid–structure interaction permitted) and (2) with the fluid and solid uncoupled (*i.e.* solid deformation due to passive inertial-elastic forcing alone). In the coupled mode, we weakly coupled the fluid and solid models by imposing the computed fluid pressure onto the solid model at each time step (see section S1 of supplementary information (available from stacks.iop.org/BB/9/000000/mmedia)).

We integrated the solid and fluid models between time steps using a second order Runge–Kutta method. As above, integration within the solid model was performed via Newmark integration. Thus, Newmark integration was used to subsample between Runge–Kutta time steps. The coupling was weak because we solved the solid and fluid models separately and only allowed them to interact between time steps. Despite this limitation, the coupled model did solve for the complete aeroelastic dynamics of the actuated wing.

For the uncoupled model, we did not allow the fluid pressure to act as a load on the structural model. That is, we set the pressure induced on the wing by the fluid to zero and solved for the deformation of the solid independent of the fluid. By running the model with the coupling both enabled and disabled, we quantified the importance of fluid coupling to the development of flight forces.

3.3.4 *Non-dimensional parameters*

We used several non-dimensional variables in our analysis (table 3.1). The relevant physical quantities listed in table 3.1 include: the flexural stiffness, EI, of the wing, the density, ρ_f, and free-stream velocity, U_{ref}, of the fluid, the chord length, c, span, b, and thickness, h, of the wing, the frequency, f , and pitch, θ_a, and plunge, h_a, amplitudes of wing actuation, the lift, L, and thrust, T, forces produced by wing movement, the displacement of the wing tip for flexible, y_{tip_flex}, and rigid wings, y_{tip_rigid}, and the time, t.

Table 3.1. Non-dimensional parameters of interest.

Parameter Name	Symbol	Definition
Effective stiffness	R	$EI/\left(\rho_f U_{ref}^2 b^2 hc\right)$
Reduced frequency	k	$2\pi fc/U_{ref}$
Lift coefficient	C_l	$L/\left(0.5\rho_f cU_{ref}^2\right)$
Thrust coefficient	C_t	$T/\left(0.5\rho_f cU_{ref}^2\right)$
Relative tip displacement	ξ	$(y_{tip,flex}-y_{tip,rigid})/c$
Lift ratio	L^*	$L_{coupled}/L_{uncoupled}$
Thrust ratio	T^*	$T_{coupled}/T_{uncoupled}$
Displacement ratio	D	$\xi_{coupled}/\xi_{uncoupled}$
Convective time	τ	tU_{ref}/c

Since we fixed the amplitudes of pitching and plunging to be h_a/c = 0.05 and θ_a = 0.15 respectively, the Strouhal number was proportional to reduced frequency. As a result, we report our results using only reduced frequency, k. In addition, since this is an inviscid model, our results apply to Reynolds numbers in excess of 103.

Several of these variables are widely used or have been cited previously in the literature (Kang *et al* 2011). However, we chose to introduce three new parameters in order to capture the relative importance of fluid–solid coupling: (1) the lift ratio, (2) the thrust ratio, and (3) the displacement ratio. We computed the thrust ratio by measuring the average value of thrust with fluid–solid coupling and dividing it by the average value predicted without coupling model. Since the average value of lift and displacement is zero, we computed these ratios using the root-mean-square values with and without coupling.

In order to ensure that the results would be comparable over the entire range of frequency and stiffness values that we explored, we performed our analysis of all three ratios using only the last five cycles of each simulation after the solution reached steady state (figure 3.2). In order to

ensure all solutions reached steady state, we changed the number of cycles for each simulation according to the imposed stiffness, *EI*, and the forcing frequency, *f*.

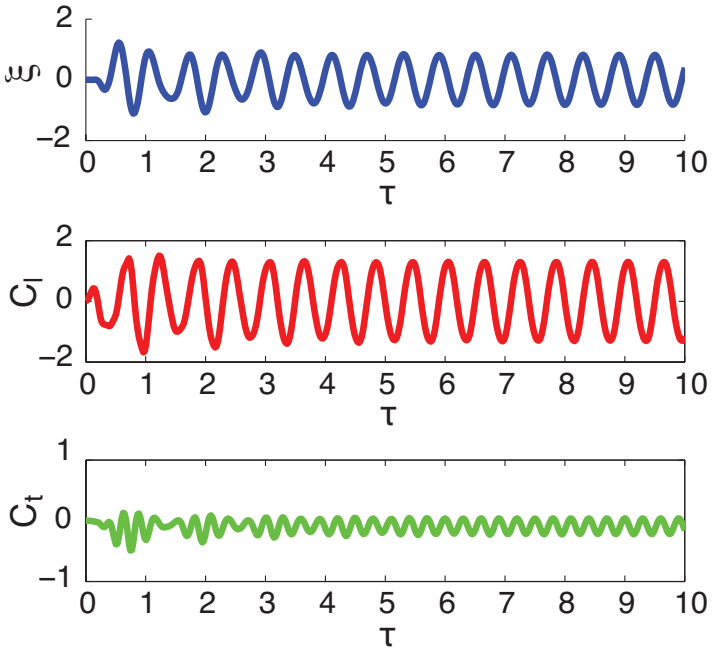

Figure 3.2. The relative tip displacement (ξ), coefficient of lift (C_l), and coefficient of thrust (C_t) plotted versus convective time, τ. The region that we use to report our results corresponds to the last five cycles after the solution reaches steady state (*i.e.* t = 7 – 10).

3.3.5 *Model validation, convergence testing, and simulations*

We validated the fluid model using two methods (see section S3 of the supplementary information (available from stacks.iop.org/BB/9/000000/mmedia)). In both cases we prescribed the solid model to be rigid. First, we compared the lift force of the rigid model with constant angle of attack in steady flow to the theoretical prediction of an inclined plate (Katz and Plotkin 2001). The results showed that the steady state solution of the model corresponded with the theoretical prediction for several different angles of attack. Second, we compared the lift force of the model undergoing small amplitude heave and pitch motions to Theodorsen's solution for unsteady motion of a thin plate (Katz and Plotkin 2001). These results demonstrated that the

model correctly reproduced Theodorsen's solution for small amplitude motions at several frequencies of actuation.

We validated the solid model by imposing a periodic input and comparing the displacement of the trailing edge to the analytical solution for ground motion of a fixed-free beam (Timoshenko *et al* 1974; see section S4 of the supplementary information for solid model validation (available from stacks.iop.org/BB/9/000000/mmedia)). Due to our desire to look only at the steady-state solution and since our forcing was not close to the higher modes of vibration, we found that the motion of the wing was well described using only the first five modes of vibration. In addition, since the first five modes were well captured by four cubic polynomials, we only needed four elements to capture the motion of the wing.

We also examined the convergence of both the solid and fluid solutions as we varied the timestep size and element size (see section S5 of the supplementary information for convergence testing (available from stacks.iop.org/BB/9/000000/mmedia)). In order for the solution to converge, our analysis indicated that for four elements we needed to use a time step of 2×10^{-4} s for the fluid and 4×10^{-6} s for the solid. Since the solid model dominated the time required to solve our systems, we implemented the 2×10^{-4} s time step for the fluid and then subsampled the solid 50 times during every time step.

To explore how frequency of actuation, phase of actuation, and flexural stiffness interact to impact flight performance in insect flight, we ran simulations over a range of parameters relevant to insect wings. We varied flexural stiffness at twenty intervals evenly spaced logarithmically in base 10 from 10^{-5} to 10^{-7} N m^2 (effective stiffness, R, of ~37 to 3700) and frequency at 20 intervals from 10 to 100 Hz (reduced frequency, k, of ~1 to 10) for three different phases of actuation (φ equal to 0, $\pi/2$, and π). We also varied frequency at twenty intervals from 10 to 100 Hz and phase at twenty intervals from $-\pi$ to π for three values of flexural stiffness (10^{-5} N m^2, 5×10^{-6} N m^2, and 10^{-6} N m^2). We ran all simulations with fluid–solid coupling enabled and disabled. Thus, we ran a total of more than 4000 simulations (see supplementary information (available from stacks.iop.org/BB/9/000000/mmedia)).

3.4 RESULTS AND DISCUSSION

3.4.1 *Coupled model results: frequency versus stiffness*

We found that the relative displacement, ξ, coefficient of lift, C_l, and coefficient of thrust, C_t, vary considerably with effective stiffness, R, and reduced frequency, k, for three different phases of actuation (figure 3.3). All three parameters—relative displacement, lift and thrust—exhibit similar contours with one to two continuous regions of peak values. As the phase advance of the pitch relative heave increases (*i.e.* value of phase increases), the magnitudes of the contours also increase. In addition, for all three phases of pitch-heave actuation, the regions of peak lift and thrust values correspond to resonances of the solid and therefore align with the peak tip displacement of the structure (see section 3.4 for the computation of resonant frequencies). Although thrust does not exhibit as much variation near the second resonance as lift, the values of maximum thrust and lift both occur in the region of the first structural resonance.

This finding is consistent with previous results that show that optimal performance (not efficiency) is found near the structural resonant frequency of the wing (Zhang *et al* 2010, Kang *et al* 2011, Ramananarivo *et al* 2011). In contrast, other work on the fluid forces of swimming animals in water demonstrated that peak forces coincided with the fluid resonance of the wake structure rather than the resonance of the elastic structure (Moored *et al* 2012). Our results confirm that in the case of wings in air, it is the structural, not fluid dynamic, resonance that dominates the response.

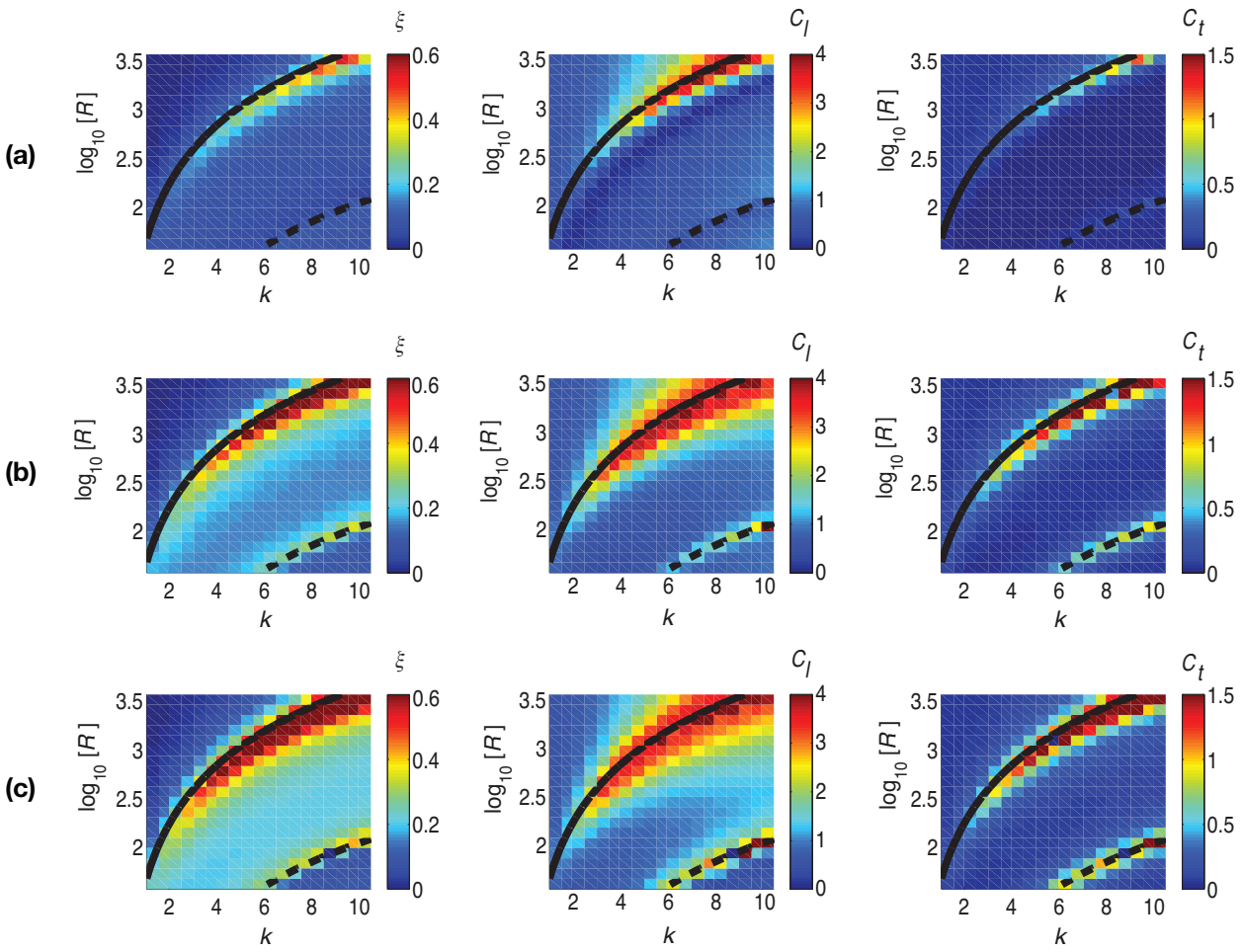

Figure 3.3. The log10 of the effective stiffness (R) plotted against the reduced frequency (k) for the relative tip displacement (ξ), coefficient of lift (C_l), and coefficient of thrust (C_t) as phase of actuation varies from (a) 0 rad to (b) π/2 rad to (c) π rad. For each subplot the value of the parameter of interest is plotted using the coloring indicated on the color bar to its right. The solid line represents the first damped resonant frequency of the structure and the dashed line is the second damped resonant frequency of the structure.

3.4.2 *Coupled model results: frequency versus phase*

We also found that the relative displacement, ξ, coefficient of lift, C_l, and coefficient of thrust, C_t, vary with phase of actuation, φ (figure 3.4). As above, all three parameters—tip displacement, lift and thrust—exhibit similar contours with fairly continuous regions of peak values. However, instead of increasing in magnitude as they did with phase in figure 3.3, the peak regions in these contours shift to the right as stiffness increases. The shift of these contours is a result of the shift in the resonant frequency of the structure, which increases with the

effective stiffness. Therefore, these results with varying phase reinforce the importance of structural resonance as a key determinant of fluid force generation.

In addition, the sharp peaks in forces suggest that very subtle shifts in the phase of actuation near these peaks, could lead to significant changes in force. These results show that the heave-pitch actuation phase has considerable control authority, allowing the force generated by the wing to be tuned using the phase of actuation. Indeed, Mountcastle and Daniel (2010) raised this issue earlier by taking the derivative of the flight forces with respect to phase to illustrate the potential for phase to modulate these forces.

3.4.3 *Relative importance of fluid loading*

With regard to the importance of fluid–structure interaction, we found that for the wide range of parameters used in this study, fluid loading rarely contributes to the emergent forces and bending dynamics of the wing (figures 3.5 and 3.6). Even though the values of tip displacement, coefficient of lift, and coefficient of thrust vary by over two orders of magnitude for this range of parameters (figures 3.3 and 3.4), the relative importance of fluid loading (*i.e.* the displacement, lift, and thrust ratios) appears to be surprisingly small (figures 3.5 and 3.6). While the resonant frequencies of the structure still correspond with the extrema in figures 3.5 and 3.6, the coupled lift at these resonant frequencies is only about 20% larger than the lift generated in the uncoupled case. Thus, even though resonance plays a key role in determining maximum flight forces, it appears to play less of a role in the relative importance of fluid loading.

In addition, in the regions outside of the structural resonance, the values of lift and thrust change by less than 2% when fluid loading is removed. As a result, while there are a few frequency and stiffness values where fluid loading changes the lift and thrust generated by the wing, particularly near the structural resonance, the fluid loading proves not to be important over the majority of this parameter space.

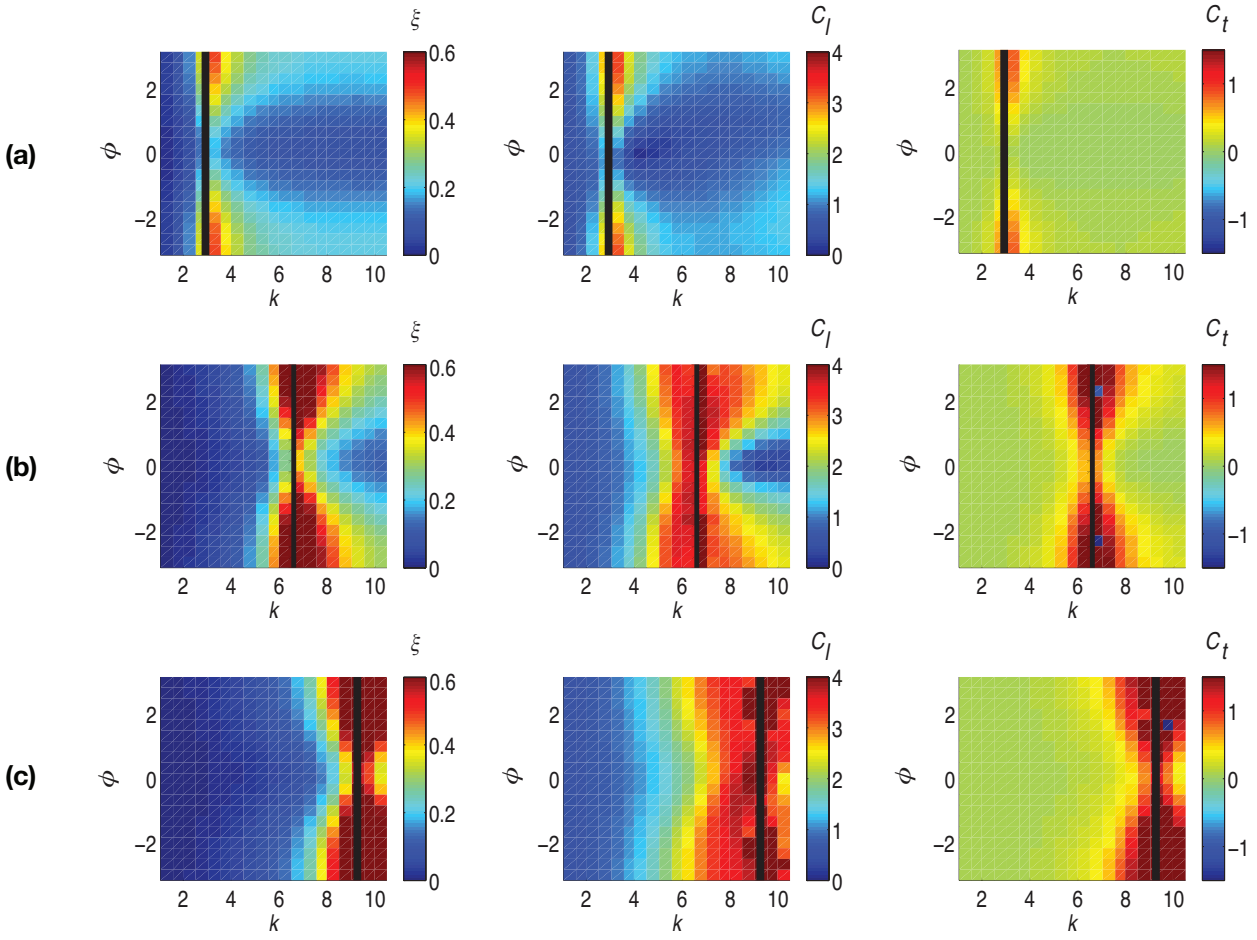

Figure 3.4. The heave-pitch actuation phase (φ) plotted against the reduced frequency (k) for the relative tip displacement (ξ), coefficient of lift (C_l), and coefficient of thrust (C_t) as effective stiffness varies from (a) 378 to (b) 1840 to (c) 3780. For each subplot the value of the parameter of interest is plotted using the coloring indicated on the color bar to its right. The solid line represents the first damped resonant frequency of the structure.

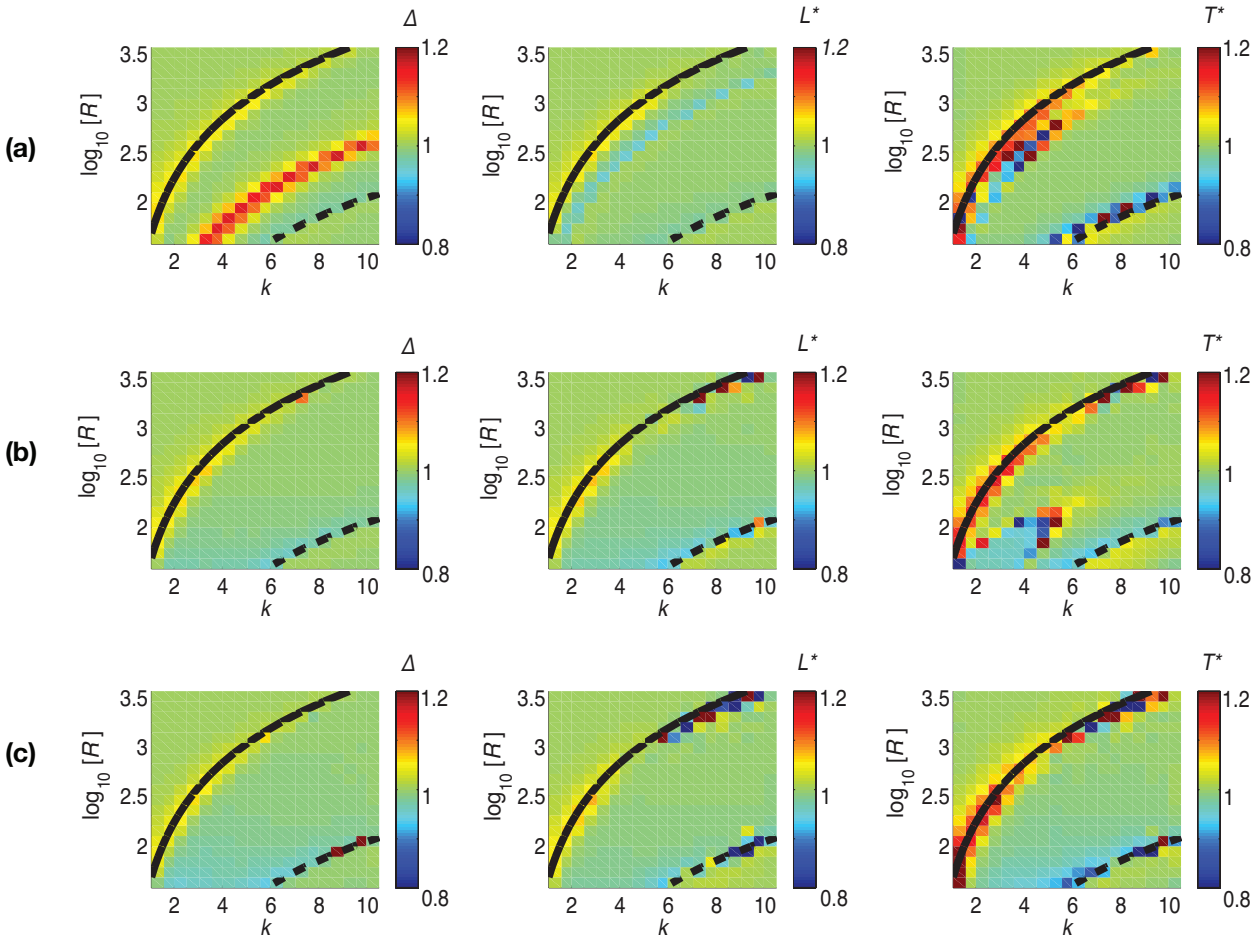

Figure 3.5. The $\log_{10}$ of the effective stiffness (R) plotted against the reduced frequency (k) for the displacement ratio (Δ), lift ratio (L^*), and thrust ratio (T^*) as phase of actuation varies from (a) 0 rad to (b) π/2 rad to (c) π rad. For each subplot the value of the parameter of interest is plotted using the coloring indicated on the color bar to its right. As defined in table 3.1, if the value of the ratio equals 1, then there is no difference between the coupled and uncoupled values. The solid line represents the first damped resonant frequency of the structure and the dashed line is the second damped resonant frequency of the structure. It is important to note that the displacement ratio takes on high values when the absolute value of the tip displacement is quite low, hence the third line in the upper left plot.

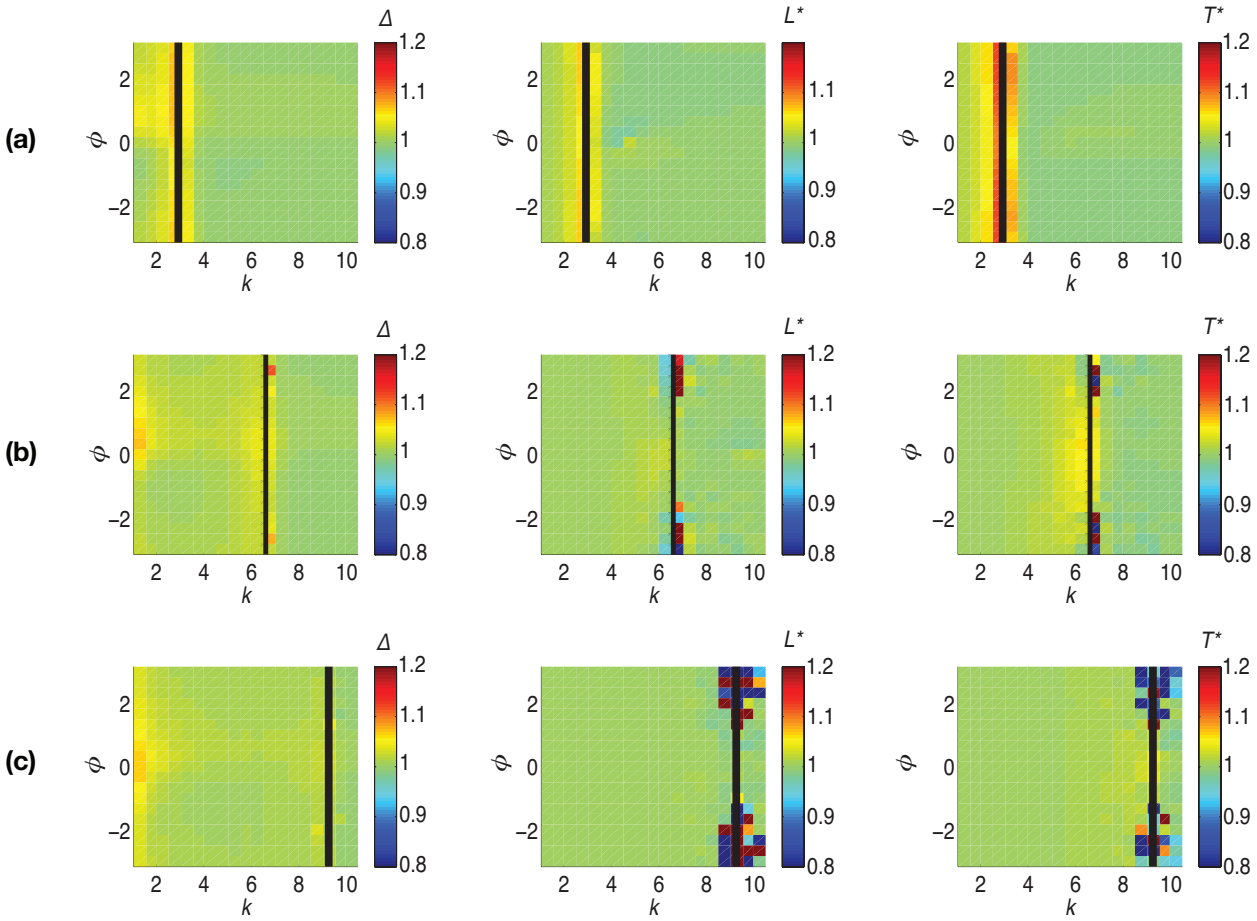

Figure 3.6. The heave-pitch actuation phase (φ) plotted against the reduced frequency (k) for the displacement ratio (Δ), lift ratio (L^*), and thrust ratio (T^*), as effective stiffness varies from (a) 378 to (b) 1840 to (c) 3780. For each subplot the value of the parameter of interest is plotted using the coloring indicated on the color bar to its right. As defined in table 3.1, if the value of the ratio equals 1, then there is no difference between the coupled and uncoupled values. The solid line represents the first damped resonant frequency of the structure and the dashed line is the second damped resonant frequency of the structure.

3.4.4 *Importance of structural resonance*

The peak regions in figures 3.3–3.6 correspond to the first and second damped resonance frequencies of a constrained-free (cantilever) beam that has the structural and material properties of our model. As determined analytically, these damped resonance frequencies, ω_i, vary with flexural stiffness, EI, according to

$$\omega_i = \lambda_i^2 \omega_n \sqrt{1-2\xi^2} = \lambda_i^2 \sqrt{\frac{EI(1-2\xi^2)}{m_{eq}c^3}} \tag{3.11}$$

where ζ is the damping ratio, m_{eq} is the equivalent mass of the wing (equal to 0.048 g), c is the chord length, and λ_i are the roots of the frequency equation that governs the motion of the beam (Volterra and Zachmanoglou 1965). The first and second roots are $\lambda_1 = 1.875$ and $\lambda_2 = 4.694$. To illustrate the importance of structural resonance, we overlaid our results with the first two damped resonance frequencies obtained from (11) (solid lines correspond to the non-dimensional representation of ω_1 and dashed lines correspond to the non-dimensional representation of ω_2).

3.5 CONCLUSIONS

In this work, we explore how the fluid loading on an insect wing influences the shape of the wing and thereby modifies the flight forces it develops. We examine how the magnitudes of tip displacement, coefficient of lift, and coefficient of thrust change as actuation frequency, phase of pitch-heave actuation, and wing stiffness vary. We also look at how much the aeroelastic nature of the wing (*i.e.* the coupling of the fluid loading to the elastic structure) impacts the total deformation of the wing and the overall flight forces that the wing develops.

While the fidelity of vortex methods can be limited as compared to Navier–Stokes solvers, our goal is not to replicate the exact flow field around an insect wing but instead to develop a preliminary understanding of the impact of actuation frequency and flexibility on the development of flight forces, separate from other factors like leading-edge and wing-tip vortices. One of the advantages of our model is that it allows us to achieve a computationally efficient approach while achieving sufficient accuracy so as to explore a vast parameter space. Despite its limitations, our approach does not preclude us from discussing the general trends that result from running the model with and without fluid loading.

Our analysis shows that when the excitation frequency of an insect wing aligns with the resonant frequency of the elastic structure, then flight forces increase dramatically. Despite the fact that the magnitudes of the aerodynamic forces increase in the regions of structural resonance, fluid loading is still relatively unimportant in these regions. Furthermore, in regions that do not coincide with the resonant frequency of the structure, the difference between the forces and displacements of the coupled and uncoupled simulations is very small. These results

indicate that fluid loading plays little role in determining flight forces over the entire parameter space.

These results differ from those that have been reported previously for fins in water. While the alignment of hydrodynamic resonance and structural resonance maximizes the propulsive efficiency of flexible plates in water (Dewey *et al* 2013), the hydrodynamic resonance alone plays the dominant role in maximizing the forces developed by a fin in water (Moored *et al* 2012). In contrast, here we show that structural resonance plays the dominant role in maximizing the forces developed by an insect wing in air. However, the ratio of the fluid density to the solid density is about three orders of magnitude greater in the hydrodynamic cases than for insect wings in air. As a result, it is not surprising that these results might differ such that the inertial-elastic forces dominate when the density of the solid is larger whereas the fluid forces dominate when the opposite holds true. Future work will modify our model to perform a similar analysis over a range of frequencies and stiffnesses that are relevant for swimming animals. We expect that these results will show similar trends compared to those reported previously for swimming animals and also that the relative importance of fluid loading is much greater for fins in water.

Our exploration of this parameter space also reveals regions of high sensitivity that allow for optimization of lift and thrust using frequency and phase of wing activation. Since insects can easily control the frequency and phase of their wings, these results suggest that insects are capable of tuning their flight forces by modifying these parameters during flight. However, control authority residing in wing actuation and bending would logically require sensory feedback for responses to gusts and planned course changes. Such sensory feedback might come from visual systems. But in insects like the hawkmoth, visual responses may be too slow for effective control. However, wings themselves, which are richly imbued with strain sensing structures (campaniform sensilla), provide exceedingly rapid responses to the bending dynamics of the wing. Thus, information about bending dynamics and its potential for control is available all along the wing surface (Daniel *et al* 2012). Future work will examine how insects could use sensory feedback systems to detect rapid changes in wing shape and then modify wing actuation frequency and phase to alter flight forces in response to disturbances during flight.

There are several time-varying phenomena that play a role in insect wing aeroelasticity, including, but not limited to, the elastic vibrations of the wing, the oscillatory boundary conditions, and the vortex shedding in surrounding fluid. While previous research showed that

the resonance of the fluid structure plays a key role in determining hydrodynamic forces for swimming animals, it appears that for an insect wing in air, in contrast to a fin in water, the resonance of the solid structure plays the dominant role. In addition, although structural resonance coincides with maximum flight forces, the relative importance of fluid loading remains relatively unimportant over a broad range of insect wing stiffnesses, frequencies and phases of actuation. These results suggest that the design process for wings in flapping micro air vehicles can benefit from uncoupled models and that the structural design and actuation dynamics of the wings can be tuned to optimize aerodynamic performance.

3.6 ACKNOWLEDGMENTS

The authors thank Brad Dickerson (University of Washington) for his assistance performing the damping experiments, Steve Brunton (University of Washington) for his discussions and consultations on model validation, Andrew Mountcastle (Harvard University) for his discussions about vortexlet methods, and Tim Dardis (University of Washington) for his assistance with the laser vibrometer. This work was supported by NSF grant EEC-1028725 to TLD and AFOSR grant FA9550-11-1-0155 to TLD as well as the Komen Endowed Chair and ONR MURI grant N000141010952 to TLD. ALE also received funding from an NSF Graduate
Research Fellowship (DGE-0718124).

Chapter 4. INSECT WINGS AS GYROSCOPIC SENSORS

Although insect wings are primarily used as actuators for propulsion, they are also covered in hundreds of strain sensors called campanifom sensilla. The hind wings of some insects, specifically flies, have evolved into dumbbell-shaped sensory structures called halteres. Insects that possess halteres use the campaniform sensilla at the base of their halteres to detect rotational perturbations of their bodies. Since halteres are derived from wings, evolution suggests that rudimentary versions of the halteres' sensory mechanisms might reside in wings themselves. Thus, my collaborators and I were interested in exploring how changes in the structural dynamics of an insect wing might be used to detect rotational perturbations of the body.

To explore this question, we developed a low-order model of the structural dynamics of a compliant, flapping wing with body rotations orthogonal to the axis of wing flapping. The model showed us how wing dynamics differ when a wing flaps with and without body rotations. Since results from my prior work (see Chapter 3) indicated that the influence of the fluid loading should have a limited impact on the structural dynamics of the wing, for efficiency and simplicity, we only modeled the structural dynamics in our computational model. However, we wanted to confirm that fluid-structure interaction did not substantially impact our results so we constructed a robotic wing model and actuated in air. We found that in both our computational and robotic bio-inspired wing models, a new dynamic mode emerges when the wings undergo rotation while flapping. This mode manifests as torsion orthogonal to the rotation axis and can be detected using shear strain, normal strain, and vertical displacement. This work was published in the *Journal of the Royal Society, Interface* in January of 2015 (Eberle *et al* 2015).

This is an author-created, un-copyedited version of an article accepted for publication in the Journal of the Royal Society, Interface. The Version of Record is available online at http://rsif.royalsocietypublishing.org/content/12/104/20141088.

4.1 ABSTRACT

Insects perform fast rotational maneuvers during flight. While two insect orders use flapping halteres (specialized organs evolved from wings) to detect body dynamics, it is unknown how

other insects detect rotational motions. Like halteres, insect wings experience gyroscopic forces when they are flapped and rotated and recent evidence suggests that wings might indeed mediate reflexes to body rotations. But, can gyroscopic forces be detected using only changes in the structural dynamics of a flapping, flexing insect wing? We built computational and robotic models to rotate a flapping wing about an axis orthogonal to flapping. We recorded high-speed video of the model wing, which had a flexural stiffness similar to the wing of the *Manduca sexta* hawkmoth, while flapping it at the wingbeat frequency of *Manduca* (25 Hz). We compared the 3D structural dynamics of the wing with and without a 3 Hz, 10 degree, rotation about the yaw axis. Our computational model revealed that body rotation induces a new dynamic mode: torsion. We verified our result by measuring wing tip displacement, shear strain, and normal strain of the robotic wing. The strains we observed could stimulate an insect's mechanoreceptors and trigger reflexive responses to body rotations.

4.2 INTRODUCTION

Insects acquire multimodal sensory information to control rapid flight maneuvers as they navigate through spatially and temporally complex natural environments. While both vision and mechanoreception play important roles, these sensory modalities operate over very different time scales. Indeed, signal transduction mechanisms used by the visual system result in information processing speeds that are too slow to account for the rapid maneuvers these animals display in free flight (Land and Collett 1974, Theobald *et al* 2010, Fuller *et al* 2014b). Thus, the timing precision, sensitivity and low latencies associated with mechanoreceptors make them critical features of insects' flight control circuitry.

Flies, for example, possess mechanosensory organs known as halteres that allow these animals to detect and correct for any perturbations to their flight path (figure 4.1a–c). These small club-shaped structures sit behind the forewings and oscillate at wingbeat frequency (figure 4.1b). During rotational maneuvers, halteres experience a Coriolis force, which is proportional to the angular velocity of the body and is orthogonal to the velocity of the haltere (Pringle 1948, Nalbach 1993). This force is thought to drive small, out-of-plane movements of the haltere (Thompson *et al* 2008), which would result in a normal strain at the haltere's base. While these movements have been demonstrated theoretically (Thompson *et al* 2008), they have not been confirmed experimentally. However, Coriolis-induced haltere bending has been shown to excite

embedded mechanoreceptors known as campaniform sensilla (figure 4.1c) (Fraenkel and Pringle 1938, Pringle 1948, Hengstenberg 1988), triggering a host of compensatory reflexes (Hengstenberg 1988, Nalbach and Hengstenberg 1994, Dickinson 1999). Interestingly, in engineering, an analogous method of strain sensing is commonly used in vibrating structural gyroscopes (Voss *et al* 1997, Funk *et al* 1999, Wu *et al* 2002, Bhadbhade *et al* 2008) where a mass attached to a beam is actuated via in-plane bending.

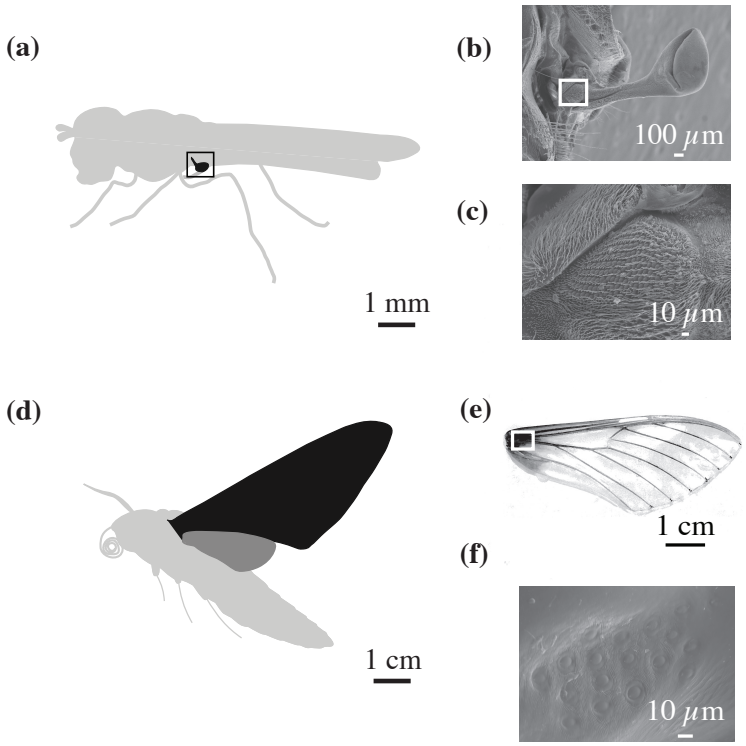

Figure 4.1. Insect halteres (a-c) and wings (d-f) possess campaniform sensilla. A single haltere on a robber fly is highlighted via the black box in (a) and magnified by SEM images in (b,c), where the white box in (b) indicates the location magnified in (c). The wing of a hawkmoth is highlighted in black in (d). A photograph of a cleared wing is shown in (e), where the white box in (e) shows the location the SEM image of campaniform sensilla in (f).

The evolution of the haltere has provided flies with the capacity to monitor inertial forces separate from the aerodynamic forces produced by the wings. However, only two insect orders, Diptera and Strepsiptera, possess such structures (Pix *et al* 1993). The vast majority of insects instead possess the antecedent structures of halteres: an additional pair of wings. Thus, how most

flying insects collect information about their body dynamics through mechanosensory structures is a long-standing problem in insect flight control. Although recent evidence suggests that the antennae of the hawkmoth *Manduca sexta* detect Coriolis forces and aid the animal in maintaining flight stability (Sane *et al* 2007, Hinterwirth and Daniel 2010, Hinterwirth *et al* 2012, Dickerson *et al* 2014), the use of antennae as putative inertial sensors does not preclude other structures from serving a similar role.

Since halteres are evolutionarily derived from wings, the wings of all insects might be capable of providing information about body rotations. Indeed, recent electrophysiological and behavioral evidence suggests that the campaniform sensilla embedded in the forewings of *Manduca* (figure 4.1d–f) provide the animal with input that mediates reflexes to virtual body rotations via wing bending (Dickerson *et al* 2014). However, the structural dynamics of flapping wings during whole-body rotations, and how these dynamics affect campaniform sensilla to trigger these reflexes, are unknown at this time.

Furthermore, the dynamics of wing deformations during body rotations are likely substantially different from those of halteres under similar conditions: the mass distribution, flexural stiffness, and aerodynamic loading of wings are very different than halteres. The flexibility of insect wings, for example, depends strongly on their morphology (Chen *et al* 2008, Combes and Daniel 2002, Combes and Daniel 2003a, Ennos 1988, Walker *et al* 2009, Wooton 1992, Wooton 1993, Norris *et al* 2010). There is also growing evidence that this flexibility enhances aerodynamic performance (Young *et al* 2009, Vanella *et al* 2009, Mountcastle and Daniel 2010, Nakata and Liu 2012, Eberle *et al* 2014). However, flapping wings experience more than just the large aerodynamic and inertial forces associated with their flapping. Just as with halteres, they also experience additional inertial forces, specifically gyroscopic forces, as they undergo rapid rotational accelerations of their bodies. Thus, wing compliance may serve to improve more than just aerodynamic performance; wing compliance may also amplify the wings' ability to serve as a sensor of the body's angular velocity.

While the dynamics of structures undergoing concurrent actuation and rotation are well studied in engineered systems, particularly with regard to the blades of helicopters and wind turbines (Veers et al 1998, Friedmann 2004, Sreenivasamurthy and Ramamurti 1981), these analyses often focus only on two bending axes and provide limited insight into the relationship between Coriolis forces and torsion. In addition, little work has been done to explore the

dynamics that emerge in a highly flexible cantilever plate that is subject to concurrent rotation and orthogonal actuation, as in the case of an insect wing (Jankauski and Shen 2014).

Here we explore how gyroscopic forces change the dynamics of a flapping, flexing wing. We sought to answer two questions. First, instead of undergoing small, out-of-plane deformations during rotations as are suggested for halteres, might flexible wings respond with a different dynamic mode? If so, is it then possible, using only the structural dynamics of a flapping, flexing wing, to determine the angular velocity of a whole-body rotation? To address these questions, we developed a computational model of a flapping, flexing plate subject to whole-body rotations. We then experimentally validated these results with two different robotic flapping actuators subject to rotations about an orthogonal axis. We found that a flapping, flexing plate subject to rotation in an orthogonal axis exhibits significant torsion, a deformation mode not previously suggested for gyroscopic sensing in animals. Thus, we propose that existing strain sensory systems in the wings of flying insects could be used to provide gyroscopic information. In this way, the wings would serve a function similar to the halteres, long heralded as an exemplar of gyroscopic sensing in nature.

4.3 MATERIALS AND METHODS

We used Lagrange's equations in combination with a simple model of a deformable plate to derive the equations of motion for a flexible insect wing undergoing flapping motions in a rotating reference frame. This approach draws from the Rayleigh method (Rayleigh 1877) and uses energy techniques rather than the force balance procedures that have been used previously (Pringle 1948, Nalbach 1993, Thompson *et al* 2008).

4.3.1 *Computational model of insect wing structural dynamics*

We modeled the wing as a thin plate of uniform thickness, stiffness, and density (figure 4.2; table 4.1). Using *Manduca* wings as a guide for dimensions, the chord and span were set to 25 mm and 50 mm, respectively. The plate consisted of four nodes, each having three local degrees of freedom: two angular degrees of freedom about the local x- and y-axes, $\phi_i(t)$ and $\theta_i(t)$ respectively, and one displacement degree of freedom along the local z-axis, $\delta_i(t)$.

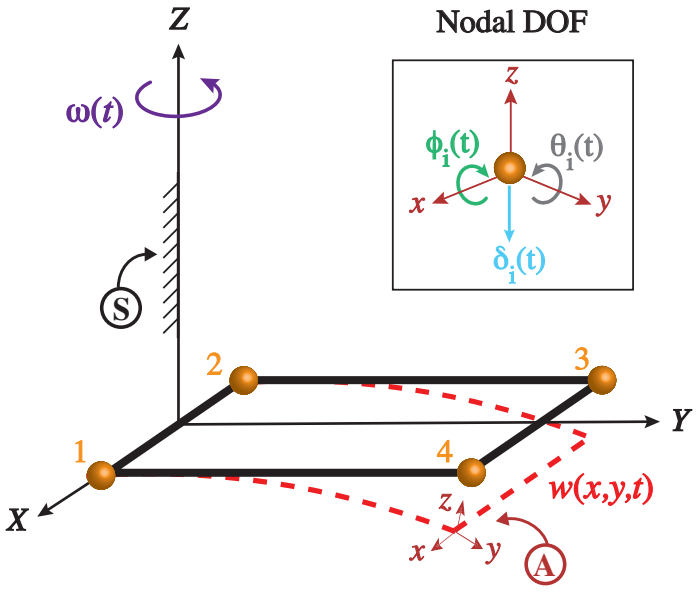

Figure 4.2. Diagram of the computational wing model, where symbols indicate the following: $w(x,y,t)$ is the z-displacement of the surface, which varies in space (x,y) over the surface of the wing and also in time, t; and $\omega(t)$ is the angular velocity of the body frame about the inertial Z-axis. The inertial frame, denoted by S, corresponds to the X, Y, and Z axes, and the local frame of the wing, denoted by A, is defined by the x, y, and z, axes. Orange spheres illustrate the nodes of the computational model. Nodes 1 and 2 are prescribed to move according to a single degree-of-freedom, which is a flapping input about the local x-axis. Nodes 3 and 4 are allowed three local degrees of freedom shown in inset: rotation about the local x-axis, $\phi_i(t)$, twist about the local y-axis, $\theta_i(t)$, and vertical displacement along the local z-axis, $\delta_i(t)$.

Table 4.1. List of symbols.

Symbol	Description
ϕ_i	angular displacement of the i^{th} node about the *x*-axis
θ_i	angular displacement of the i^{th} node about the *y*-axis
δ_i	angular displacement of the i^{th} node about the *z*-axis
Φ	input flapping angle
A_{flap}	amplitude of flapping
f_{flap}	frequency of flapping
w(x,y,t)	displacement of the wing's surface along the *z*-axis
a	half of chord length
b	half of span length
h	thickness
$\omega(t)$	time varying angular velocity of the body about *z*-axis
A_{rot}	amplitude of angular velocity
f_{rot}	frequency of angular velocity
ω_c	constant angular velocity of the body about *z*-axis
${}^{S}\boldsymbol{\Omega}^{A}$	vector of angular velocity of the body
$\varepsilon_{yy,F}$	normal strain along the *y*-axis while flapping
$\varepsilon_{xx,F}$	normal strain along *x*-axis while flapping
$\varepsilon_{xy,F}$	shear strain in *x*-*y* plane while flapping
$\varepsilon_{yy,F\&R}$	normal strain along *y*-axis while flapping and rotating
$\varepsilon_{xx,F\&R}$	normal strain along *x*-axis while flapping and rotating
$\varepsilon_{xy,F\&R}$	shear strain in *x*-*y* plane while flapping and rotating
$\Delta\varepsilon_{yy}$	difference in normal strain along *y*-axis between flapping versus flapping and rotating
$\Delta\varepsilon_{xx}$	difference in normal strain along *x*-axis between flapping versus flapping and rotating
$\Delta\varepsilon_{xy}$	difference in shear strain in *x*-*y* plane between flapping versus flapping and rotating
D_L	displacement of the left wing tip in *z*-direction
D_R	displacement of the right wing tip in *z*-direction
ΔD_F	Difference in *z*-displacement of left and right wing tips while flapping
$\Delta D_{F\&R}$	Difference in *z*-displacement of left and right wing tips while flapping and rotating
Δz	Difference in *z*-displacement of wing surface for flapping versus flapping and rotating
$\mathcal{F}\{\ \}$	Fourier transform operator

To be consistent with our experimental setup, the positions and angles of the two nodes at the base of the wing (nodes 1 and 2 in figure 4.2) were prescribed as follows

$$\phi_1(t) = \phi_2(t) = \Phi(t) = A_{flap}\left[\sin(2\pi f_{flap}t) + 0.2\sin(4\pi f_{flap}t)\right] \tag{4.1a}$$

$$\theta_1(t) = \theta_2(t) = 0 \tag{4.1b}$$

$$\delta_1(t) = \delta_2(t) = 0 \tag{4.1c}$$

where A_{flap} is the amplitude of flapping, f_{flap} is the wingbeat frequency and t is time. We did not allow any of the nodes to move in the local x- and y-directions (*i.e.* no stretching of the wing), but we did allow for displacement in the global X-, Y-, and Z-directions.

With the two nodes at base of the wing constrained, our wing model had six degrees of freedom remaining at nodes 3 and 4 (see figure 4.2). Thus, a vector, $\vec{q}(t)$, of the generalized coordinates is given by

$$\vec{q}(t) = \begin{bmatrix} \delta_3 & \phi_3 & \theta_3 & \delta_4 & \phi_4 & \theta_4 \end{bmatrix} \tag{4.2}$$

where δ_i is the linear displacement of the i^{th} node along the z-axis, ϕ_i is the angular displacement of the i^{th} node about the x-axis, and θ_i is the angular displacements of the i^{th} node about the y-axis.

We assumed that the displacement of the plate could be described by

$$w(x,y,t) = \left[\bar{N}(x,y)\right]^T \vec{q}(t) \tag{4.3}$$

where $\vec{q}(t)$ is the vector of generalized displacements given by equation 4.2 and $\bar{N}(x,y)$ is a vector of shape functions that satisfy the boundary conditions (Reddy 2004). For our model, we chose shape functions derived from fourth-order polynomials (Melosh 1963; see supplementary material for details). Although this model has a limited ability to capture the higher modes of vibration, our goal was not to explore all that is physically possible. We chose this reduced order model as a more computationally efficient, but yet sufficiently accurate, approach to explore the underlying dynamics that develop when a wing is flapped and also rotated. Moreover, the results generated by this computational model agree quite well with those measured experimentally (see Results).

The position of all points, m, on the plate's surface in the plate's reference frame, A, is therefore given by

$$ {}^{A}\vec{r}^{\,m}(x,y,t) = \begin{bmatrix} x & y & w(x,y,t) \end{bmatrix}^{T} \tag{4.4} $$

where x and y describe the position of each point in space, t is time, and $w(x,y,t)$ is given by equation 4.3. For simplicity, we only allowed the flapping wing to rotate globally about the root of the support edge (*i.e.* body rotation with zero translation). Due to our simplified dynamics, the angular velocity, ${}^{S}\vec{\Omega}^{A}$, of the wing's reference frame, A, in the inertial frame, S, was therefore

$$ {}^{S}\vec{\Omega}^{A} = \begin{bmatrix} \dfrac{d\Phi}{dt} & 0 & \omega(t) \end{bmatrix}^{T} \tag{4.5} $$

where Φ is the flapping rotation about the X-axis, which is prescribed at nodes 1 and 2 by equation 4.1a, and $\omega(t)$ is the rotation of the body about the Z-axis.

In one set of simulations, we set the angular velocity of the body to be a constant value equal to the maximum angular yaw velocity of 800°/s encountered by *Manduca* during flight (Hedrick *et al* 2009). However, since insects rarely perform maneuvers at constant angular velocities in their natural environment, we also simulated a periodic angular velocity of the body. Thus, in the computational model, the angular velocity of the body was either described by

$$ \omega(t) = \omega_c = 800^{\circ}/s \tag{4.6a} $$

or

$$ \omega(t) = A_{rot}\sin(2\pi f_{rot} t) \tag{4.6b} $$

where f_{rot} is the frequency of the rotation and A_{rot} is the amplitude of the rotation. In the case of periodic rotation (equation 4.6b), the frequency and amplitude of the rotation were set to 3 Hz and 10°, respectively. We based the frequency of body rotation on previous experiments of *Manduca* subject to actual and simulated whole-body rotations (Hinterwirth and Daniel 2010, Dickerson *et al* 2014). The amplitude of the rotation was set by the amount of maximum rotation that we could achieve in our experimental setup (see next section).

With the position of all points on the plate surface given by equation 4.4 and the angular velocity of the wing in the inertial frame given by equation 4.5, we derived the equations of

motion for a wing subjected to rotation using Lagrange's equations (see supplementary material). The general form of this system of equations is given by

$$\frac{d^2\bar{q}(t)}{dt^2} = M^{-1}M_a\frac{d\vec{v}_o}{dt} + \left(\frac{d\Phi}{dt}\right)^2\bar{q}(t) - M^{-1}K\bar{q}(t) + M^{-1}I_C R^S\vec{\Omega}^A + M^{-1}\eta\frac{d\bar{q}(t)}{dt} \tag{4.7}$$

where $\bar{q}(t)$ is the vector of generalized coordinates (equation 4.2) for which we solved, M^{-1} is the inverse of the mass matrix, M_a is the applied acceleration mass matrix, $\vec{v}_o$ is a vector that describes the linear velocities of and angular velocities about basal nodes of the wing, Φ is the prescribed input flapping (equation 4.1a), K is the stiffness matrix due to strain energy of the plate, I_c is an inertia-like matrix that describes the contribution of the Coriolis, R is the rotation matrix between the body and the wing, ${}^S\vec{\Omega}^A$ is the angular velocity of the wing in the inertial frame, and η is the damping factor. The terms on the right hand side correspond to the angular acceleration of the plate due to the initial conditions, the centrifugal force, the stiffness of the plate, the Coriolis force, and the wing damping, respectively.

We solved this system of second-order ordinary differential equations for the generalized coordinate vector $\bar{q}(t)$ over ten rotation cycles, starting from rest, using a fourth-order Runge Kutta method in MATLAB (The MathWorks, Natick, MA, USA). Simulations were run under five different conditions: flapping alone, constant rotation alone, periodic rotation alone, a combination of both flapping and constant rotation, and a combination of both flapping an periodic rotation.

We reported our results from the computational model using the position of the wing's tips and strain near the wing's base. The right and left wing tip positions (D_R and D_L, respectively) are given by

$$D_R = \begin{bmatrix} -a & 2b & w(-a,2b,t) \end{bmatrix}^T \tag{4.8a}$$

$$D_L = \begin{bmatrix} a & 2b & w(a,2b,t) \end{bmatrix}^T \tag{4.8b}$$

where a is half of the chord length, b is half of the span length, and $w(x,y,t)$ is the deformation found above. In addition, the strain is given by

$$\vec{\varepsilon}(x,y,t) = -\frac{h}{2}\left[\begin{array}{ccc} \frac{\partial w(x,y,t)}{\partial x^2} & \frac{\partial w(x,y,t)}{\partial y^2} & 2\frac{\partial w(x,y,t)}{\partial x \partial y} \end{array}\right]^T \tag{4.9a}$$

$$\vec{\varepsilon}(x,y,t) = -\frac{h}{2}\left[\begin{array}{ccc} \varepsilon_{xx}(x,y,t) & \varepsilon_{yy}(x,y,t) & \varepsilon_{xy}(x,y,t) \end{array}\right]^T \tag{4.9b}$$

where h is the thickness of the wing, $\varepsilon_{xx}(x,y,t)$ is normal strain in the x-direction, $\varepsilon_{yy}(x,y,t)$ is normal strain in the y-direction, and $\varepsilon_{xy}(x,y,t)$ is shear strain in the x-y plane.

4.3.2 *Robotically actuated model with position tracking*

To validate the results of our computational model we built a robotic actuator to oscillate a model insect wing in a flapping motion while also rotating it about an orthogonal axis (figure 4.3). This experimental setup was used to measure the displacement of the tips of a model wing actuated in air.

By optically tracking the position of the wing, we measured the dynamics of wing deformation during a combination of flapping and body rotation. Our model wing consisted of a 50 mm by 25 mm acrylic sheet with a flexural stiffness of 10^{-5} Nm^2 that well approximated a *Manduca* forewing (Combes and Daniel 2003a). To track bending during each trial, we drew a 5 by 9 grid of fiduciary markers on our wing model with correction fluid (figure 4.3b). The model wing was attached to the shaft of a servomotor controlled by a length driver (Model 305B Dual-Mode Lever Arm System, Aurora Scientific Inc., Aurora, ON, Canada) and the frequency and amplitude of the flapping oscillation were controlled with a function generator (3311A Function Generator, Hewlett-Packard, Palo Alto, CA). The oscillation amplitude (15°) was constrained by the motor power and was lower than that of *Manduca*. However, the wing was flapped at the typical *Manduca* wingbeat frequency of 25 Hz.

We secured the robotic actuator onto a rigid aluminum frame that was mounted to a stepper motor (Hinterwirth and Daniel 2010). To be consistent with our computational model, the rotation of this motor was controlled using a custom Arduino script that generated a 10°, 3 Hz sinusoid about the z-axis via a micro-step controller (G201, GeckoDrive Inc., Tustin, CA). We mounted a high-speed camera (Phantom Miro, Vision Research, NJ, USA) to the frame and

recorded at 500 frames s^{-1}, with a 400μs shutter speed. An orthogonal view of the wing was provided by a mirror attached to the frame above the model wing in the view of the camera.

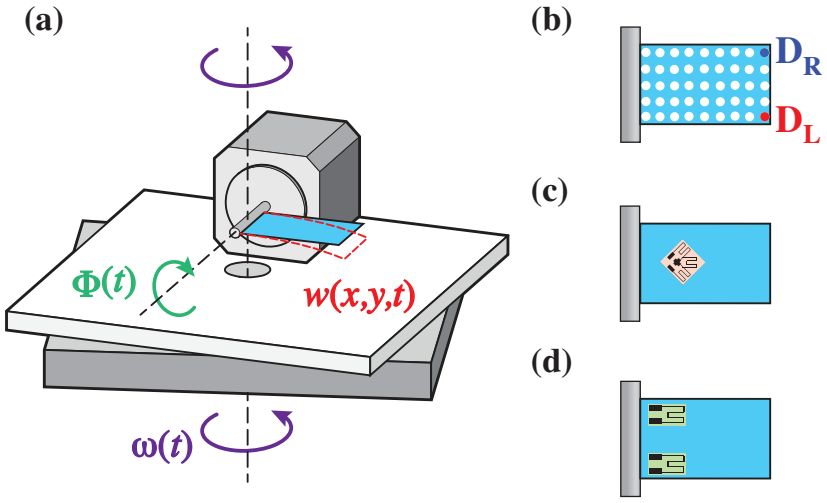

Figure 4.3. Diagram of the robotically actuated wing setup (a), where *F(t)* is the flapping input and *ω(t)* is the angular velocity input about the vertical. The model wing is viewed from the side and a trace of its displacement, *w(x,y,t),* (dashed red line) corresponds to *w(x,y,t)* in the computational model (see figure 4.2). To measure displacement, the wing model was marked with correction fluid to create a 5 by 9 grid of fiduciary markers (b). To measure strain, strain gauges were adhered to the wing's surface. In the case of shear strain, a single rosette was placed at about ¼ span along the mid-chord (c). When evaluating normal strain, two linear strain gauges were applied to either side of the wing's base (d).

We measured wing tip motions under the following conditions: flapping alone, rotation alone, and flapping and rotation. All trials were conducted for 10 seconds to allow the system to reach steady state motion. We digitized the videos using a custom MATLAB script (The MathWorks, Natick, MA, USA), tracking six points on the model wing: the free ends of the top and bottom of the wing, and the two corners at the base of the wing. To be consistent with the results from our computational model, these values were reported using the variables D_R for the right wing tip and D_L for the left wing tip (see equations 4.8a,b).

4.3.3 *Robotically actuated model with strain measurement*

A second experimental system allowed us to measure model wing strain during a combination of flapping and rotation about the *z*-axis. The model wing consisted of a piece of 50 mm by 25 mm

acrylic with a thickness of 127 μm. To measure shear strain, we glued a 350 Ω rosette strain gauge (SGD-2/350-RY53, Omega Engineering Inc., Stamford, CT, USA) to the wing at about 1/4 of the span along the mid-chord (figure 4.3c). The rosette was placed such that two of the strain gauges in the rosette were aligned at 45° to the span with the remaining gauge coincident with the mid-chord. Since our primary interest was to detect shear strain caused by torsion, recordings were only taken from the two strain gauges oriented at 45° to the span. For the measurement of normal strain, we glued two 350 Ω linear strain gauges (KFH-3/350-C1, Omega Engineering Inc., Stamford, CT, USA) onto either edge of the chord at the base of a separate model wing (figure 4.3d). In all cases, the strain gauges were connected in separate quarter-bridge configurations so that we could measure the strain of each gauge independently.

The model wing was attached onto a camshaft setup designed to produce sinusoidal motion (25 Hz, 15°) using the previously mentioned function generator. As in the prior experimental setup, the system was actuated in air with periodic (3 Hz, 10°) rotation about the z-axis. We measured wing strain under the same conditions as the prior setup: flapping alone, rotation alone, and flapping and rotation. Signals from the strain gauges were amplified 100x (Transbridge 4M, WPI, Sarasota, FL, USA) and sampled at 5 kHz (USB-6008, National Instruments, Austin, TX, USA).

4.4 RESULTS

Below we summarize computational results for flapping wings subject to constant yaw rotation as well as periodic yaw (z) rotations. The latter are compared to experimental results for flapping wings subject to periodic yaw rotations.

4.4.1 *Torsional deformation emerges from a combination of flapping and constant yaw rotation in the computational model*

Simulations from the computational model revealed that wings subject to both flapping (25 Hz, 15°) and constant yaw rotation (ω_c = 800°/s) exhibit torsional deformations (figure 4.4). These results are seen in the temporal pattern of tip displacements (D_R and D_L). The difference between these displacements (*i.e.* the relative tip displacement, $D_L - D_R$) (figure 4.4c) is about 100 times smaller than the absolute tip displacement (figure 4.4a). Though small, this difference in the displacement of the two wing tips during concurrent flapping and rotation (solid line in figure

4.4c) is indicative of wing torsion. This phenomenon is not seen in either pure flapping or pure rotation (dashed line in figure 4.4c). Moreover, the double peaks in the sinusoidal pattern of deformation during flapping and rotation (dashed lines in figure 4.4c) occur at twice the flapping frequency and are therefore a signature of the Coriolis force. Indeed, when we reverse the direction of the angular velocity (*i.e.* ω_c = -800°/s), the peaks that occur at twice the flapping frequency due to the Coriolis force also reverse sign (figure 4.4d).

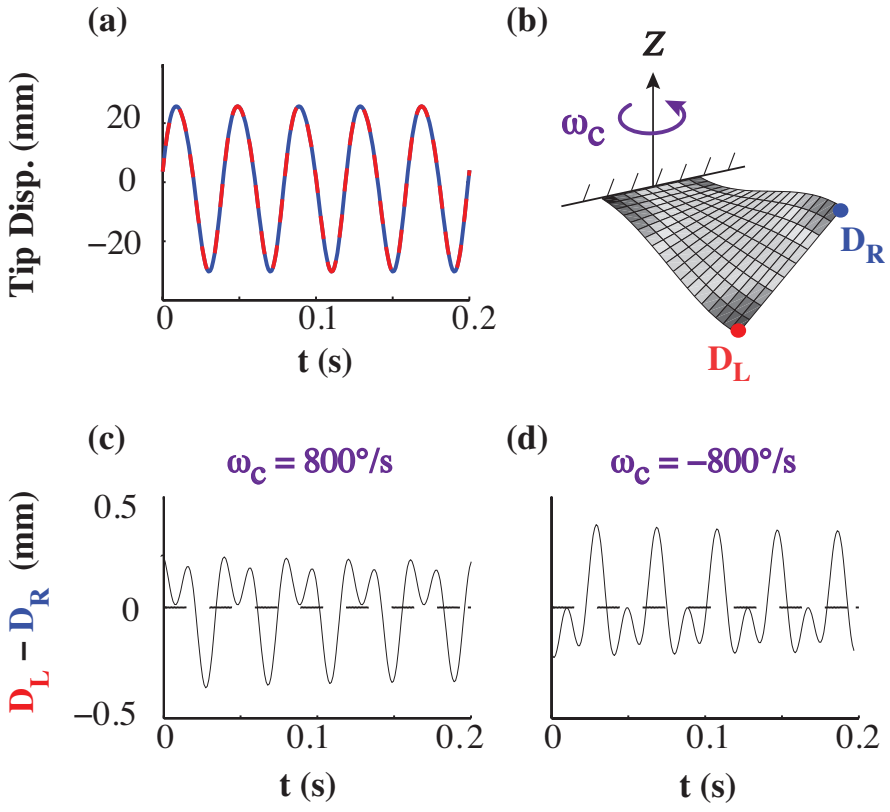

Figure 4.4. The displacements of the left (D_L, solid red) and right (D_R, dashed blue) wingtips of the computational wing model are very similar over time, t, for flapping alone (a). When the wing twists due to an applied constant rotation, ω_c, illustrated in (b), the difference between these two tip displacements changes. This difference is effectively zero when the wing is just flapping (dashed lines in (c) and (d)). However, when the wing is flapping while also rotating (solid lines in (c) and (d)), the difference in tip displacement oscillates at wingbeat frequency and twice wingbeat frequency. When the sign of the rotation is reversed, the signature at twice the wingbeat frequency (indicative of the Coriolis force) also reverses sign (d).

To further explore the dynamics of Coriolis-induced wing torsion, we plotted the differences in wing deformation and strain with and without constant yaw rotation at several snapshots in time during a single period of flapping (figure 4.5). While the differences in normal strain in the span-wise (y) direction (figure 4.5c) and shear strain in the x-y plane (figure 4.5e) are of the same order of magnitude (0.001% strain), the difference in the normal strain along the chord-wise (x) direction (figure 4.5d) is about 100 times smaller. This difference in chord-wise normal strain is due to changes in span-wise lengthening generated by the tiny centrifugal forces produced by wing flapping combined with the Poisson effect: the model wing compresses in the chord-wise direction as it is stretched in the span-wise direction. As a result, the largest differences in chord-wise normal strains are near at the tip of the wing because that is where the span-wise lengthening is greatest.

Additionally, the difference in normal strain in the span-wise (y) direction displays peak regions that oscillate from side-to-side near the base of the wing. On the other hand, the difference in shear strain is largest in the center of the wing. These observations are consistent with theoretical results for a plate undergoing torsion (Reissner and Stein 1951): maximum shear strain occurs at the center of the plate and maximum normal strain along the span-wise direction occurs at the base of the plate. Thus, when the plate undergoes rotation while flapping, a new mode of deformation appears: torsion.

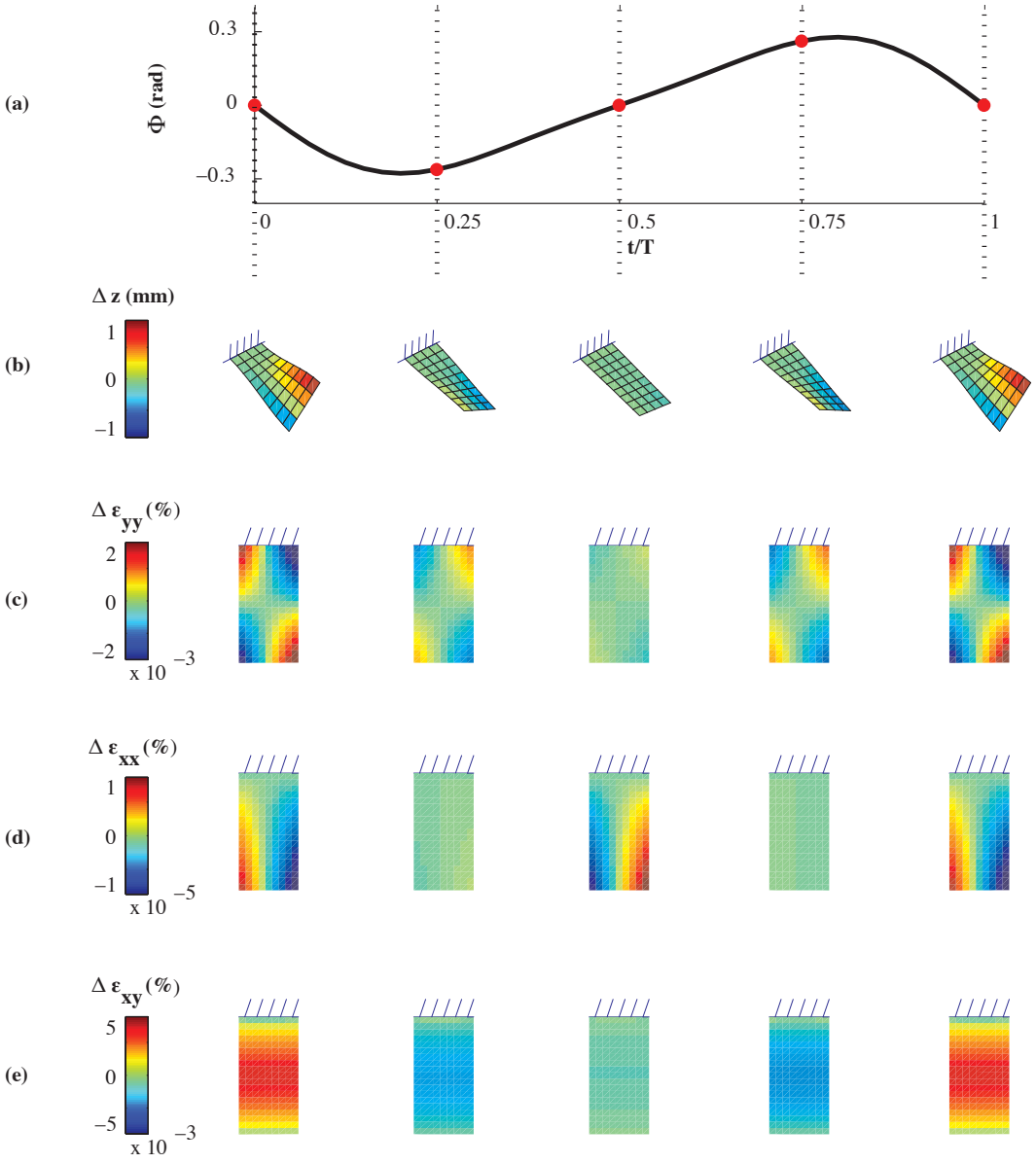

Figure 4.5. Torsion emerges in the computational model when the wing is flapped while it is also rotated at constant angular velocity of 800°/s. As shown in (a), the input flapping angle, Φ, varies over the relative time in the flapping cycle, t/T. The displacement of the model wing and the strain at its surface change in both space and time. At several snapshots in time (indicated by the filled circles and dotted vertical lines in (a)), spatial contours of the difference between flapping and rotating versus flapping alone are shown for four parameters: displacement, Δz (b); normal strain along the y-axis, $\Delta\varepsilon_{yy}$ (c); normal strain along the x-axis, $\Delta\varepsilon_{xx}$ (d); and shear strain in the x-y plane, $\Delta\varepsilon_{xy}$ (e). Colouring refers to the magnitude of each parameter as indicated by the colour bars on the far left.

4.4.2 *Wing tip deformation reveals torsion in flapping wings subject to periodic yaw rotation in both computational and physical models*

As mentioned above, for both experimental convenience and biological relevance, we examined tip deformations in both computational and experimental wings subject to a combination of flapping and periodic yaw rotations. This approach provided a direct validation of our computational results. Since our robotic models were actuated in air, they also include aerodynamic loading and therefore allow us to examine the relative impact of aerodynamic forces. Since prior work showed that aerodynamic forces do not contribute substantially to wing bending at the scale of *Manduca* (Combes and Daniel 2003b), we expected our experimental and computational results for wing torsion to be very similar.

Indeed, we observed strong similarities between the relative tip displacement (*i.e.* difference between the model wing's two free ends, ΔD) of our computational and experimental results (figure 4.6). When subject to flapping alone, the relative tip displacement is zero for the computational model (figure 4.6a). While the relative tip displacement during flapping alone is not exactly zero in the physical experiment, it is quite small (~5 μm) and rather noisy (figure 4.6d). In contrast, during the combination of flapping and rotating about an orthogonal axis, the relative tip displacement is much larger (~50 μm) and strongly periodic (figure 4.6e). This result holds true for both the computational (figure 4.6b) and robotic (figure 4.6e) models.

To determine the frequencies present in these periodic signals, we computed the fast Fourier transforms (FFTs) of the relative tip displacements and evaluated the difference between the amplitudes of the FFTs for flapping alone and flapping and rotating (see supplementary material for further explanation). Our results show strong peaks at the imposed flapping frequency of 25 Hz ± rotation frequency (3 Hz) for both our computational and physical models (figure 4.6c,f). This phenomenon, known as amplitude modulation, results from the Coriolis force, which is proportional to the angular velocity (a sine wave at rotation frequency) crossed with the velocity of the wing (a cosine wave at wingbeat frequency). Using the product-to-sum trigonometric identity,

$$\sin(\alpha)\cos(\beta) = \frac{\sin(\alpha+\beta)+\sin(\alpha-\beta)}{2} . \qquad (4.10)$$

Thus, the Coriolis force causes torsional oscillations at wingbeat frequency, modulated by the rotation frequency. Moreover, the magnitudes of these oscillations in relative tip displacement (figure 4.6c,f) are about three orders smaller than the absolute tip displacement (~30 mm).

4.4.3 *Torsion caused by rotational perturbations of flapping wings is reflected in wing strain*

The Coriolis-induced torsion that we observed via relative wing tip displacement is also reflected in the spatiotemporal patterns of shear and normal strain. For both flapping alone and flapping with imposed periodic body rotation, our computational and experimental results exhibit periodic shear (figure 4.7) and normal (figure 4.8) strain. Shear strain, as measured near the base of the wing at the mid-chord, is on the order of 0.01% strain. On the other hand, normal strain, as measured in the span-wise direction at either side of the wing base, is an order of magnitude larger (0.2% strain). As expected, when the wing is subjected to body rotation alone, both shear and normal strain are zero (data not shown). In all cases, the experimental and computational models exhibit equivalent strain dynamics.

The difference between flapping with versus without body rotation for both shear and normal strain is difficult to discern looking at the two signals side by side (*e.g.* figures 4.7a,b and 4.8a,b). Since the experimental results for pure flapping versus combined flapping and rotating are not phase-matched, we cannot perform a simple subtraction. As such, we instead computed the FFTs of the strains under each condition and then computed the difference between the magnitudes of the FFTs. We performed this analysis separately for both shear and normal strain under the two conditions of flapping with and without body rotation (figures 4.7c,f and 4.8c,f). Similar to the displacement (figure 4.6), both shear and normal strain exhibit sharp peaks at the wingbeat frequency ± the rotation frequency and its first harmonic. The experimental results also have additional peaks at wingbeat frequency and its harmonics, which are likely due to our inability to exactly control the flapping frequency in the experiment (*e.g.* less than 1% difference in frequency causes the difference of the FFTs to have large peaks at the flapping frequency – see supplementary material).

Our computational results for periodic yaw (z) rotation also show spatiotemporal patterns of shear and normal strains on the surface of the wing that are similar to those noted above for constant rotation (figure 4.5). As for constant rotation, the maximum and minimum values of the

difference span-wise normal strains between flapping and rotating versus flapping alone oscillate near the base of the wing (see supplementary material). Moreover, as during constant rotation, the maximum and minimum values of the difference in the shear strains between flapping with versus without periodic rotation are largest at the center of the wing. However, in the case of periodic rotation, the magnitude of the strain varies at both the wingbeat frequency and the frequency of the yaw rotation.

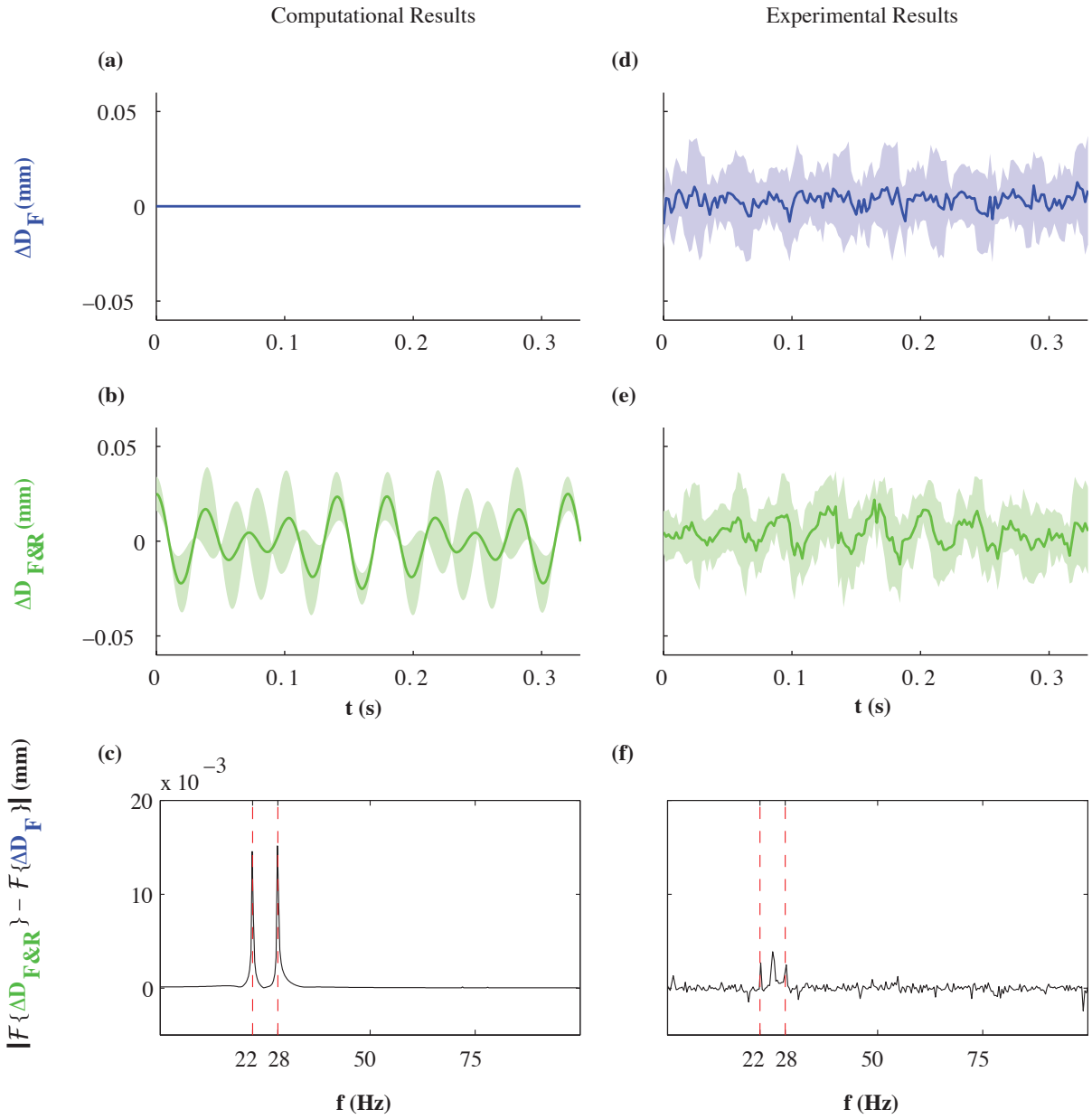

Figure 4.6. The difference between the displacement of the left (D_L) and right (D_R) endpoints of the wing, ΔD, versus time, t, for flapping alone (a,d) and flapping and rotating with periodic angular velocity (b, e). The subscripts of ΔD are F for flapping alone and $F\&R$ for flapping and rotating. Time domain results for a time-average taken over ten rotation cycles are shown for computational (a-b) and experimental (d-e) models. Shading denotes standard deviation. Frequency domain results of the difference in amplitude of the fast Fourier transforms (FFTs) of ΔD for flapping and rotating compared to flapping alone for the computational (c) and experimental (f) models. Note the peaks at the flapping frequency of 25 Hz, plus and minus the rotation frequency of 3 Hz.

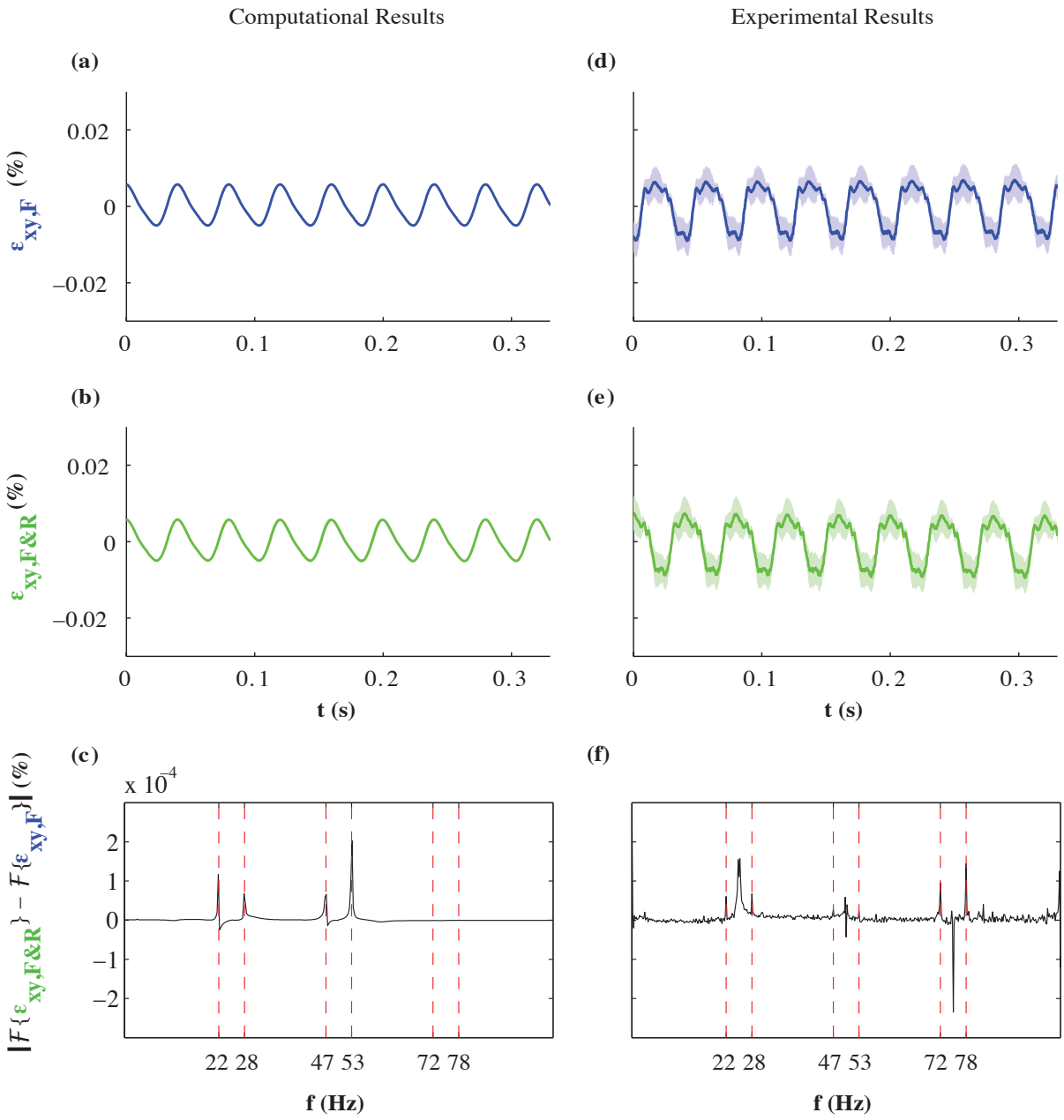

Figure 4.7. The shear strain at the quarter span along the mid chord ε_{xy} versus time, t, for flapping alone (a,d) and flapping and rotating with periodic angular velocity (b,e). The additional subscripts of ε_{xy} are F for flapping alone and $F\&R$ for flapping and rotating. Time domain results for a time-average taken over ten rotation cycles are shown for computational (a-b) and experimental (d-e) models. Shading denotes standard deviation. Frequency domain results of the difference in amplitude of the fast Fourier transforms (FFTs) of ε_{xy} for flapping and rotating compared to flapping alone for the computational (c) and experimental (f) models. Note the peaks at the flapping frequency of 25 Hz, plus and minus the rotation frequency of 3 Hz, and their harmonics.

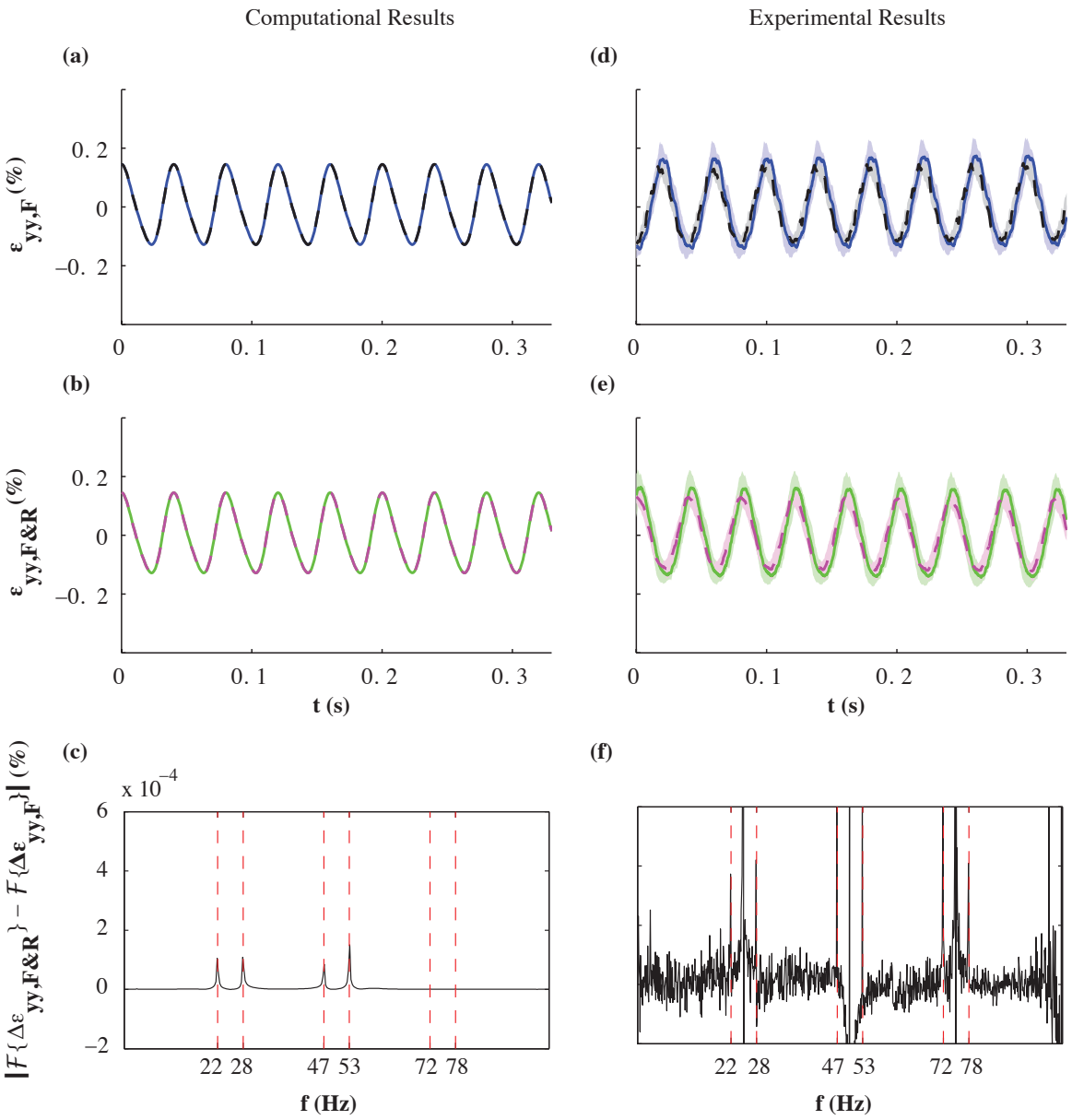

Figure 4.8. The normal strain along the span wise direction, ε_{yy}, on either side of the wing's chord (lift side - solid; right side - dashed) near the base of a model wing versus time, t, for flapping alone (a,d) and flapping and rotating with periodic angular velocity (b,e). The additional subscripts of ε_{yy} are F for flapping alone and $F\&R$ for flapping and rotating. Time domain results for a time-average taken over ten rotation cycles are shown for computational (a-b) and experimental (d-e) models. Shading denotes standard deviation. Frequency domain results of the difference in amplitude of the fast Fourier transforms (FFTs) of the difference between the left and right normal strains, $\Delta\varepsilon_{yy}$, for flapping and rotating compared to flapping alone for the computational (c) and experimental (f) models. Note the peaks at the flapping frequency of 25 Hz, plus and minus the rotation frequency of 3 Hz, and their harmonics.

4.5 DISCUSSION

As flapping, flexing, and flight-force generating structures, insect wings are subject to a host of aerodynamic and inertial forces. These forces, in turn, interact with the wings' structural dynamics to generate complex spatial and temporal patterns of deformation. In this study, we undertook a series of computational and experimental approaches to investigate how such patterns of wing deformation depend upon body rotations. Our work was motivated, in part, by the notion that wings, as evolutionary antecedents of halteres, might themselves provide information about body dynamics. Additionally, biological systems might provide inspiration for new ways to generate gyroscopic sensory devices.

Our goal here is to reveal the principles that govern the structural dynamics of flapping insect wings during body rotations. As a result, we only considered simplified flapping kinematics and assumed a flexible plate of uniform stiffness and mass distribution. In actuality, insect wings are neither homogeneously stiff (Combes and Daniel 2003c) nor do they have uniform mass distribution. Factoring in these characteristics may affect the torsional dynamics and change the strain distribution on wings. Regardless, we have uncovered a unique mechanism that easily enables the wings to detect information previously thought to require complex neural processing (Chan *et al* 1998).

Here we found that flapping, flexible wings subject to rotations about an orthogonal axis reveal a pattern of torsional deformation not noted previously. In addition, wings exhibit periodic normal and shear strains that are a direct consequence of the Coriolis forces acting on them. During rotations, these changes in strain could stimulate embedded mechanoreceptors and trigger correctional reflexes. In this way, insect wings would serve a role similar to halteres, the prototypical biological gyroscopes.

4.5.1 *Insect wings undergo torsion during body rotations, resulting in spatiotemporally varying strain*

Whereas a great deal of effort has gone into understanding the causes of wing bending, torsion in insect wings has received far less attention. Much of the focus in this regard pertains to measuring the torsional stiffness of insect wings (Wooton 1993) or understanding the basis for torsion during hovering flight (Ennos 1988). Ennos (1988), for example, concluded that torsion

in hoverfly wings was due primarily to inertial forces. But inertial forces in a rotating reference frame arise from both rectilinear and rotational accelerations, one of which is the acceleration arising from the superposition of orthogonal rotational motions (the Coriolis acceleration). Thus, the inertial forces that result from body rotations could cause wing torsion and thereby convey information about rotation rate.

Our computational results reveal a complex spatiotemporal pattern of strain that arises when flapping wings are subject to rotation about an axis orthogonal to their flapping, as during a body rotation. Whether we simulate constant or periodic body rotation, three key results emerge. First, wings undergo a large bending deflection along the span driven by inertial bending moments produced by flapping. This result is consistent with prior studies highlighting the dominant role of inertial and elastic mechanisms underlying wing and haltere deformation (Pringle 1948, Nalbach 1993, Daniel and Combes 2002 , Combes and Daniel 2003b, Thompson *et al* 2008). Second, superimposed upon that large bending deformation is a smaller torsional deformation that is seen in the difference of the tip displacement at the corners of our rectangular wing. In contrast to the minuscule lateral deflections suggested for halteres subject to Coriolis forces, the high lateral second moment of area of wings prohibits any such deformation and thus torsion emerges. Third, wing torsion appears as periodic patterns of shear and normal strains distributed over the wing surface. In contrast to normal strains, where the dominant signal arises from in-plane bending, shear strains directly measure torsion and are insensitive to the large in-plane bend.

4.5.2 *Changes in wing strain could stimulate mechanosensors, enabling insects to detect body rotation*

In halteres, the detection of Coriolis forces is thought to require extreme directional sensitivity of the campaniform sensilla in order to respond to exceedingly small lateral deflections in the presence of large in-plane bending moments that result from haltere flapping (Fraenkel and Pringle 1938, Pringle 1948). While such sensitivity has been suggested for haltere campaniform sensilla (Zill and Moran 1981), wing campaniform sensilla are highly unlikely to experience lateral deflections analogous to those suggested for halteres. Perhaps alternate mechanisms, which combine our results with previous results on the neural timing precision of campaniform sensilla, suggest other ways to detect Coriolis forces.

One possible mechanism could involve detecting the temporal separation of peak strain as opposed to changes in strain magnitude. We show that the magnitudes of peak normal strains at the wing base are large and that the small differences that arise from Coriolis-induced torsion result in shifts in the timing of peak strain. As has been suggested for halteres (Fox *et al* 2010), this spatiotemporal pattern of wing strain could be encoded by the nervous system using subtle shifts in the phase of firing of campaniform sensilla across the wing. While this encoding strategy would require a high level of temporal precision from wing campaniforms, high temporal precision is a hallmark of campaniform sensilla on halteres (Chapmapn *et al* 1979, Dickinson 1990a, Dickinson 1990b, Fox and Daniel 2008, Fox *et al* 2010) and wings (Dickerson *et al* 2014). In fact, the detection of the wing torsion dynamics that we observed is well within the encoding bandwidth limits of campaniform sensilla. Moreover, recent computational work suggests that the incorporation of neuronal filters, which capture aspects of a signal's time history, onto the strain field of a flapping flexing plate enhances the ability to detect body rotation (Brunton *et al* 2014). Thus, rather than relying on magnitude alone, gyroscopic sensing may require an encoding strategy that includes both the spatial and temporal aspects of strain.

No matter how the strain sensing occurs, this unique sensory role through the process of actuation would make the wing both a sensor and an actuator. That is, by flapping for propulsion and maneuverability, the wing and its embedded campaniform sensilla could detect phenomena during perturbations or maneuvers that would be otherwise unavailable to the animal. This sensory role for the wings could predate their evolutionary modification into halteres, organs with a demonstrated capability for sensing angular velocity.

4.6 CONCLUSIONS

We propose that insects can detect the angular velocity of their body via changes in the structural dynamics of their wings. Through the development of computational and robotically actuated wing models, we show that torsion emerges when a flapping, flexing wing is subject to body rotations. This torsion leads to an increase in strain over the wing's surface, which could stimulate the campaniform sensilla embedded in the wing and thereby trigger compensatory reflexes. Thus, we demonstrate that there is indeed a unique structural dynamic mode that develops in the wing, which could inform an insect about its body dynamics.

These results have broad implications for our understanding of biological gyroscopes and for the design of engineered systems. For example, our results indicate that information about body dynamics could be determined by embedding strain gauges directly onto the surface of flexible airfoils already being actuated for propulsion or energy harvesting (*e.g.* micro air vehicles, turbine blades, and helicopter blades). Since the spatiotemporal pattern of strain has implications for optimal sensor placement, future work will examine the extent to which this information might allow us to 1) identify the biological placement of campaniforms on insect wings and 2) inform sensor design for engineered systems. Furthermore, our results suggest that the time has come for a re-examination of the haltere's structural dynamics. Future work will modify prior haltere models to allow for torsional deformation and test hypotheses regarding the importance of temporal encoding.

Through the exploration of biological gyroscopes we have uncovered principles that might be useful for engineering design. Conversely, our use of engineering analysis has provided insight into the form and function of the mechnanosensory structures embedded in insect wings.

4.7 Acknowledgements

BHD and ALE contributed equally to this work. The authors thank Bing Brunton, Eatai Roth, Brian Hinson, and the Daniel Lab for useful discussions and comments on this manuscript. This work was supported by AFOSR grant FA9550-11-1-0155 to TLD as well as the Komen Endowed Chair and ONR MURI grant N000141010952 to TLD. BHD and ALE also received funding from NSF GRFP (DGE-0718124). We have no competing interests.

4.8 Data Accessibility

The code for our computational model and our computational and experimental data are available at https://github.com/eberlea/TorsionWing.

Chapter 5. HALTERES AS TORSIONAL GYROSCOPES

While halteres are the prototypical examples of biological gyroscopes, the majority of flying insects lack them. Yet, many insects are still able to achieve impressive aerial maneuvers and do so with four wings (instead of two wings and two halteres as in dipterans, the true flies). Since halteres are derived from wings, evolution suggests that wings and halteres possess similar rudimentary sensory systems. Indeed, it is difficult to imagine a scenario of haltere evolution where the wings themselves did not provide at least some information about body rotational dynamics.

In Chapter 4, we proposed that insects might indeed be able to sense changes in the torsion of their wings to detect body rotations. However, this torsional mechanosensory mechanism in wings is different than the traditionally accepted out-of-plane bending deformation mechanism in halteres. Thus, while halteres and wings might both sense gyroscopic forces using the same sensory structures, campaniform sensilla, they might monitor rotation by a different mechanism. This difference raises questions about how the gyroscopic sensing capability in halteres evolved.

However, since prior haltere models approximated the haltere as a single point mass, those models could not consider haltere torsion or other dynamics that might result from a distributed mass. As a result, I chose to explore whether halteres might also sense body rotations via torsion. This chapter explores the extent to which distributed mass might allow halteres to sense body rotations via torsion. This chapter contains a manuscript that we are preparing to submit to the *Journal of the Royal Society, Interface*.

5.1 INTRODUCTION

Insects encounter very fast rotational perturbations during flight (Hedrick *et al* 2009). Because flapping flight is an inherently unstable mode of locomotion, flying insects must be able to detect and alter their body dynamics quickly. Since feedback from visual systems is often too slow to provide adjustments to the flight path in response to such perturbations (Land and Collett 1974, Theobald *et al* 2010, Fuller *et al* 2014b), rapid feedback from mechanosensory structures often serves a crucial role in flight stability (Taylor and Krapp 2007).

Flies, for example, use dumbbell-shaped mechanosensory structures, called halteres, to obtain information about their body dynamics (figure 5.1). By flapping their halteres during movement, flies use these mechanosensory organs to detect the motion of their bodies via Coriolis forces, which are directly proportional to body rotation rate (Pringle 1948, Nalbach 1993, Thompson *et al* 2008). Recent work has also shown that wings, the evolutionary antecedents of halteres, might serve a gyroscopic mechanosensory function (Dickerson *et al* 2014, Eberle *et al* 2015). However, the mechanosensory mechanism proposed for wings (*i.e.* torsion) is different than the traditional understanding of haltere mechanosensing (*i.e.* bending).

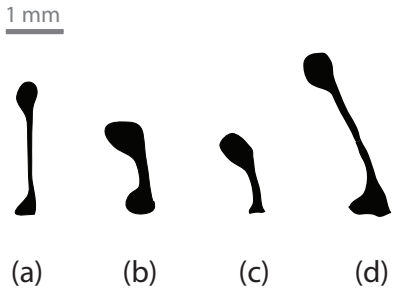

Figure 5.1. Some insect species, particularly the true flies of Diptera, possess halteres, dumbbell-shaped mechanosensory structures that are used to detect body dynamics. As illustrated by traces drawn from photographs, haltere shape varies widely depending on the family of flies: Syrphidae (hover flies) (a), Asilidae (robber flies) (b), Empididae (dance flies) (c), and Tipulidae (crane flies) (d). Note that haltere structures generally have larger bulb-like masses at either end of a thin stalk, and they are also often asymmetric about the long axis (left to right in these drawings).

The dynamics of halteres have been widely studied over the greater part of the last century, and many researchers think that the nature of their gyroscopic sensing capabilities centers upon small out-of-plane bending deflections of the haltere's tip (Pringle 1948, Nalbach 1993, Thompson *et al* 2008). The insect theoretically senses the deflections caused by haltere bending via mechanical sensors, called campaniform sensilla, at the haltere's base. However, while significant behavioral and neurological consequences of haltere motion have been demonstrated (Nalbach 1993, Fox and Daniel 2008, Fox *et al* 2010), the tiny, rotation-induced bending deformations have never been observed experimentally.

Unlike halteres, which are thought to detect gyroscopic forces via bending, wings are thought to detect body dynamics via torsion. However, all prior models of haltere dynamics have

assumed the mass of the haltere to be isolated to a single point mass at the end of a massless rod and have allowed only bending motions (Pringle 1948, Thompson *et al* 2008). As a result, none of these prior models has been capable of determining whether halteres might undergo torsion, which could occur when the mass is distributed, establishing a moment of inertia.

While the bulbs at the tips of halteres do contain a large portion of the halteres' mass, halteres are complex structures with their mass distributed asymmetrically over a large variety of shapes and sizes (figure 5.1). Due to the asymmetric nature of halteres, along with recent evidence that wings respond to body rotations via torsion, the question arises as to whether halteres might use a torsional sensory mechanism similar to wings, their evolutionary predecessors. Thus, we ask: do halteres experience torsion when undergoing concurrent flapping and rotation? If so, how does the torsional displacement compare to the out-of-plane bending component and how much does it change compared to flapping alone?

To address these questions, we developed two models: an analytical model and a finite element model. These models confirmed the results for a haltere traditionally modeled as a point mass on a stick (*i.e.* gyroscopic forces induce out-of-plane bending deformation). However, when we modified the model to incorporate symmetrical and asymmetrical haltere shapes, we also found that gyroscopic forces can induce haltere torsion. Furthermore, depending on the mass distribution of the haltere, these forces could result in torsional displacements that are of similar magnitude to the out-of-plane bending displacements. Thus, our results suggest that halteres and wings may indeed sense torsion using the same structural dynamic mechanism: torsion.

5.2 Materials and Methods

To examine whether halteres might undergo torsion due to gyroscopic forces, we developed two models of a flapping, rotating haltere. The first model used an analytical approach to derive the equations of motion via Lagrangian mechanics (figure 5.2). The second model employed finite element modeling software to accommodate more complex geometries (figure 5.3). Although both of these models are capable of examining rotation about all three axes (x, y, and z), we chose to focus on a single rotation axis: the z-axis, just as we explored for wings in Chapter 4. For both of the models described below, we simulated flapping in the x-z plane with and without a constant rotation about the z-axis.

It is important to note that the engineering methods described here are widely used for modeling the dynamics of complex, flexible, multi-body systems as in aerospace (Meirovitch 1974, Ho 1977, Meirovitch 1975) and robotics (Chu and Pan 1975, Book 1979, Song and Haug 1980). Shabana (1997) provides a thorough review of the methods used to model flexible multi-body dynamics, and Shabana (2013) provides detailed descriptions regarding implementation.

5.2.1 *Analytical Model in MATLAB*

In order to investigate the halteres' ability to sense gyroscopic forces via torsion, we developed a simple computational model that drew upon prior work (Pringle 1948, Nalbach 1993, Thompson *et al* 2008). Instead of allowing for only a single out-of-plane bending degree of freedom as in previous models, we expanded the model to include an additional twisting degree of freedom (figure 5.2a).

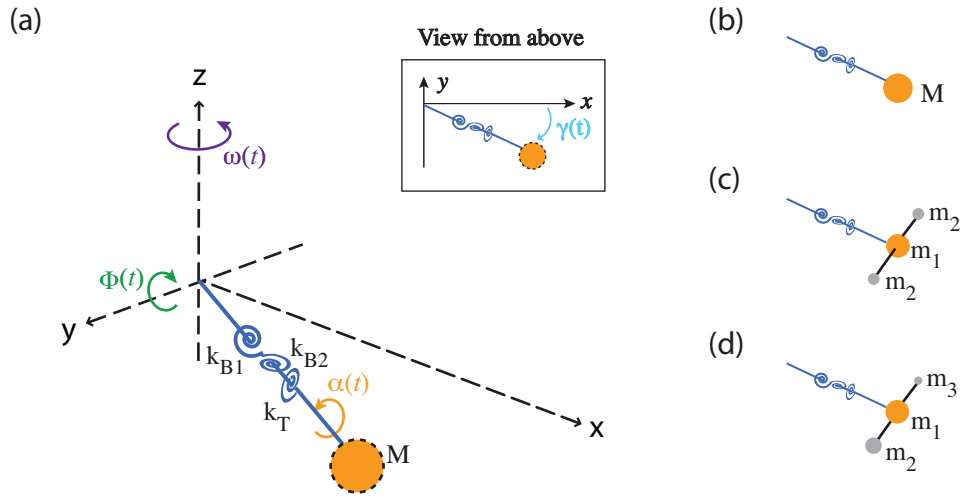

Figure 5.2. Diagram of our haltere model (a) with three types of mass distributions: a single point mass (b), a symmetric distribution of eccentric masses (c), and an asymmetric distribution of eccentric masses (d). The flapping input is prescribed by $\Phi(t)$ and the rotation is given by the angular velocity $\omega(t)$. Three springs are used to describe the stiffness of the haltere: two for bending about the radial and angular axes, k_{B1} and k_{B2}, and one for torsion about the radial axis, k_T. The two degrees of freedom are the torsional displacement angle, $\alpha(t)$, and the out-of-plane displacement angle, $\gamma(t)$. The total mass of at the end of the haltere is given by M. In the asymmetric mass distributions (c and d), the central mass is given by m_1 and the eccentric masses are given by m_2 and m_3 (in these cases total mass is conserved, that is $m_1 + 2m_2 = M$ or $m_1 + m_2 + m_3 = M$).

We formulated the equations of motion for the haltere using Lagrangian mechanics. The first step in such an approach is to derive equations for the kinetic and potential energy and write the Lagrangian function. For our setup, assuming the gravitational force is negligible, the kinetic, T, and potential, V energies are given by

$$T = \frac{1}{2}\sum_{j=1}^{n} m_j \dot{\vec{r}}_j \cdot \dot{\vec{r}}_j \tag{5.1}$$

$$V = \frac{1}{2}k_B\delta_z^2 + \frac{1}{2}k_B\delta_y^2 + \frac{1}{2}k_T\theta^2 \tag{5.2}$$

where m_j is the mass of each point mass, n is the number of point masses (ranges from 1-3), $\dot{\vec{r}}_j$ is the linear velocity of each point mass, k_B and k_T are the bending and torsion spring constants, δ_z and δ_y are the linear displacements in the z and y directions, and θ is the angular torsional displacement as shown in figure 2. The Lagrangian, L, can therefore be written as

$$L = T - V = \frac{1}{2}\sum_{j=1}^{n}\left(m_j \dot{\vec{r}}_j \cdot \dot{\vec{r}}_j\right) - \frac{1}{2}k_B\delta_z^2 - \frac{1}{2}k_B\delta_y^2 - \frac{1}{2}k_T\theta^2. \tag{5.3}$$

where we prescribed the spring constants according to

$$k_B = M\omega_n^2 \tag{5.4a}$$

$$k_T = \frac{Ml^2\omega_n^2}{3(1+\upsilon)}, \tag{5.4b}$$

where M is the total mass of the system, l is the length of the haltere, and ω_n is the natural frequency of the system. For more details about how we determined these spring constants, see Appendix 3.

Using the Lagrange equation, we then solved for the equations of motion as follows:

$$\frac{d}{dt}\left(\frac{\partial L}{\partial \dot{q}_i}\right) - \frac{\partial L}{\partial q_i} = Q_i', \tag{5.5}$$

where L is the Lagrangian function given by equation 5.3, q_i is the i^{th} generalized coordinate, and Q_i' is the i^{th} generalized force. For this problem, we chose our generalized coordinates to be the out-of-plane displacement angle, γ, and the torsional displacement angle, θ (see figure 2a).

We also chose to include damping for both generalized coordinates, such that each generalized force is given by

$$Q_i' = \eta \dot{q}_i \tag{5.6}$$

where η is the damping factor, which is given by $2\zeta\omega_n$. To be consistent with prior work (Thompson *et al* 2008), we set the damping ratio, ζ, equal to 0.1.

After inputting the expressions for the linear velocities and angular displacements, written in terms of the generalized coordinates, into equations 5.1 and 5.2, we solved for the resulting equations of motion. The expressions for linear and angular displacements are given by

$$\vec{r}_1 = \begin{bmatrix} l\cos(\gamma)\cos(\Phi) \\ -l\sin(\gamma) \\ l\cos(\gamma)\sin(\Phi) \end{bmatrix} \tag{5.7a}$$

$$\vec{r}_2 = \begin{bmatrix} R\left(\sin(\theta)\cos(\Phi)+\cos(\theta)\sin(\Phi)\sin(\gamma)\right)+l\cos(\gamma)\cos(\Phi) \\ R\cos(\theta)\cos(\gamma)-l\sin(\gamma) \\ R\left(\sin(\theta)\sin(\Phi)-\cos(\theta)\cos(\Phi)\sin(\gamma)\right)-l\cos(\gamma)\sin(\Phi) \end{bmatrix} \tag{5.7b}$$

$$\vec{r}_3 = \begin{bmatrix} l\cos(\gamma)\cos(\Phi)-R\left(\sin(\theta)\cos(\Phi)+\cos(\theta)\sin(\Phi)\sin(\gamma)\right) \\ R\cos(\theta)\cos(\gamma)-l\sin(\gamma) \\ R\left(\sin(\theta)\sin(\Phi)-\cos(\theta)\cos(\Phi)\sin(\gamma)\right)+l\cos(\gamma)\sin(\Phi) \end{bmatrix} \tag{5.7c}$$

$$\alpha_1 = \theta,\ \alpha_2 = \Phi,\ \alpha_3 = \gamma\ , \tag{5.7d}$$

where l is the length of the haltere and R is the radial displacement of the eccentric masses. To solve for the linear velocities, we evaluated the velocity in the inertial frame via

$$\vec{r}_j = \frac{d\vec{r}_j}{dt} + \vec{\Omega} \times \vec{r}_j\ , \tag{5.8}$$

where the position vectors, $\vec{r}_j$, are given by equations 5.7a-c and the angular velocity vector is given by the components shown in figure 2. as

$$\vec{\Omega} = \begin{bmatrix} 0 \\ 0 \\ \omega(t) \end{bmatrix}. \tag{5.9}$$

Once we formulated the equations of motion, we solved this system of second-order differential equations using a fourth-order Runge Kutta method in MATLAB (The MathWorks, Natick, MA, USA). The initial conditions were assumed to be zero, the solution was obtained for forty flapping cycles, and we prescribed haltere flapping by setting angular displacement about the *y*-axis to be

$$\Phi = A\sin(2\pi f_{flap} t) \tag{5.10}$$

where A is the amplitude of the flapping, f_{flap} is the flapping frequency, and t is time. The amplitude and frequency of flapping were set to $\pi/2$ rad and 200 Hz, respectively, so as be consistent with prior haltere models (Thompson *et al* 2008).

To validate our model, we first simulated the tip of the haltere as a point mass (figure 5.2b) and confirmed that the out-of-plane displacement was consistent with prior work by Thompson *et al* (2008) (see Appendix 3). We then simulated two additional mass distributions such that the tip of the haltere would have either a symmetric (figure 5.2c) or asymmetric (figure 5.2d) rotational moment of inertia. These additional simulations allowed us to explore the extent to which the distribution of the mass modified the dynamics of the haltere and permitted the structure to convey gyroscopic dynamics via torsion.

5.2.2 *Finite Element Model in COMSOL*

To provide further validation of our analytical model and to expand the geometries and mass distributions that we could explore, we also developed a haltere model using COMSOL Multiphysics software (COMSOL AB, Stockholm, Sweden). We used the Multibody Dynamics Module to create a rigid support structure that simulated insect body rotations via a mechanical gyroscope with three concentric rings and a central rod. We then attached a haltere-like flexible structure to the rod at the center (figure 5.3). We actuated the COMSOL haltere model using the same approach as in the analytical model (flapping about the *y*-axis according to equation 5.10 and measuring bending and torsional displacements about the *z*- and *x*-axes, respectively). We also limited our analysis to examine only rotations about the *z*-axis.

To validate this model, we compared our results for the symmetric model against both our analytical model and prior work by Thompson *et al* (2008). For the purposes of this validation, and so as to be consistent with prior work, we set the haltere material properties to steel

(Young's modulus = 200 GPa; density = 7850 kg m^{-3}) so that we could examine the results for limited haltere flexibilities. Due to the high stiffness of the steel material, the out-of-plane bending deformation of the haltere was generated by attaching the haltere to the central flapping actuation rod via a spring about a *z*-axis hinge joint. Using this setup, the out-of-plane deformation results from our COMSOL model were very similar to the results generated by our analytical model and those published by Thompson *et al* (2008) (see Appendix 3).

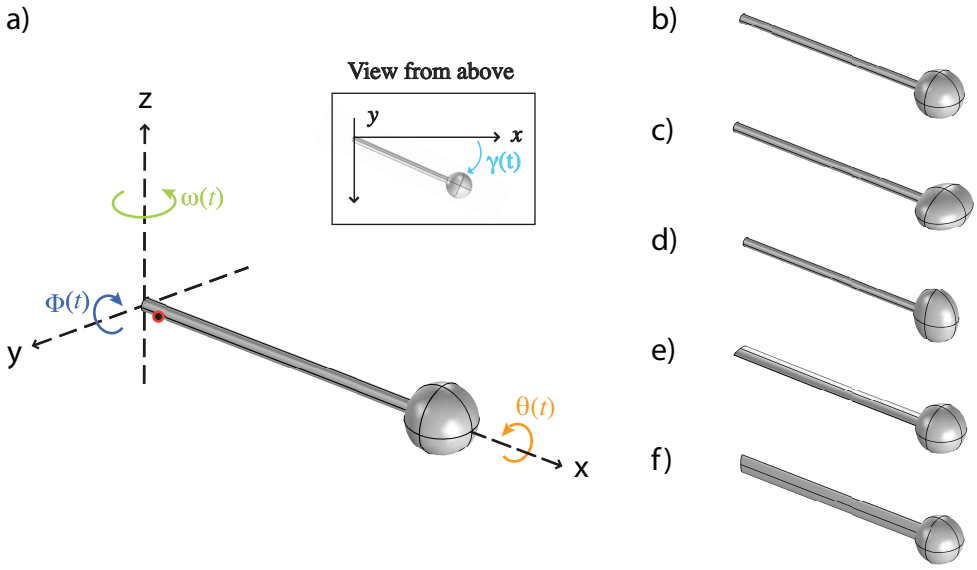

Figure 5.3. COMSOL model of a haltere (a), where the haltere is modeled as an elastic solid. The flapping input is prescribed by Φ(t) and the rotation is given by either the angular velocity ω(t). The torsional displacement angle, θ(t), and the out-of-plane displacement angle, γ(t), change with rotation rate. We considered several different haltere geometries, including a symmetric haltere with a spherical bulb and cylindrical stalk (b), asymmetric halteres with ellipsoidal bulbs oriented perpendicular (c) and parallel (d) to the rotation (*z*) axis, and asymmetric halteres with spherical bulbs and ellipsoidal stalks oriented perpendicular (e) and parallel (f) to the rotation (*z*) axis.

The out-of-plane bending displacements from our analytical model were very similar to those generated by our COMSOL model. However, in addition to out-of-plane bending deformations, our COMSOL model also demonstrated torsional deformations about its length. These torsional displacements result from our COMSOL model's ability for to handle complex distributions of mass rather than the single point masses used in prior studies. In order to ensure convergence of the torsional deformations, we performed simulations using four decreasing

relative tolerances (*i.e.* 1e-4, 1e-5, 1e-6, and 1e-7). From this analysis, we chose to implement a relative tolerance of 1e-7 since the solution for the torsion induced by flapping alone converged to less than 1% of the torsion during flapping with rotation (see Appendix 3). In addition to modeling the haltere as a steel material, we also examined a more realistic haltere material with a Young's modulus of 3 MPa and a density of 1190 kg m^{-3} (similar to acrylic).

Beyond the symmetric haltere (figure 5.3a; spherical bulb and cylindrical stalk), we also investigated four other cases with asymmetric halteres. Two of these cases investigated the importance of the symmetry of the haltere bulb (figure 5.3c-d) and the other two cases examined asymmetry of the stalk (figure 5.3e-f). For both the bulb and stalk, we examined whether the orientation of the asymmetry mattered by considering geometries elongated in either an orientation parallel or perpendicular to the rotation (z) axis. We used the same initial and boundary conditions as described in the analytical model (*i.e.* the flapping input was described by equation 5.10) and solved for the angular displacements due to torsion and bending over twenty flapping cycles.

5.3 RESULTS

Our analytical and COMSOL models of the haltere revealed several interesting results. First, when the mass of a haltere is distributed beyond a single point mass, the haltere develops torsional deformations when is it concurrently flapped and rotated. Second, these torsional deformations occur at twice the flapping frequency and are likely induced by a spatial gradient in the Coriolis force, which is directly proportional to the mass distribution. Third, the bulb's mass distribution appears to play a more significant role than the stalk's distribution in determining the torsional deformations. Finally, the combination of torsional and out-of-plane bending deformations cause in changes in the length-wise normal strain that are largest near the haltere's root.

5.3.1 *Haltere model undergoes torsion due to spatial gradient in Coriolis force*

Both our symmetric analytical and symmetric COMSOL haltere models undergo torsion when they are rotated while flapping (figures 5.4 and 5.6a). What induces this torsion? In the case of the symmetric analytical model with eccentric masses oriented parallel to the rotation axis, this rotation is likely induced by the spatial variation in the Coriolis force, which, in this case of

simplified flapping about the *y*-axis, is orthogonal to the rotation axis (figure 5.5). Since the analytical model with the symmetric masses oriented perpendicular to the rotation axis is likely an unstable configuration (*i.e.* any small perturbation out-of-plane will drive the setup further from this configuration), this setup responds similarly. Thus, if the configuration oriented perpendicular to the rotation axis moves slightly away from its initial orientation, the gradient in the Coriolis force drives it even further from this position. If we expand this concept to consider a spherical distribution of point masses about a central point mass, then we achieve a simplification of the COMSOL model with a continuous spherical mass distribution. Thus, it is likely that the spatial gradient in the Coriolis force that results from the haltere's distributed mass drives the torsion we observe in these models.

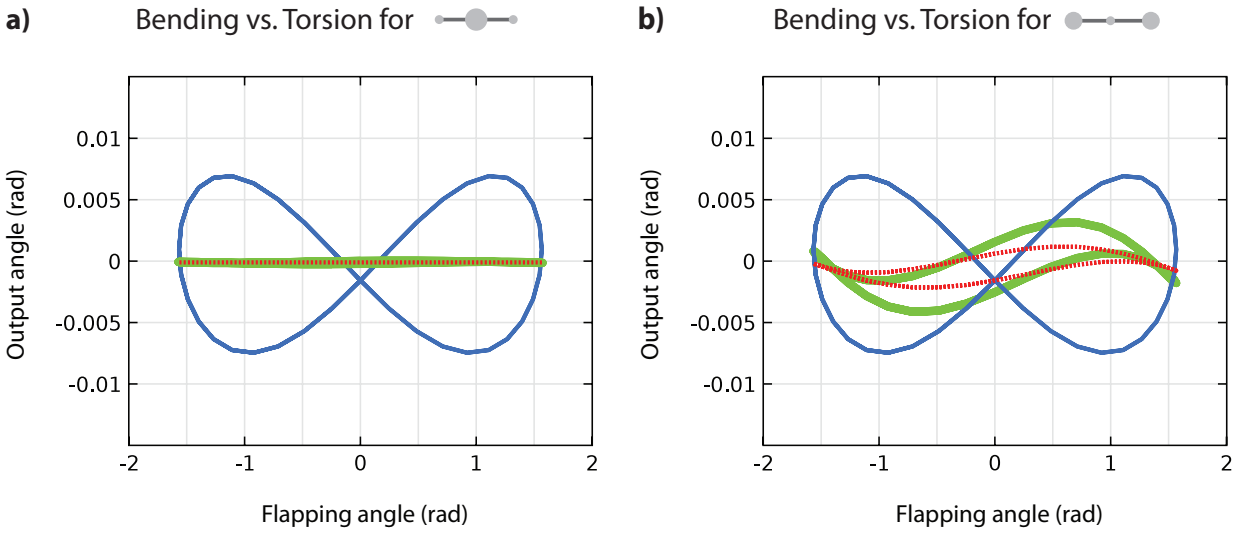

Figure 5.4. Out-of-plane bending (blue lines) and torsion angles (green and red lines) for flapping under constant body rotation about the *z*-axis. In the case of flapping alone, both torsion and bending angles are zero (data not shown). These results are for the symmetric analytical model with eccentric masses oriented perpendicular (green) and parallel (red) to the body rotation axis. The grey drawings above each plot qualitatively indicate the mass distribution as seen from the end of the haltere: most of the mass located at the center (a), and most of the mass located out at the eccentric masses (b). In all cases the total mass is held constant. However, when more of the mass is distributed further out from the central point mass, the torsion angle increases. In some cases, the torsion angle is of similar magnitude to the out-of-plane bending displacement (b).

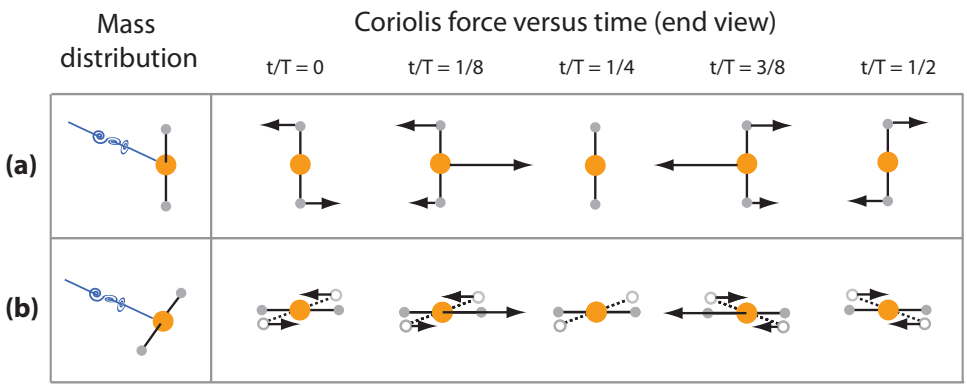

Figure 5.5. Haltere torsion is induced by a spatial gradient in the Coriolis force. For a symmetric mass distribution with eccentric masses parallel to the rotation axis (a), the Coriolis forces on the eccentric masses generate a moment about the central mass. As shown, these forces oscillate at twice the flapping frequency (*i.e.* a full cycle is completed in half the flapping period t/T = 1/2). Similarly, when the eccentric masses are perpendicular to the rotation axis (b), a small perturbation from the equilibrium position will also induce torsion.

5.3.2 *Haltere torsion depends largely on the mass distribution of the bulb*

For the symmetric analytical model, the torsional displacement is highly dependent on the mass distribution (figure 5.5). When the mass is distributed mostly at the center (figure 5.5a), then the torsional displacement is extremely small (green and red lines) as compared to the bending displacement (blue line). However, if more of the mass is distributed out at the eccentric masses, then the torsional displacements are much larger (figure 5.5b). In some cases, the magnitude of the torsional displacement is similar to the magnitude of the out-of-plane bending (figure 5.5b). Furthermore, when a continuous distribution of mass is considered, as in the COMSOL model (figure 5.6a), the torsion amplitude is also similar to the out-of-plane bending.

When we examined the torsion generated by the COMSOL model with asymmetric ellipsoidal haltere bulbs oriented parallel and perpendicular to the rotation axis (figure 5.6b), we found similar results to the analytical model with parallel and perpendicularly oriented eccentric masses (figure 5.5b). When mass is moved from the central mass to the eccentric masses in the perpendicular configuration, then more torsion is generated compared with the symmetric case. When the mass is more distributed along the axis parallel to the rotation, then slightly less torsion is generated as compared to the symmetric case. However, when the geometry of the haltere's stalk is changed, there is very little difference in the torsion generated (figure 5.6c).

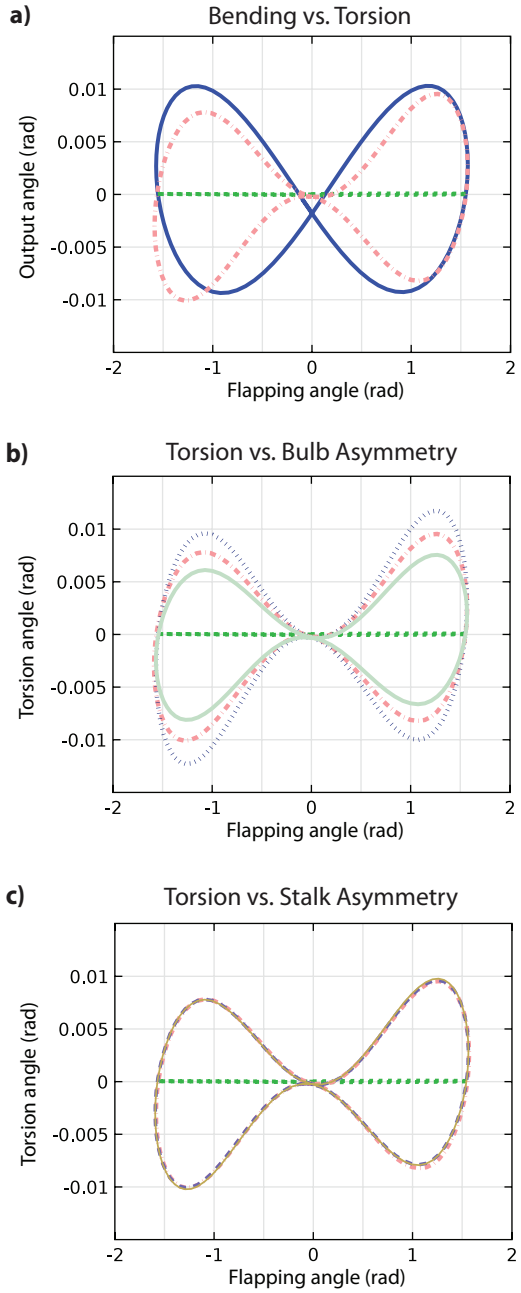

Figure 5.6. Out-of-plane bending (solid line in a) and torsion angles (dash-dot line in a) from the symmetric COMSOL model (figure 3b) for flapping under constant body rotation. When the mass distribution of the bulb is changed to an ellipsoid rather than a sphere, the torsion angle changes (perpendicular ellipsoidal bulb—light dashed; parallel ellipsoidal bulb—solid line; sphere—dashed-dot line;). However, when the shape of the stalk changes, the torsion angle changes very little (c; circular stalk—dashed-dot line, perpendicular ellipsoidal stalk—dashed black, parallel ellipsoidal stalk—solid grey). In all cases, the bending and torsion angles for flapping alone are zero (dashed green lines in a, b, and c).

5.3.3 *Gyroscopic forces induce changes in length-wise normal strain*

While the idea of using torsion and bending angles to measure the gyroscopic forces works well for understanding the dynamics of halteres from an engineering perspective, insects are unlikely to measure these values directly. Instead, insects use strain-like mechanoreceptors called campaniform sensilla. Thus, we were interested to see how the torsion and bending induced by gyroscopic forces might manifest in the spatiotemporal patterns of haltere strain. In order to increase the amount of strain developed in the haltere, we modified the symmetric COMSOL model to use an acrylic-like material (Young's modulus of 3 GPa and density of 1190 kg m^{-3}) rather than steel. The results reported here correspond to this acrylic-like symmetric COMSOL model.

A temporally varying strain pattern emerges in the difference between the length-wise normal strain (strain XX) between flapping with and without rotation at the base of the haltere (figure 5.7a). For this particular material, the difference in the length-wise normal strains is on the order of a ten microstrain (~10 με). As expected, this indicates that the torsion and bending deformations induced by gyroscopic forces do cause changes in the length-wise normal strain. In order to extract the frequency at which these regions of peak strain oscillate, we took a fast Fourier Transform of the signal (figure 5.7b). Although the length-wise normal strain varies primarily at the flapping frequency, the amplitude of the length-wise normal strain at twice the flapping frequency increases when the haltere is rotating as compared to flapping alone (figure 5.7b). Furthermore, while the strain at this particular location was only about ten times larger than the difference in strain between flapping and rotating, the peak strain for the entire structure (flapping with or without rotation) was closer to 100 με. Thus, these results are consistent with prior observations regarding the detection of gyroscopic forces in halteres and wings: the out-of-plane bending deformations in halteres and the torsional deformations in wings are about two orders of magnitude smaller than the deformations due to haltere or wing flapping.

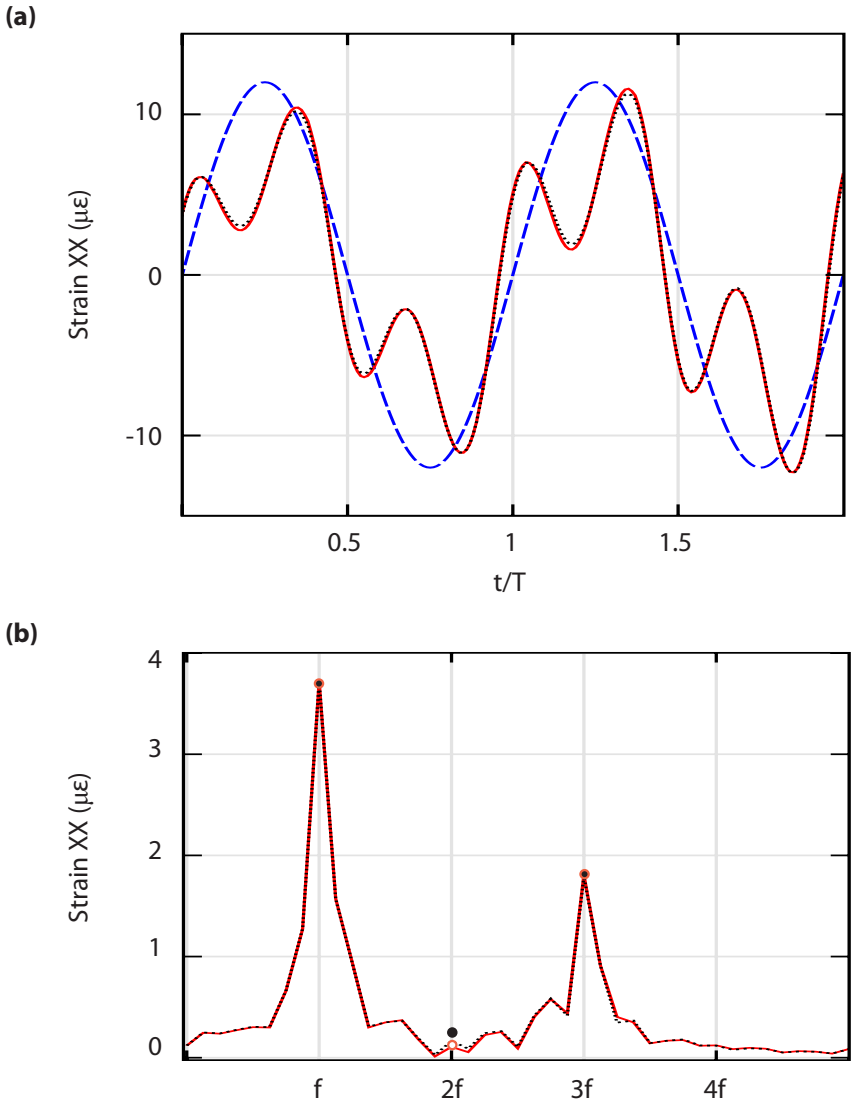

Figure 5.7. The length-wise normal strain (strain XX) measured at one location near the base of the haltere. In the time domain (a), the strain is qualitatively quite similar for flapping alone (solid red) and flapping with rotation (dotted black). The flapping angle (dashed blue) is overlaid for reference. However, when the strain signals are examined in the frequency domain, the amplitude of the strain during rotation (solid black circle) is larger than the strain during flapping alone (unfilled red circle) at twice the flapping frequency. At the flapping frequency and three times the flapping frequency, the strain amplitudes are the same for flapping with and without rotation.

5.4 Discussion and Conclusions

Our results indicate that halteres may indeed twist, and not just bend, when they are simultaneously flapped and rotated. Furthermore, torsion in halteres is highly reliant on the mass distribution of the bulb, and the ratio of torsion to bending is largely dependent upon the second moment of area of the stalk. Still, we show that for haltere models that possess distributed mass, the torsional deformations are of similar magnitude to the out-of-plane bending deformations. We also show that the deformations of the haltere are manifest as changes in the length-wise normal strain. Thus, it might be possible that both halteres and wings use torsion as a mechanosensory mechanism to detect body rotations. This mechanosensory similarity could have substantial implications for describing the evolutionary pathway that led wings to morph into halteres.

5.4.1 *Halteres likely undergo torsion when they are flapped and rotated*

As evidenced by our low-order model of haltere dynamics, it is likely that the asymmetric mass distribution of halteres causes them to undergo torsion when they undergo body rotations while flapping. However, even though the overall magnitude of torsion in these cases may be of the same order as the out-of-plane bending displacements, the difference in torsion between flapping with and without rotation is similar for both asymmetric and symmetric mass distributions. In both cases, the torsion caused by rotation is extremely small—on the order of less than 1 degree, which is similar to the out-of-plane bending displacement. Thus, although halteres probably do undergo torsional displacements when flapping and undergoing body rotations, the change in torsion induced by a body rotation is very small. Still, the torsional displacement is on the same order of magnitude as the out-of-plane bending. Moreover, since halteres are thought to be able to detect these small out-of-plane bending displacements, they may also be able to detect these small torsional deformations. As a result, we conclude that halteres may also be able to sense rotations via torsion.

5.4.2 *Sensitivity to mass distribution has implications for haltere evolution*

Our results also indicate that haltere deformations are very sensitive to changes in mass distribution, particularly with regard to the bulb of the haltere. When the haltere bulb is

transformed from a sphere to an ellipsoid, the torsion angle varies with the orientation of the ellipsoid. When the bulb is oriented perpendicular to the axis of rotation, then the torsion increases, but when it is parallel to the axis of rotation the torsion decreases. If the changes in mass distribution result in increased gyroscopic sensing capabilities in halteres, then the same is likely true for wings. Thus, it is possible that halteres and wings employ a similar sensory mechanism, which is enhanced by certain mass distributions. As such, torsional gyroscopic sensitivity may provide a pathway by which wings could evolve into halteres. Future work will explore the extent to which changes in wing shape and mass distribution might explain the evolution of haltere-shaped structures. In addition, due to the differences associated with other aspects of the form and function of halteres and wings, aerodynamic loading is another key issue that will need to be examined in order to fully understand the evolution of halteres from wings.

5.5 ACKNOWLEDGEMENTS

The authors thank Brad Dickerson, Thomas Mohren, Greg Herschler, and the Daniel Lab for useful discussions and comments on this manuscript. This work was supported by AFOSR grant FA9550-11-1-0155 to TLD as well as the Komen Endowed Chair and ONR MURI grant N000141010952 to TLD. ALE also received funding from NSF GRFP (DGE-0718124).

Chapter 6. AERODYNAMIC VS. GYROSCOPIC FORCES ON WINGS AND HALTERES

While my work has suggested that wing torsion might be a gyroscopic sensory mechanism that would allow wings and halteres to detect their body dynamics, we still do not completely understand how aerodynamic and gyroscopic forces scale with wing and haltere size, shape, and flapping frequency. This chapter will inquire into some of the ideas posed in Chapters 4 and 5 about the nature of gyroscopic sensing in wings and halteres. For example, we proposed that since wings may sense gyroscopic forces using torsion (Chapter 4) and since halteres are derived from wings, we investigated whether halteres might also sense gyroscopic forces via torsion (Chapter 5). Additionally, in the case of a robotic moth-like wing, we showed that the aerodynamic loading had little impact on the inertial/elastic torsion induced by an orthogonal rotation of the body (Chapter 4). Thus, for moth-like wings flapping at moth-specific frequencies, torsion may be a mechanism for gyroscopic sensing. However, for wings of other shapes, sizes, and flapping frequencies, the relative importance of gyroscopic to aerodynamic forces might be quite different. For example, in the case of fly wings it could be that the aerodynamic forces are much larger than the gyroscopic forces, which could drive the need for the development of more sensitive gyroscopic sensory structures, like halteres.

Thus, in the context of my prior work, I was interested to explore how the ratio of gyroscopic to aerodynamic forces varied for halteres and wings of differing size, shape, and flapping frequency. Whereas flapping halteres encounter large inertial forces and produce negligible aerodynamic forces, flapping wings both experience and produce large inertial and aerodynamic forces. This chapter describes a preliminary investigation into the relative scaling of gyroscopic and aerodynamic loads on halteres and wings.

6.1 INTRODUCTION

Unlike insect wings, which serve primarily as actuators that modulate flight forces, halteres—the quintessential examples of biological gyroscopes—experience very small aerodynamic loads. As dumbbell-shaped structures, halteres extend from behind the forewings of dipteran flies and are exquisitely sensitive to rotational perturbations of the body. Although we know that halteres are

derived from wings, the evolutionary pathway for this transition is unclear. Still, evolution suggests that these two structures should share at least some similarities in their fundamental sensory capabilities. However, due to the disparities in the geometries and mass distributions of wings and halteres, and the subsequent differences in aerodynamic and gyroscopic forces, we were interested to explore how these aspects of size and flapping frequency might impact the gyroscopic sensing capabilities of these structures. Thus, we ask: how do the ratios of gyroscopic to aerodynamic forces differ for wings and halteres of varying sizes and flapping frequencies?

To explore this issue, we performed a preliminary evaluation of the relationship between the gyroscopic sensory nature of halteres and their evolutionary predecessors, wings. We prescribed the wing/haltere kinematics and then computed the inertial forces using rigid body dynamics. We then input the kinematics into quasi-steady fluid models of thin plates and spheres to approximate the aerodynamic forces imposed on the structures. We used these models to answer three questions. First, how do the aerodynamic and gyroscopic forces compare for a rigid, flapping, rotating haltere? Second, how do the aerodynamic and gyroscopic forces compare for a rigid, flapping, rotating wing? And, finally, how do these values vary with size and flapping frequency? We found that for moth-like wings, the ratio of Coriolis to aerodynamic forces was more than 100 times larger than in the case of fly-like wings. Thus, it is possible that the design of compliant wings might vary with scale and require a tradeoff between aerodynamic efficiency and gyroscopic sensing capabilities.

6.2 Materials and Methods

We used the principles of rigid body dynamics to solve for the moments generated by the prescribed motion of flapping wings and halteres during a constant orthogonal body rotation. We then input these kinematics into quasi-steady aerodynamic models to evaluate the aerodynamic forces on flapping wings and halteres (see program diagram in figure 6.1). By varying flapping frequencies, wing shapes, and body rotation rates according to experimentally measured values for a range of insect taxa, we explored the relative magnitude of gyroscopic to aerodynamic forces.

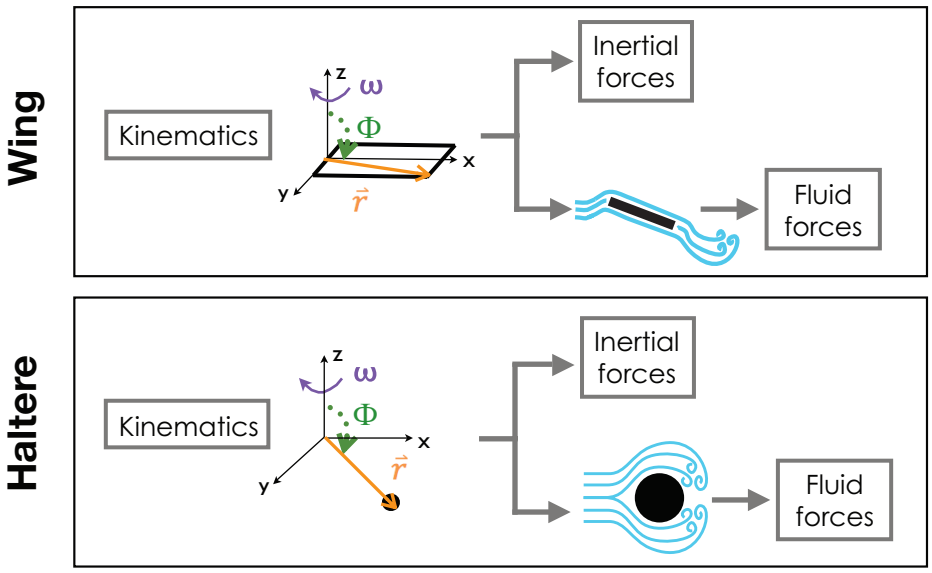

Figure 6.1. Program diagram for simplified model of inertial and aerodynamic forces on an insect wing and haltere. The wing is modeled as a rigid plate segmented into five sections and the haltere is modeled as a single point mass. The kinematics are prescribed using flapping angle, Φ, rotation angle, ω, and position vector, $\vec{r}$. The moments generated by the inertial forces are then computed using equations 6.7-6.9 below. The kinematics are input into a blade element model to compute the fluid forces on the wing. In the case of the haltere, the kinematics are input into a model for drag on a sphere.

6.2.1 *Wing model*

We assumed the wing to be a rectangular rigid plate and prescribed the wing flapping angle, $\Phi(t)$, and body rotation angular velocity, $\omega(t)$, according to

$$\Phi(t) = A_{flap} \sin(2\pi f_{flap} t) \tag{6.1}$$

$$\omega(t) = \omega_c = \frac{d\theta(t)}{dt} \tag{6.2}$$

where A_{flap} is the amplitude of flapping, which we assumed to be π/2 radians, f_{flap} is the frequency of flapping, which was varied from 10-1000 Hz, ω_c is the constant angular velocity of the body, which was varied from 10-25 rad/s, and $\theta(t)$ is the angle of the rotation. Thus, the position of any point on the wing's surface, in the body's reference frame, B, is described by

$$\vec{r}(t) = \begin{bmatrix} x\cos\left(\Phi(t)\right) \\ y \\ x\sin\left(\Phi(t)\right) \end{bmatrix} \tag{6.3}$$

where x and y are the spatial coordinates of any point on the wing's surface, in the wing's reference frame and $\Phi(t)$ is the wing flapping angle as given by equation 6.1.

We approximated the wing by breaking it down into five sections with point masses at the center of mass of each section. Given the input kinematics, we then solved for the forces generated by the flapping motion and the body rotation. For the case of constant angular velocity, the position, velocity, and acceleration of each segment of wing mass in the inertial frame, N, are

$$\vec{p}\big|_N = \begin{bmatrix} \cos\left(\theta(t)\right) & \sin\left(\theta(t)\right) & 0 \\ -\sin\left(\theta(t)\right) & \cos\left(\theta(t)\right) & 0 \\ 0 & 0 & 1 \end{bmatrix} \vec{r}(t) \tag{6.4}$$

$$\vec{v}\big|_N = \left.\frac{d\vec{r}(t)}{dt}\right|_B + \omega(t)\times\vec{r}(t) \tag{6.5}$$

$$\vec{a}\big|_N = \left.\frac{d^2\vec{r}(t)}{dt^2}\right|_B + 2\omega(t)\times\left.\frac{d\vec{r}(t)}{dt}\right|_B + \omega(t)\times\left(\omega(t)\times\vec{r}(t)\right) \tag{6.6}$$

where $\theta(t)$ is the angle of the rotation, $\vec{r}(t)$ is the position of the mass in the body's frame as given by equation 6.3, and $\omega(t)$ is the angular velocity of the body in the inertial frame as given by equation 6.2. The three terms in the expression for the acceleration (equation 6.6) are, from left to right, the flapping acceleration, the Coriolis acceleration, and the centrifugal acceleration. Using these kinematics, we can determine the total moment generated about the root of the wing for each type of force. The moment generated by the flapping force is given by

$$\vec{M}_{flap} = \sum_{i=1}^{5}\left(\vec{r}_i \times \left.\frac{d^2\vec{r}(t)}{dt^2}\right|_B\right). \tag{6.7}$$

The moment generated by the Coriolis force is given by

$$\vec{M}_{Coriolis} = \sum_{i=1}^{5}\left(\vec{r}_i \times \left(2\omega(t)\times\left.\frac{d\vec{r}(t)}{dt}\right|_B\right)\right) \tag{6.8}$$

and the moment generated by the centrifugal force is given by

$$\vec{M}_{centrifugal} = \sum_{i=1}^{5}\left(\vec{r}_i \times \left(\omega(t) \times \left(\omega(t) \times \vec{r}(t)\right)\right)\right). \tag{6.9}$$

In order to compute the moment generated by the aerodynamic force on the wing, we used these positions, velocities, and accelerations to compute the angle of attack of the wing and then solved for the fluid forces using a blade element model. We approximated the fluid forces on each wing segment using literature values for experimentally derived coefficients of lift and thrust

$$C_l = 1.5\sin\left(2\alpha - 0.06\right) + 0.3\cos\left(\alpha - \frac{\pi}{6.9} - 0.03\right) + 0.012 \tag{6.10}$$

$$C_d = 1.4\sin\left(2\alpha - 0.14\right) + 0.3\cos\left(\alpha - \frac{\pi}{5} - 0.7\right) + 1.5 \tag{6.11}$$

where α is the angle of attack of an insect wing. These equations were computed using lift and drag polar plots for low to medium Reynolds number model flapping insect wings (Dickinson *et al* 1999, Sane 2003, Usherwood and Ellington 2002, Hedrick and Daniel 2006). The moments generated by lift and drag forces were then computed by summing over the five wing segments

$$\vec{M}_l = \sum_{i=1}^{5}\left(\vec{r}_i \times \frac{1}{2}\rho A_i C_{l,i} |\vec{v}_i| \vec{v}_i\right) \tag{6.12}$$

$$\vec{M}_d = \sum_{i=1}^{5}\left(\vec{r}_i \times \frac{1}{2}\rho A_i C_{d,i} |\vec{v}_i| \vec{v}_i\right) \tag{6.13}$$

where $\vec{r}_i$ is the position of the *ith* segment in the body's frame, ρ is the density of the air, A_i is the area of the *ith* segment, $C_{d,i}$ and $C_{l,i}$ are the coefficients of lift and drag of the *ith* segment, and $\vec{v}_i$ is the velocity of the *ith* segment in the inertial frame, *N*. We validated this fluid model by computing the flight forces generated by a moth and a fly and comparing them to literature values.

6.2.2 *Haltere model*

We used a very similar approach to construct a simplified haltere model. We assumed that the haltere was comprised of a single point mass at the tip of the haltere. While we showed in

Chapter 5 that this approximation might not be sufficient to reproduce all of the haltere dynamics, the gyroscopic twisting and bending deformations of the haltere are quite small. Thus, the point mass assumption should give us a general sense for the order of magnitude of the gyroscopic forces.

We prescribed the angular position of the haltere in the body's frame according to equation 6.1 and then computed the positions, velocities, and accelerations of the haltere approximated as a point mass at the tip. We solved for the inertial moments generated about the root of the haltere by modifying equations 6.7-6.9 above for a single mass rather than summing over five masses.

To compute the moment generated by the fluid force on the haltere, we assumed the haltere to be comprised of a lone sphere of radius, *R*. According to a curve-fit equation generated by White (1974), the drag generated on a sphere is given by

$$C_d = \frac{24}{\mathrm{Re}} + \frac{6}{1+\mathrm{Re}^{1/2}} + 0.4 \quad , \tag{6.14}$$

where Re is the Reynolds number, which is given by

$$\mathrm{Re} = \frac{\rho|\vec{v}|2R}{\mu} \quad , \tag{6.15}$$

where ρ is equal to the density of the fluid and μ is equal to the dynamic viscosity of the fluid. Thus, the moment generated by the aerodynamic loads on the sphere is given by

$$\vec{M}_d = \vec{r} \times \frac{1}{2}\rho A C_d |\vec{v}|\vec{v} \tag{6.16}$$

where $\vec{r}$ is the position of the tip of the haltere in the body's frame, *B, A* is the cross-sectional area of the sphere, and $\vec{v}$ is the velocity of the haltere in the inertial frame, *N*.

6.3 Results and Discussion

Our results show that in the case of moth-like wings, inertial forces are relatively more important than aerodynamic moments (figure 6.2a). However, for fly-like wings, the relationship is reversed such that aerodynamic moments play a larger role than inertial moments (figure 6.2b). With regard to Coriolis forces, which are directly proportional to angular velocity, the ratio of Coriolis to aerodynamic forces is close to 0.4 in the case of moth-like wings (f_{flap} = 25 Hz, span = 5 cm) and 0.004 in the case of fly-like wings (f_{flap} = 150 Hz, span = 2 mm).

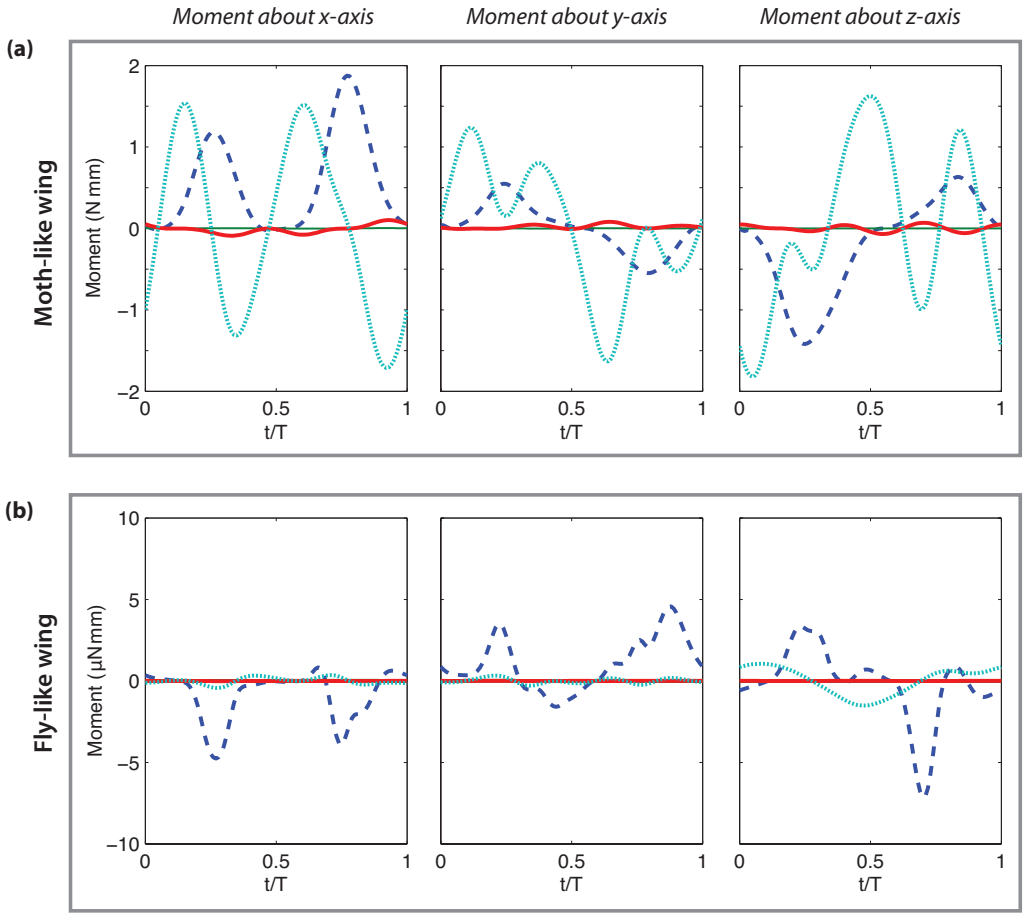

Figure 6.2. Comparison of inertial and aerodynamic moments generated by rigid moth- and fly-like wings. For moth-like wings, the inertial moment due to flapping (dotted light blue line) is comparable to the aerodynamic force (dashed dark blue) and the moment induced by the Coriolis force (solid red) is close to the same order of magnitude as these forces. On the other hand, for fly-like moths, the aerodynamic force dominates and the inertial moments due to flapping and Coriolis are much smaller. In both cases the moment induced by centrifugal forces (thin green line) is extremely small (~100 times < Coriolis force).

6.3.1 *Ratio of Coriolis to aerodynamic moments on wings increases with span and decreases with flapping frequency*

As evidenced by complexity of the results in figure 6.2, it did not make sense to compare the results from a large parameter space in the time domain. Thus, in order to examine how these forces vary with wing size and flapping frequency, we chose to compute the ratio of the amplitudes of the Coriolis to aerodynamic moments in the frequency domain. For simplicity, we

chose to limit our analysis to examine this ratio at the flapping frequency and twice flapping frequency.

Our results indicate that the ratio of Coriolis to aerodynamic moments increases with increasing wingspan and decrease with increasing flapping frequency (figure 6.3). The wingspan causes the ratio to increase because we assume that aspect ratio is held constant and the mass of the wing varies according to a scaling law derived by Greenewalt (1962):

$$m = \frac{A^{1.67}}{2570} \tag{6.17}$$

where A is the area of the wing. Since the aerodynamic moments are directly proportional to area and the inertial forces are proportional to $A^{1.67}$, when the span increases, the ratio of Coriolis to aerodynamic moments also increases.

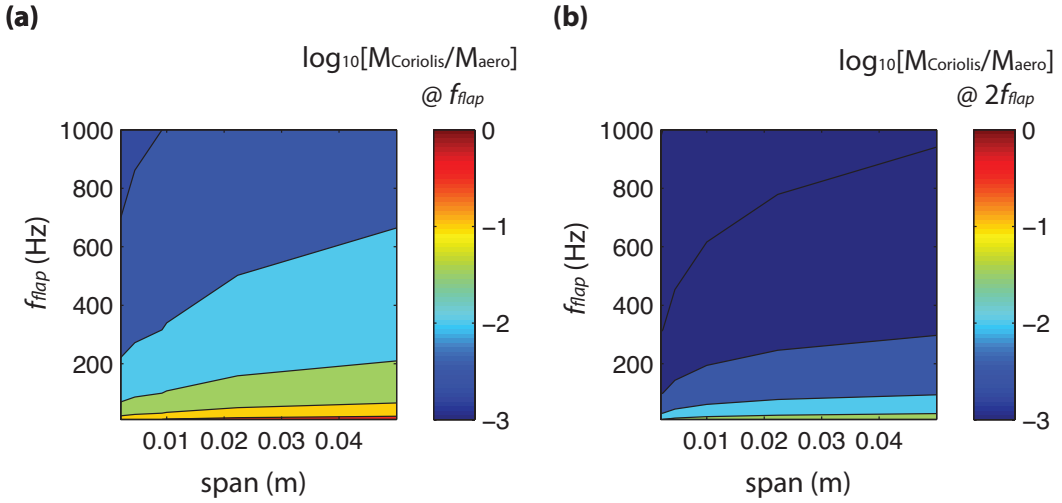

Figure 6.3. The ratio of the amplitudes of the Coriolis and aerodynamic moments for wings varies with wingspan and flapping frequency, f_{flap}. The log of the ratio is plotted over the surface at flapping frequency (a) and twice flapping frequency (b). The ratio is largest for moth-like wings (lower right corner of each surface).

Furthermore, when the frequency of flapping increases, the Coriolis to aerodynamic moment ratio decreases. Although both the Coriolis and aerodynamic moments increase with increasing flapping frequency, the aerodynamic moment is proportional to flapping frequency squared whereas the Coriolis force is proportional to the flapping frequency. Thus, the ratio is proportional to one over the flapping frequency.

6.3.2 *Coriolis to aerodynamic moments on wings increases with angular velocity*

Since the moment generated by the Coriolis force is directly proportional to angular velocity, it is not surprising that as angular velocity increases, so does the ratio of Coriolis to aerodynamic moments (figure 6.4).

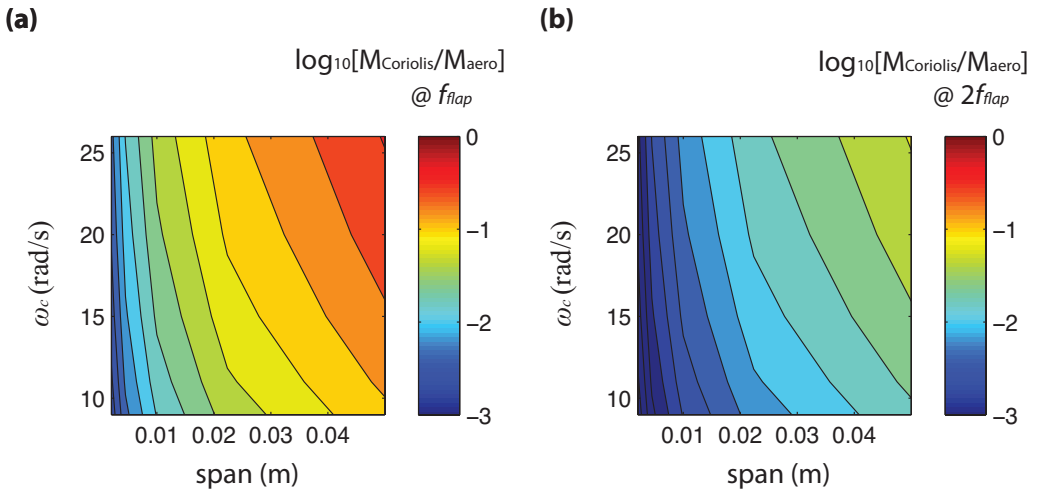

Figure 6.4. The ratio of the amplitudes of the Coriolis and aerodynamic moments for wings varies with wingspan and angular velocity, ω_c. The log of the ratio is plotted over the surface at flapping frequency (a) and twice flapping frequency (b). The ratio increases with increasing angular velocity and increasing wingspan.

6.3.3 *Ratio of Coriolis to aerodynamic moments on halteres is much larger than for wings*

Due to the streamlined form of a haltere, it is not surprising that the ratio or Coriolis to aerodynamic moments are much larger for a haltere than for a wing (figure 6.5). First, since the haltere has a large amount of mass out at its tip, the Coriolis forces induced on halteres are much larger than for a similarly scaled wing-like structure. In addition, the aerodynamic loading is lower on a haltere due to its streamlined form and this further amplifies the ratio of Coriolis to aerodynamic moments.

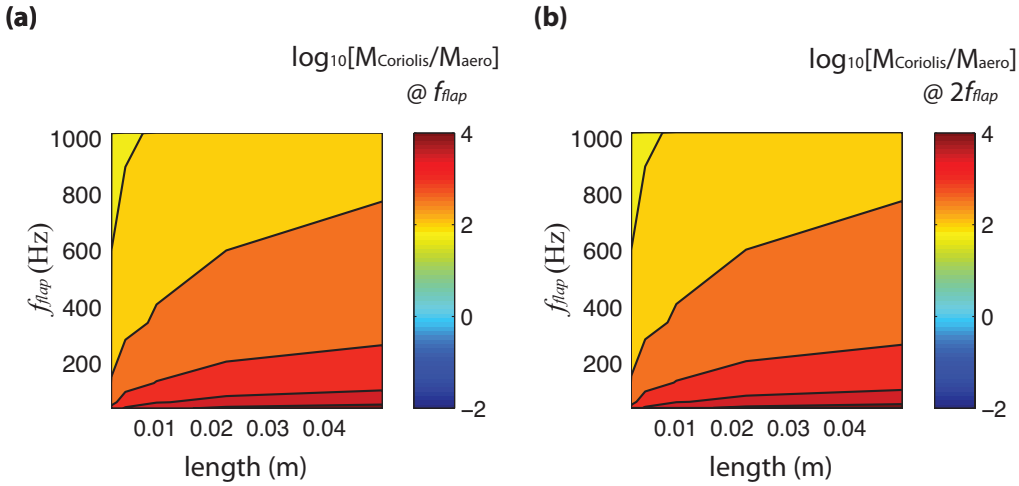

Figure 6.5. The ratio of the amplitudes of the Coriolis and aerodynamic moments for halteres varies with length and flapping frequency, f_{flap}. The log of the ratio is plotted over the surface at flapping frequency (a) and twice flapping frequency (b). The ratio is largest for moth-like wings (lower right corner of each surface).

6.4 CONCLUSIONS

We used rigid body dynamics combined with aerodynamic blade element methods to model inertial and aerodynamic forces on flapping wings and halteres during a constant orthogonal body rotation. By varying flapping frequencies, structure size, and body rotation rates according to experimentally measured values for a range of insect taxa, we explored the relative magnitude of gyroscopic to aerodynamic forces on wings and halteres. Our results show that the ratio of gyroscopic to aerodynamic forces decreases from 40% for model moth wings to 0.4% for model fly wings. We also found that the ratio for halteres is about 10-1000 times larger than for wings. These results point to a mechanism that can drive selection for angular rate detection in insect wings and explain their increased specialization for haltere geometries.

We recognize that the models developed here are very simple and do not account for all of the complex aerodynamic forces and elastic deformations that wings and halteres encounter in nature. However, these low-order models should be able to help us make some predictions about the basic principles that govern gyroscopic sensing in insect flight.

We found that for moth-like wings, the aerodynamic loads are close to the same order of magnitude as the Coriolis forces generated by body rotations. These results indicate that even with aerodynamic loads, it should be possible for moth-like wings to detect body rotations by

sensing the deformation of their wings. However, for fly-like wings the aerodynamic forces are much larger than the inertial forces and therefore flies might not be able to take advantage of the same sensory mechanisms as larger wings. This limitation might have led flies to develop haltere-like structures that are more sensitive to Coriolis forces, which would allow them to more readily detect body rotations. Indeed, we show that haltere-like structures do in fact experience Coriolis forces that are several orders of magnitude larger than the aerodynamic loads on the structure. The fact that the gyroscopic sensory capability of wings seems to vary with scale indicates a possible mechanical design pathway that could explain the evolution of halteres.

Chapter 7. CONCLUSIONS

The intent of this work was to develop a deeper understanding of the nature of fluid-structure interaction and gyroscopic sensing in insect wings. In pursuit of this goal, I completed four projects:

1) I developed a 2D model of fluid-structure interaction in a moth-like wing and showed that for most flapping frequencies and wing flexibilities relevant to insect flight the fluid forces have little impact on changing the shape of the wing and thereby impacting flight forces.

2) In order to investigate the gyroscopic sensing capabilities of insect wings, I created 3D structural dynamic computational model and constructed a robotically actuated bio-inspired wing model. This work described a novel mechanism, torsion, which would allow insect wings to serve as gyroscopic sensors.

3) After discovering that wings might employ torsional deformations to sense gyroscopic forces, I created a finite element model of a haltere to investigate if halteres might also develop torsional deformations when undergoing body rotations. The computational model indicates that halteres might indeed twist due to gyroscopic forces. Furthermore, the deformations that result from gyroscopic forces cause changes in the strain pattern on the haltere's surface.

4) Finally, to further explore how gyroscopic sensing capabilities of halteres and wings might differ, I used rigid body dynamics and blade element methods to explore how the aerodynamic and gyroscopic forces vary for halteres and wings of various sizes and flapping frequencies.

The work described in this dissertation serves to address several deficiencies in the literature. First, while several other researchers have developed models of fluid-structure interaction in insect wings, most employed either computational fluid dynamic models that were too computationally intensive to explore a vast parameter space or reduced-order models that had a limited ability to capture wing flexibility. In order to explore how aspects of wing flexibility and actuation might impact the development of flight forces, it was necessary to develop a new model that had reduced computation requirements and yet still achieve sufficient accuracy. The approach described in Chapter 3, using a vortex particle method coupled with a finite element model, was suitable for attaining such a goal. The results from this model indicated that although the flight forces vary with flapping frequency and flexural stiffness, the fluid forces have very

little impact on changing the shape of the wing and thereby impacting flight forces. Thus, for the parameter space of moth-sized wings with various flexural stiffness and flapping frequencies, our results confirmed prior work that the fluid and solid models could be run separately, which presents the possibility of significant computational savings.

Beyond serving as flight-force actuators, I showed that wings might also serve as gyroscopic sensors. While halteres are known to act as gyroscopic sensors for a small group of insects, most insects do not possess these mechanosensory structures and instead have an extra set of wings. Since halteres are derived from wings, evolution suggests that wings themselves might possess basic sensory capabilities that are similar to halteres. In Chapter 4 I described how wings might experience a torsional deformation when they are subject to body rotations. This result presented a possible mechanism by which the mechanosensors on the wing's surface might detect the body's angular velocity. Since the torsion developed by gyroscopic forces was different from the primary bending mode that occurs during wing flapping, it is possible that insects could isolate these very small deformations of their wings to obtain information about rotation rate.

After uncovering the torsional mechanism for gyroscopic sensing in wings, the next question became whether halteres, the gyroscopic sensors that are derived from wings, might also employ torsion to sense body rotations. Prior work in this field included kinematic analysis of the haltere, mathematical modeling of haltere bending, and a basic understanding of haltere's biological function. However, prior research on haltere dynamics assumed that halteres were comprised of a single point mass; no study had examined the importance of haltere mass distribution or torsion. In Chapter 5, I explained results from an analytical model that drew from prior work in the field but also included torsional deformation. I also explained the results from a finite element model of a haltere flapping with and without an imposed body rotation. Results from these models indicated that the gyroscopic sensing capabilities of the haltere vary with the haltere's mass distribution. Moreover, rotation of the flapping haltere does induce torsion. In addition, the haltere's dynamics are highly sensitive to its mass distribution, particularly to the distribution of mass in the bulb of the haltere. Finally, these bending and torsional deformations of the haltere cause changes in the spatiotemporal patterns of strain on the haltere's surface, which could be detected using the haltere's mechanosensors. The similarities between the gyroscopic sensory capabilities of halteres and wings also highlight a possible evolutionary pathway that might explain how insect halteres were derived from wings. By understanding this

mechanism, we might be able to create design criteria to improve small-scale angular velocity sensors for micro- and nano-air vehicles.

Finally, while it was useful to show that halteres and wings might sense angular velocity using the same sensory mechanism, we still did not completely understand how the aerodynamic forces on halteres and wings might impact the gyroscopic sensing capabilities of these structures. This topic is particularly relevant for formulating a coherent theory about the evolution of gyroscopic sensors in biology, especially since the relative scaling of aerodynamic and Coriolis forces changes when wing size decreases from a moth down to a fly. In Chapter 6, I explored some basic issues associated with how the ratio of Coriolis to aerodynamic forces scales with wing size and flapping frequency. Using rigid body dynamics and simple quasi-steady fluid models, I examined how size and frequency affect these forces on wings and halteres. I discovered that for moth-like wings, the gyroscopic and aerodynamic forces are of the same order of magnitude. However, for a fly-like wing, the aerodynamic forces are several orders of magnitude larger than the gyroscopic forces. Thus, while a moth-like wing might be able to sense gyroscopic forces it is unlikely that a fly-like wing would be able to function similarly. On the other hand, for a haltere, the ratio of Coriolis to aerodynamic forces is quite large for a structure of any size. This result indicates that there might be a scaling limitation for gyroscopic sensing in wings, which might allow a potential pathway for the evolution of a haltere-like form from a wing-like structure.

This work also presents several ideas that may be useful for engineering. First, as we continue to make smaller flying vehicles it may be useful to understand more about the design principles that govern wing flexibility in natural systems. For example, in many flexible-winged, nano-air vehicles, like the Harvard's RoboBee, Delft's DelFly, and Aerovironment's NanoHummingbird, wing flexibility was chosen without adhering to specific design criteria and was instead decided using a trial-and-error approach. In addition, these small, flexible-winged robots are often not able to achieve stable flight without being controlled by humans. However, some work has shown that if these robots know their angular velocity, stable control can be achieved autonomously (Fuller *et al* 2014a). As a result, understanding the nature of gyroscopic sensing in insect flight might provide useful insights for 1) generating design paradigms for flexible-winged systems and 2) controlling small-scale flexible-winged flyers using integrated angular velocity sensors. Furthermore, I believe there are numerous possibilities for the design of

bio-inspired sensor and control technologies for applications to renewable energy technologies, particularly for wind, wave, and tidal power. While issues of scale may pose challenges for applications in these areas, leveraging blade flexibility to create low-powered, bio-inspired sensors and actuators might improve the control of flexible, rotating power systems.

Beyond presenting ideas that might forward the development of engineered systems, this work clearly shows that engineering tools are extremely useful for exploring questions about biological systems. The synergetic relationship of using engineering to explore biology and biology to inspire engineering presents many interesting opportunities for future work.

REFERENCES

Alben S 2008 Optimal flexibility of a flapping appendage in an inviscid fluid *Journal of Fluid Mechanics* **614** 355-80

Alben S 2012 Flapping propulsion using a fin ray *Journal of Fluid Mechanics* **705** 149–64

Alben S, Witt C, Baker T V, Anderson E and Lauder G V 2012 Dynamics of freely swimming flexible foils *Physics of Fluids* **24** 051901

Bandyopadhyay P R, Beal D N and Menozzi A 2008 Biorobotic insights into how animals swim *Journal of Experimental Biology* **211** 206–14

Barannyk O, Buckham B J and Oshkai P 2012 On performance of an oscillating plate underwater propulsion system with variable chordwise flexibility at different depths of submergence *Journal of Fluids and Structures* **28** 152-66

Bathe K J and Wilson E L 1976 *Numerical Methods in Finite Element Analysis* (Englewood Cliffs, NJ: Prentice-Hall)

Bhadbhade V, Jalili N, and Nima Mahmoodi S 2008 A novel piezoelectrically actuated flexural/torsional vibrating beam gyroscope *Journal of Sound and Vibration* **311** 1305–1324

Bisplinghoff R L 1962 *Principles of Aeroelasticity* (New York: Wiley)

Bisplinghoff R L, Ashley H, and Halfman R L 1996 *Aeroelasticity* (New York: Dover)

Book W J 1979 Analysis of massless elastic chains with servocontrolled joints *ASME Journal of Dynamic Systems, Measurement, and Control* **101** 187–192

Brunton B, Eberle A L, Dickerson B, Brunton S, Kutz J N, and Daniel T 2014 Sensor placement for sparse sensory decision-making *COSYNE*, Salt Lake City, UT

Clark R P and Smits A J 2006 Thrust production and wake structure of a batoid-inspired oscillating fin *Journal of Fluid Mechanics* **562** 415–29

Chan W P, Prete F, and Dickinson M H 1998 Visual input to the efferent control system of a fly's 'gyroscope' *Science* **280** 289-292

Chapman K M, Mosinger J L, and Duckrow R B 1979 The role of distributed viscoelastic coupling in sensory adaptation in an insect mechanoreceptor *Journal of Comparative Physiology A* **131** 1–12

Chen J S, Chen J Y, and Chou Y F 2008 On the natural frequencies and mode shapes of dragonfly wings *Journal of Sound and Vibration* **313** 643–54

Chu S C and Pan K C 1975 Dynamic response of a high speed slider crank mechanism with an elastic connecting rod *ASME Journal of Engineering for Industry* **97** 542–550

Combes S A and Daniel T L 2003a Flexural stiffness in insect wings. II. Spatial distribution and dynamic wing bending *Journal of Experimental Biology* **206** 2989–97

Combes S A and Daniel T L 2003b Into thin air: Contributions of aerodynamic and inertial-elastic forces to wing bending in the hawkmoth *Manduca sexta*. *Journal of Experimental Biology* **206** 2999–3006

Combes S A and Daniel T L 2003c Flexural stiffness in insect wings I. Scaling and the influence of wing venation *Journal of Experimental Biology* **206** 2979–87

Daniel T L and Combes S A 2002 Flexible wings and fins: Bending by inertial or fluid-dynamic forces? *Integrative and Comparative Biology* **42** 1044-1049

Daniel T L, Aldworth Z, Hinterwirth A and Fox J 2012 Insect inertial measurement units: gyroscopic sensing of body rotation *Frontiers in Sensing: from Biology to Engineering* ed. F G Barth, J A C Humphrey and M V Srinivasan (Wien, Austria: Springer) pp 287–97

Derham W 1713 *Physico-theology: or, a demonstration of the being and attributes of God.* (At the honorable Mr. Boyle's lectures 1711 and 1712) W Innys, London

Dewey P A, Boschitsch B M, Moored K W, Stone H A and Smits A J 2013 Scaling laws for the thrust production of flexible pitching panels *Journal of Fluid Mechanics* **732** 29–46

Dickerson B H, Aldworth Z N, and Daniel T L 2014 Control of moth flight posture is mediated by wing mechanosensory feedback *Journal of Experimental Biology* **217** 2301-2308

Dickinson M H 1990a Linear and nonlinear encoding properties of an identified mechanoreceptor on the fly wing measured with mechanical noise stimuli *Journal of Experimental Biology* **151** 219–44

Dickinson M H 1990b Comparison of encoding properties of campaniform sensilla on the fly wing *Journal of Experimental Biology* **151** 245–61

Dickinson M H and Gotz K G 1993 Unsteady aerodynamic performance of model wings at low Reynolds numbers *Journal of Experimental Biology* **174** 45–64

Dickinson M H 1999 Haltere-mediated equilibrium reflexes of the fruit fly, *Drosophila melanogaster Philosophical Transactions of the Royal Society B* **354** 903–16.

Dickinson M H, Lehmann F-O and Sane S P 1999 Wing rotation and the aerodynamic basis of insect flight *Science* **284** 1954–60

Eberle A L, Reinhall P G, and Daniel T L 2014 Fluid-structure interaction in compliant insect wings *Bioinspiration and Biomimetics* **9** 025005

Eberle A L, Dickerson B H, Reinhall P G, and Daniel T L 2015 A new twist on gyroscopic sensing: body rotations lead to torsion in flapping, flexing insect wings *Journal of the Royal Society, Interface* **12** 20141088

Eldredge J D, Toomey J and Medina A 2010 On the roles of chord-wise flexibility in a flapping wing with hovering kinematics *Journal of Fluid Mechanics* **659** 94-115

Ellington C P, van den Berg C, Willmott A P and Thomas A L R 1996 Leading-edge vortices in insect flight *Nature* **384** 626–30

Ellington C P 1999 The novel aerodynamics of insect flight: applications to micro-air vehicles *Journal of Experimental Biology* **202** 3439–48

Ennos A 1988 The importance of torsion in the design of insect wings *Journal of Experimental Biology* **140** 137–60

Fitzgerald T, Valdez M, Vanella M, Balaras E and Balachandran B 2011 Flexible flapping systems: computational investigations fluid-structure interactions *Aeronautical Journal* **115** 593-604

Fox J L and Daniel T L 2008 A neural basis for gyroscopic force measurement in the halteres of *Holorusia Journal of Comparative Physiology A* **194** 887-897

Fox J L, Fairhall A L, and Daniel T L 2010 Encoding properties of haltere neurons enable motion feature detection in a biological gyroscope **107** 3840–5

Fraenkel G and Pringle J W S 1938 Biological sciences: halteres of flies as gyroscopic organs of equilibrium *Nature* **141** 919-920

Friedmann P P 2004 Rotary-wing aeroelasticity: Current status and future trends *AIAA Journal* 1953-1972

Fry S N, Sayaman R and Dickinson M H 2003 The aerodynamics of free-flight maneuvers in Drosophila *Science* **300** 495-498

Fuller S B, Karpelson M, Censi A, Ma K, and Wood R J 2014a Controlling free flight of a robotic fly using an onboard vision sensor inspired by insect ocelli *Journal of the Royal Society Interface* **11** 97

Fuller S B, Straw A D, Peek M Y, Murray R M, & Dickinson M H 2014b Flying Drosophila stabilize their vision-based velocity controller by sensing wind with their antennae. *Proceedings of the National Academy of Sciences of the United States of America.* **111** 1182-91

Funk K, Emmerich H, Schilp A, Offenberg M, Neul R, and Larmer F 1999 A surface micromachined silicon gyroscope using a thick polysilicon layer In *12th Annual IEEE International Conference on Micro Electro Mechanical Systems*, 57–60, 17–21 Jan, Orlando, FL

Greenewalt C H 1962 *Dimensional Relationships for Flying Animals* (Washington DC: Smithsonian Institution)

Heathcote S and Gursul I 2007 Flexible flapping airfoil propulsion at low Reynolds numbers *Aiaa Journal* **45** 1066-1079

Hedrick T L and Daniel T L 2006 Flight control in the hawkmoth *Manduca sexta*: the inverse problem of hovering *Journal of Experimental Biology* **209** 3114-3130

Hedrick T L, Cheng B, and Deng X 2009 Wingbeat Time and the Scaling of Passive Rotational Damping in Flapping Flight *Science* **324** 252-255

Hengstenberg R 1988 Mechanosensory control of compensatory head roll during flight in the blowfly *Calliphora erythrocephala Journal of Comparative Physiology A* **163** 151–65.

Hinterwirth A J and Daniel T L 2010 Antennae in the hawkmoth *Manduca sexta* (Lepidoptera, Sphingidae) mediate abdominal flexion in response to mechanical stimuli *Journal of Comparative Physiology A* **196** 947–56

Hinterwirth A J, Medina B, Lockey J, Otten D, Voldman J, Lang J H, Hildebrand J G, and Daniel T L 2012 Wireless stimulation of antennal muscles in freely flying hawkmoths leads to flight path changes *PLoS ONE* **7** e52725

Ho J Y L 1977 Direct path method for flexible multibody spacecraft dynamics *Journal of Spacecraft and Rockets* **14** 102–110

Jankauski M and Shen I Y 2014 Dynamic modeling of a rotating insect wing In *Proceeding of the International Micro Air Vehicle Conference* Delft, The Netherlands

Kang C K, Aono H, Cesnik C E S and Shyy W 2011 Effects of flexibility on the aerodynamic performance of flapping wings *Journal of Fluid Mechanics* **689** 32-74

Katz J and Plotkin A 2001 *Low-Speed Aerodynamics* (Cambridge, UK: Cambridge University Press)

Land MF and Collett TS 1974 Chasing behaviour of houseflies (Fannia c.). *Journal Comparative Physiology* **89** 331-357

Lauder G V and Madden P G A 2007 Fish locomotion: kinematics and hydrodynamics of flexible foil-like fins *Experiments in Fluids* **43** 641-653

Lee K B, Kim J H and Kim C 2011 Aerodynamic Effects of Structural Flexibility in Two-Dimensional Insect Flapping Flight *Journal of Aircraft* **48** 894-909

Leftwich M C, Tytell E D, Cohen A H and Smits A J 2012 Wake structures behind a swimming robotic lamprey with a passively flexible tail *Journal of Experimental Biology* **215** 416-425

Lentink D, Muijres F T, Donker-Duyvis F J and van Leeuwen J L 2008 Vortex-wake interactions of a flapping foil that models animal swimming and flight *Journal of Experimental Biology* **211** 267–73

Lentink D and Dickinson M H 2009 Rotational accelerations stabilize leading edge vortices on revolving fly wings *Journal of Experimental Biology* **212** 2705–19

Lentink D, Dickson W B, van Leeuwen J L and Dickinson M H 2009 Leading-edge vortices elevate lift of autorotating plant seeds *Science* **324** 1438–40

Lighthill M J 1975 *Mathematical biofluiddynamics* (Philadelphia: Society for Industrial and Applied Mathematics)

Liu H, Ellington C P, Kawachi K, van den Berg C and Willmott A P 1998 A computational fluid dynamic study of hawkmoth hovering *Journal of Experimental Biology* **201** 461-477

Lua K B, Lai K C, Lim T T and Yeo K S 2010 On the aerodynamic characteristics of hovering rigid and flexible hawkmoth-like wings *Experiments in Fluids* **49** 1263-1291

Ma K Y, Chirarattananon P, Fuller S B and Wood R J 2013 Controlled flight of a biologically inspired, insect-scale robot *Science* **340** 603–7

Meirovitch L 1974 A new method of solution of the eigenvalue problem for gyroscopic systems *AIAA Journal* **12** 1337–1342

Meirovitch L 1975 A modal analysis for the response of linear gyroscopic systems A*SME Journal of Applied Mechanics* **42** 446–450

Melosh R J 1963 Basis of Derivation of matrices for the direct stiffness method *AIAA Journal* **1** 1631-1637

Michelin S and Smith S G L 2009 Resonance and propulsion performance of a heaving flexible wing *Physics of Fluids* **21**

Moored K W, Dewey P A, Smits A J and Haj-Hariri H 2012 Hydrodynamic wake resonance as an underlying principle of efficient unsteady propulsion *Journal of Fluid Mechanics* **708** 329-348

Mountcastle A M and Daniel T L 2009 Aerodynamic and functional consequences of wing compliance *Experiments in Fluids* **46** 873-882

Mountcastle A M and Daniel T L 2010 Vortexlet models of flapping flexible wings show tuning for force production and control *Bioinspiration & Biomimetics* **5**

Nakata T, Liu H, Tanaka Y, Nishihashi N, Wang X and Sato A 2011 Aerodynamics of a bio-inspired flexible flapping-wing micro air vehicle *Bioinspiration and Biomimetics* **6** 045002

Nakata T and Liu H 2012 Aerodynamic performance of a hovering hawkmoth with flexible wings: a computational approach *Proceedings of the Royal Society B-Biological Sciences* **279** 722-731

Nalbach G 1993 The halteres of the blowfly *Calliphora* I. Kinematics and dynamics. *Journal of Comparative Physiology A* **173** 293–300

Nalbach G and Hengstenberg R 1994 The halteres of the blowfly *Calliphora* II. Three-dimensional organization of compensatory reactions to real and simulated rotations *Journal of Comparative Physiology A* **175** 695–708.

Norris A G, Palazotto A N, and Cobb R G 2010 Structural dynamic characterization of an insect wing *51st AIAA/ASME/ASCE/AHS/ASC Structures, Structural Dynamics, and Materials Conference*, 12–15 April 2010, Orlando, FL

Pix W, Nalbach G, and Zeil J 1993 Strepsipteran forewings are haltere-like organs of equilibrium *Naturwissenschaften* **80** 371–4.

Pringle J W S 1948 The gyroscopic mechanism of the halteres of Diptera. *Philosophical Transactions of the Royal Society of London, B* **233** 347–38

Ramamurti R and Sandberg W C 2001 Computational Study of 3-D Flapping Foil Flows *39th AIAA Aerospace Sciences Meeting & Exhibit* Reno, NV

Ramananarivo S, Godoy-Diana R and Thiria B 2011 Rather than resonance, flapping wing flyers may play on aerodynamics to improve performance *Proceedings of the National Academy of Sciences of the United States of America* **108** 5964-9

Rayleigh L 1877 *The Theory of Sound*, *Volume 1* (New York, NY: The Macmillan Company)

Reddy J N 2004 *An Introduction to the Finite Element Method,* Third Ed. (New York, NY: McGraw Hill)

Reissner E, Stein M 1951 Torsion and transverse bending of cantilever plates *NACA Technical Note* 2369

Sandeman D C and Markl H 1980 Head movements in flies (Calliphora) produced by deflexion of the halteres. Journal of Experimental Biology **85** 43–60

Sane S P 2003 The aerodynamics of insect flight *Journal of Experimental Biology* **206** 4191–4208

Sane S P, Dieudonne A, Willis M A, and Daniel T L 2007 Antennal mechanosensors mediate flight control in moths *Science* **315** 863–866

Shabana A A 1997 Flexible Multibody Dynamics: Review of Past and Recent Developments *Multibody System Dynamics* **1** 189-222

Shabana A A 2013 *Dynamics of Multibody Systems* (New York, NY: Wiley)

Shukla R K and Eldredge J D 2007 An inviscid model for vortex shedding from a deforming body *Theor. Comput. Fluid Dyn.* **21** 343–368

Shyy W, Aono H, Chimakurthi S K, Trizila P, Kang C K, Cesnik C E S and Liu H 2010 Recent progress in flapping wing aerodynamics and aeroelasticity *Progress in Aerospace Sciences* **46** 284–327

Song J O and Haug E J Dynamic analysis of planar flexible mechanisms *Computer Methods in Applied Mechanics and Engineering* **24** 359–381

Sreenivasamurthy S and Ramamurti V 1981 Coriolis effect on the vibration of flat rotating low aspect ratio cantilever plates *Journal of Strain Analysis and Engineering Design* **16** 97–106

Stanford B K, Sallstrom E, Ukeiley L and Ifju P G 2011 Structural dynamics and aerodynamics measurements of biologically inspired flexible flapping wings *Bioinspiration and Biomimetics* **6** 016009

Sun M and Tang J 2002 Unsteady aerodynamic force generation by a model fruit fly wing in flapping motion *Journal of Experimental Biology* **205** 55-70

Taylor G K and Krapp H G 2007 Sensory systems and flight stability: what do insects measure and why? *Advances in Insect Physiology* **34** 231-316

Theobald J C, Warrant E J, and O'Carroll D C 2010 Wide-field motion tuning in nocturnal hawkmoths *Proceedings of the Biological Sciences* **277** 853–60

Thompson R, Wehling M, Evers J, and Dixon W 2008 Body rate decoupling using haltere mid-stroke measurements for inertial flight stabilization in Diptera *Journal of Comparative Physiology A* **195** 99–112

Timoshenko S, Young D H and Weaver W 1974 *Vibration Problems in Engineering* (New York: Wiley)

Toomey J and Eldredge J D 2008 Numerical and experimental study of the fluid dynamics of a flapping wing with low order flexibility *Physics of Fluids* **20** 073603

Usherwood J R and Ellington C P 2002 The aerodynamics of revolving wings I. Model hawkmoth wings *Journal of Experimental Biology* **205** 1547–1564

Vanella M, Fitzgerald T, Preidikman S, Balaras E and Balachandran B 2009 Influence of flexibility on the aerodynamic performance of a hovering wing *Journal of Experimental Biology* **212** 95–105

Veers P, Lobitz D, and Bir G 1998 *Aeroelastic tailoring in wind-turbine blade applications* (Albuquerque, NM: Sandia National Labs)

Volterra E and Zachmanoglou E C 1965 *Dynamics of Vibrations* (Columbus: Merrill Books)

Voss R, Bauer K, Ficker W, Gleissner T, Kupke W, Rose M, Sassen S, Schalk J, Seidel H, and Stenzel E 1997 Silicon angular rate sensor for automotive applications with piezoelectric drive and piezoresistive read-out, In *IEEE International Conference on Solid-state Sensors and Actuators,* 879–82, 16-19 June, Chicago, IL

Walker S M, Thomas A L R, and Taylor G K 2009 Deformable wing kinematics in the desert locust: how and why do camber, twist and topography vary through the stroke? *Journal of the Royal Society, Interface* **6** 735–47

Weis-Fogh T 1973 Quick estimates of flight fitness in hovering animals including novel mechanisms for lift production *Journal of Experimental Biology* **59** 169-230

White F M 1974 *Viscous fluid flow* (New York: McGraw-Hill)

Wootton R J 1992 Functional-morphology of insect wings *Annual Review of Entomology* **37** 113–40

Wootton R J 1993 Leading edge section and asymmetric twisting in the wings of flying butterflies (Insecta, Papilionoidea) *Journal of Experimental Biology* **180** 105–17

Wu T 1971 Hydrodynamics of swimming propulsion: part 1. Swimming of a two-dimensional flexible plate at variable forward speeds in an inviscid fluid *Journal of Fluid Mechanics* **46** 337–55

Wu W C, Wood R J, and Fearing R S 2002 Halteres for the micromechanical flying insect *IEEE* 60–65

Yin B and Luo H X 2010 Effect of wing inertia on hovering performance of flexible flapping wings *Physics of Fluids* **22**

Young J, Walker S M, Bomphrey R J, Taylor G K and Thomas A L R 2009 Details of Insect Wing Design and Deformation Enhance Aerodynamic Function and Flight Efficiency *Science* **325** 1549-1552

Zhang J, Liu N S and Lu X Y 2010 Locomotion of a passively flapping flat plate *Journal of Fluid Mechanics* **659** 43-68

Zhao L, Huang Q F, Deng X Y and Sane S P 2010 Aerodynamic effects of flexibility in flapping wings *Journal of the Royal Society Interface* **7** 485-497

Zhu Q 2007 Numerical simulation of a flapping foil with chordwise or spanwise flexibility *AIAA Journal* **45** 2448-2457

Zill S N and Moran D T 1981 The exoskeleton and insect proprioception. I. Responses of tibial campaniform sensilla to external and muscle-generated forces in the American cockroach *Journal of Experimental Biology* **91** 1–24

APPENDIX 1:
SUPPLEMENTARY MATERIAL FOR FLUID-STRUCTURE INTERACTION MODEL

This appendix contains the supplementary material for Chapter 3: Fluid-Structure Interaction in Insect Wings. In that chapter, we described a computationally efficient 2D model of an insect with and without fluid-structure interaction (see figure S1 for a program diagram of the coupled model that includes fluid-structure interaction). As shown, we input the properties of the model (*e.g.* flexural stiffness, actuation frequency, fluid density, solid density, *etc*.) at startup along with the initial conditions and boundary conditions. We used these values to run the solid model for a small time step forward and to generate a solution for the deformation of the wing in response in input motions at the base. We then fed these results of the deformed solution from the solid model into the fluid model to compute the pressure of that the fluid exerted onto the solid after another small time step. We compared the values for the deformation of the solid and the pressure of the fluid to the previous step to ensure the values were not diverging. Assuming that the solution converged, we changed the boundary conditions and initial conditions for the next time step according to the results from the previous time step and then repeated the process until we reached the desired final time. If the solution did not converge, we tried ten smaller time steps in an attempt to achieve convergence and if none of those iterations succeeded we aborted the model. For all of the cases we reported in the text, the model converged (the convergence check was primarily used for troubleshooting).

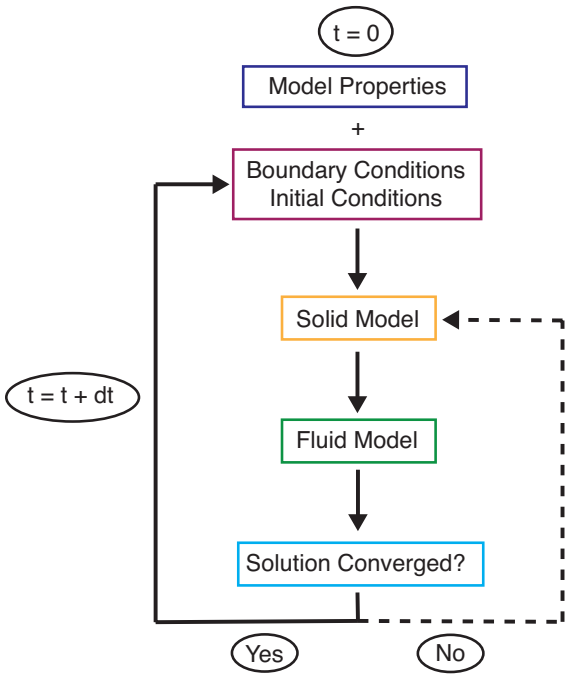

Figure S1. Program diagram for coupled fluid-solid model.

Experimental Determination of Damping

Insect wings experience internal friction forces due to imperfect elasticity of the wing. As a result, if a severed insect wing initially at rest is perturbed in a fixed-free setup in a vacuum, the vibrations of the wing will decay fairly quickly. Thus, the inherent damping of the wing must be incorporated when a physical model of the wing is developed.

We are not aware of any work that provides detailed information about the damping coefficients in insect wings. As a result, we performed an experiment to estimate the damping ratio of *Manduca sexta* wings in air. While our experiment did not isolate the importance of internal damping, it still provided us with an approximate value to use in our model.

We evaluated the damping ratio of an excised wing of the hawkmoth *Manduca sexta* using the free-vibration decay method. Using this approach, we approximated the wing as a simple spring-mass-damper and evaluated the viscous damping in the system. The general solution for the displacement, *x(t)*, of the mass in such a setup is

$$x(t) = Ae^{-\delta t}\cos(\omega_d t - \alpha_d) \qquad \text{(A1.1)}$$

where A is the amplitude of the displacement in meters, δ is the logarithmic decrement, ω_d is the damped natural frequency of the displacement in rad/s, and α_d is the damped phase angle in rad (Timoshenko *et al* 1974). This motion is comprised of periodic motion that decays within an exponential decay envelope. The decrement in amplitude over time corresponds to the logarithmic decrement, d. The ratio of two amplitudes j cycles apart can be used to evaluate d using

$$d = \frac{1}{j}\ln\left(\frac{x_i}{x_{i+j}}\right) \tag{A1.2}$$

where x_i and x_{i+j} are two amplitudes j cycles apart (Timoshenko *et al* 1974). The damping ratio, ζ, is given in terms of the logarithmic decrement by

$$\zeta = \frac{1}{\sqrt{1+\left(2\pi/d\right)^2}} \tag{A1.3}$$

which allows us to evaluate the amount of damping in a system by examining the decay of the position of the system over time.

Using this method, we determined the chord-wise damping of the first mode of vibration of an excised *Manduca sexta* wing. We fixed the leading edge of an excised wing onto a microscope slide using superglue. We then placed the microscope slide in a vice grip and adhered retro-reflective tape onto the ventral side of the wing at a location of about 75% of the chord in a direction toward the trailing edge (see figure S2(a)). We setup a laser vibrometer at a distance of approximately 0.5 m along a line perpendicular to the width of the wing such that the laser landed upon the retro-reflective tape on the wing (see figure S2(b)). We perturbed the wing tip with a quick flick from a cotton swab and recorded the wing velocity following the perturbation (figure S3).

We repeated this experiment for five wings from five different animals and performed five trials for each wing. Before running each trial, we made sure to allow enough time to ensure the motion from the prior trial had subsided. We made use of equations (A1.2) and (A1.3) along with the time-series recordings of the velocity (*e.g.* figure S3) to compute the damping ratio for each trial. The average of all trials revealed $\zeta=0.15$ with a standard error of 0.04 (n = 5). Since we actuated the wing using an impulse force, we assumed that the first mode dominated the

response. Thus, the damping ratio revealed here should correspond to the first mode of vibration. However, since we did not perform the experiment in a vacuum, this damping ratio overestimates the internal damping because it takes into account both the internal damping of the wing and the external damping of the air surrounding the wing.

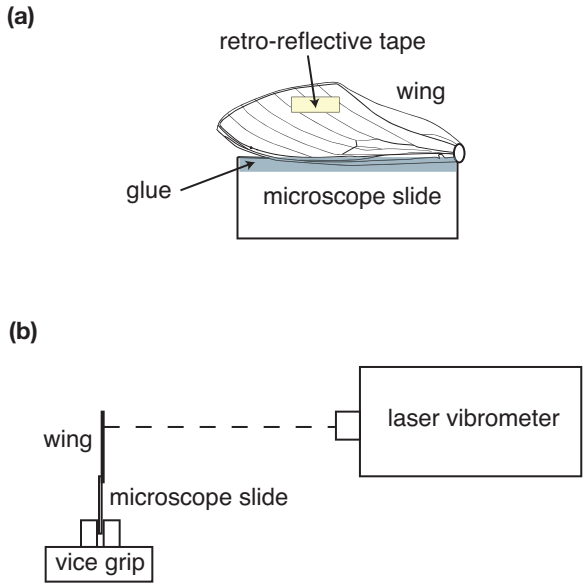

Figure S2. Experimental setup used to determine wing damping as viewed from two directions: (a) perpendicular to the laser vibrometer and (b) parallel to the laser vibrometer.

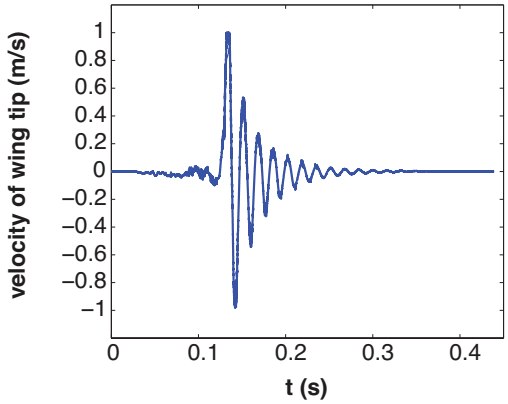

Figure S3. Time-series plot of the velocity of an excised *Manduca sexta* wing tip in response to a slight perturbation at the wing tip (recorded using a laser vibrometer).

FLUID MODEL VALIDATION

We used two approaches to validate our fluid model: 1) comparison of lift force generated by rigid inclined plate to theoretical expectation and 2) comparison between small amplitude heaving and pitching rigid plate and Theodorsen's model. We also performed an analysis to examine the impact of the smoothing parameter, δ, which ensures that a singularity does not occur in the computation of the velocity field.

Inclined plate

For small angles of attack, the lift generated by a rigid plate in uniform flow should equal $2\pi \sin(\alpha)$. As expected, our model generates the correct values for the steady state value of the coefficient of lift at several angles of attack (figure S4).

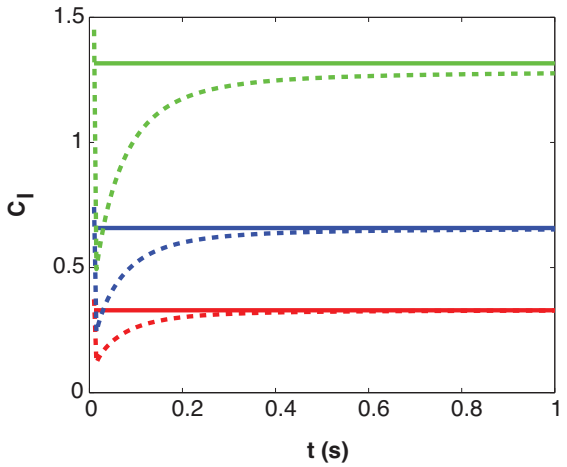

Figure S4. Coefficient of lift of rigid inclined plate generated by model (dashed) versus theoretical value (solid) for several angles of attack (red: 3 degrees; blue: 6 degrees; green: 12 degrees).

Heaving and pitching plate

The lift generated by a plate undergoing small amplitude heaving and pitching motions is well described by Theodorsen's model. This model states that the lift, L, generated by a plate that is pitching, α, and heaving, h, about the leading edge is given by (Bisplinghoff 1962)

$$L = \pi\rho b^2\left[\ddot{h} + U_{ref}\dot{\alpha} + b\ddot{\alpha}\right] + 2\pi\rho U_{ref} b\ C(k)\left[\dot{h} + U_{ref}\alpha + \tfrac{3}{2}b\dot{\alpha}\right] \tag{A1.4}$$

where ρ is the density of the fluid, b is the half-chord length, U_{ref} is the free-stream velocity, and $C(k)$ is Theodorsen's function. Theodorsen's function can be written in terms of Hankel functions, $H_v^{(2)}(k)$, as

$$C(k) = \frac{H_1^{(2)}(k)}{H_1^{(2)}(k) + iH_0^{(2)}(k)} \tag{A1.5}$$

$$H_v^{(2)}(k) = J_v(k) - iY_v(k) \tag{A1.6}$$

where J_v and Y_v are Bessel functions of the first and second kind, and k is the reduced frequency given by $k = 2\pi fb/U_{ref}$. In our model we set the value of the half-chord length, b, and free-stream velocity, U_{ref}, to be 0.01 m and 1.2 m/s, respectively. We varied the frequency, f, of the maneuver from 10 to 100 Hz. As a result of this variation, we examined the performance of our model using a rigid plate and compared it to Theodorsen's model for small amplitude heaving and pitching motions at three different frequencies: f = 2 Hz, f = 25 Hz, and f = 100 Hz (figure S5).

The tip displacement in all cases remained the same, which makes sense for the case of a rigid plate (see first column of figure S5). However, the values of lift vary depending on frequency (see second through fourth columns in figure S5). As expected, the magnitudes of the unsteady lift increases dramatically as we shift the maneuver from low to high frequencies. Even at high frequencies, the value of lift generated by the model (dashed) is very close to the theoretical prediction via Theodorsen's model (solid).

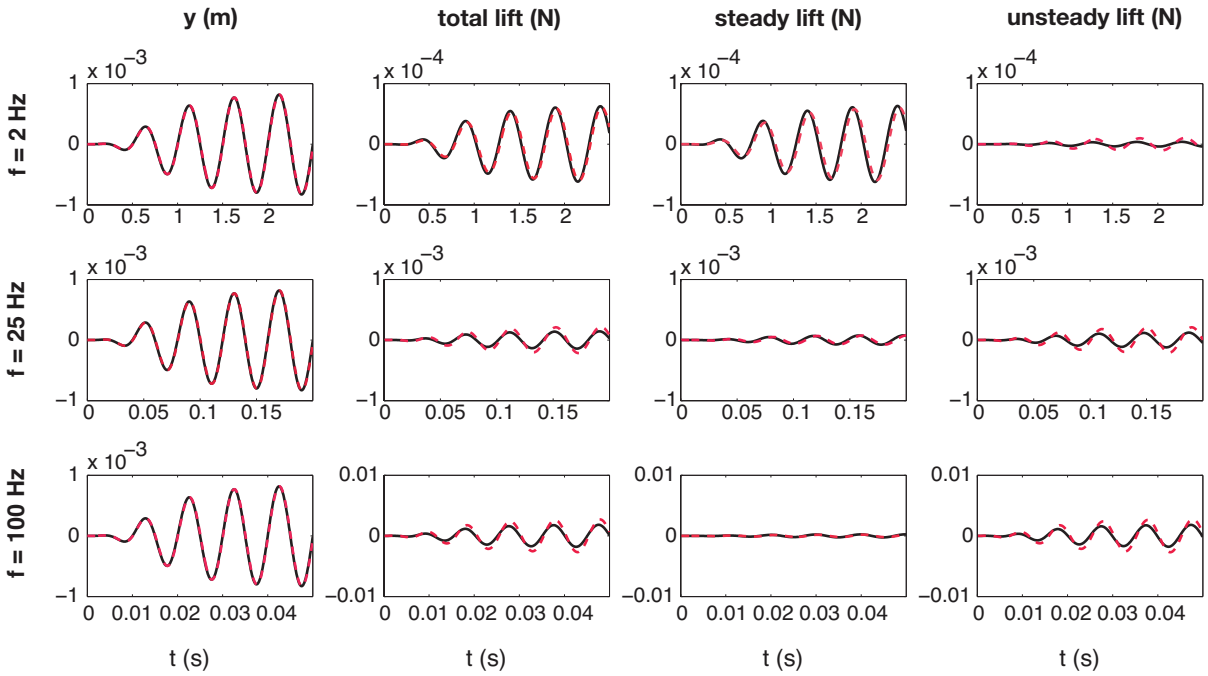

Figure S5. Comparison between lift computed by the fluid model alone (*i.e.* rigid model - dashed red) and lift from Theodorsen's model (solid black) for a plate being pitched and heaved under small amplitudes about the leading edge at three frequencies of oscillation: f = 2 Hz (first row), f = 25 Hz (second row), and f = 100 Hz (third row). The first column depicts the amount of tip displacement that the plate undergoes in each case. Columns two through four represent the total lift, steady lift, and unsteady lift for all three frequencies.

Sensitivity to smoothing parameter, δ

We also examined the extent to which the smoothing parameter in the velocity field computation, δ, changed our computations of the coefficient of lift and the lift ratio. Figure S6 shows that for a range of flexural stiffnesses and actuation frequencies, the value of the coupled coefficient of lift and the lift ratio do not change by more than 5% from those that we reported.

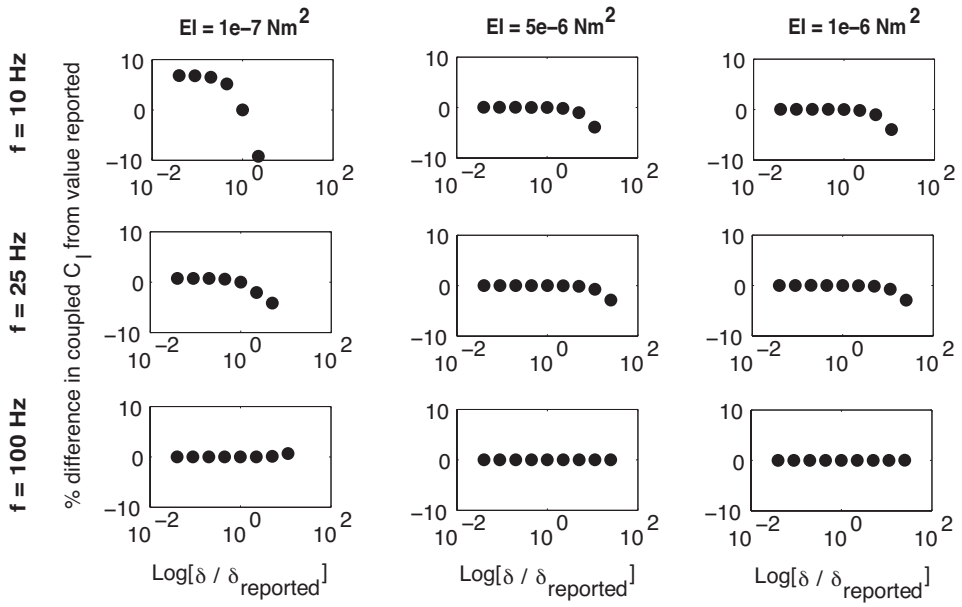

Figure S6. Differences in the coupled coefficient of lift, C_l, as the velocity field smoothing parameter, δ, varies for three frequencies of oscillation: f = 10 Hz, f = 25 Hz, and f = 100 Hz (rows 1-3, respectively) and three different flexural stiffnesses (EI): 1e-7 Nm^2, 5e-6 Nm^2, and 1e-6 Nm^2 (columns 1-3, respectively). The x-axis of each plot is the ratio of the δ value versus δ reported (*i.e.* a ratio of 10 means δ is ten times the value reported in the text, which is computed using equations (4.5) and (4.6) and varies with frequency and flexural stiffness). For example, when f = 10 Hz and EI = 1e-7 Nm^2, the value of $\delta_{reported}$ equals 0.0024 m. The y-axis of each plot is the percent difference between the coefficients of lift computed for the given δ as compared to the value reported in the text of the article.

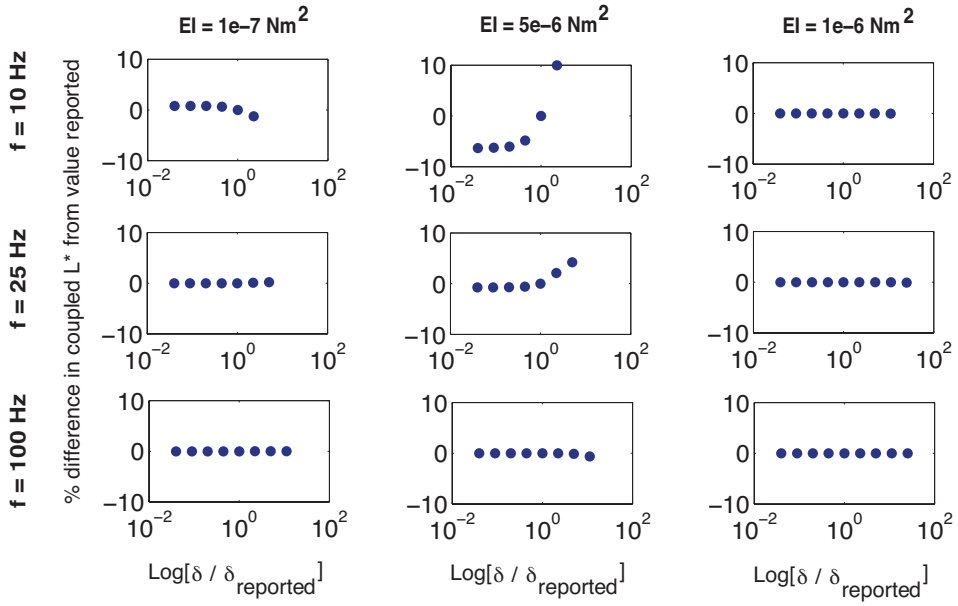

Figure S7. Differences in the lift ratio, L^*, as the velocity field smoothing parameter, δ, varies for three frequencies of oscillation: f = 10 Hz (first column), f = 25 Hz (second column), and f = 100 Hz (third column) and three different flexural stiffnesses (EI): 1e-7 Nm^2, 5e-6 Nm^2, and 1e-6 Nm^2 (rows one to three, respectively). The x- and y- axes are reported in the same manner as in figure S6 (y-axis is now in terms of L^* rather than C_l).

SOLID MODEL VALIDATION

To validate our solid model, we compared the results from our finite element model (FEM) to the analytical results of the fourth order beam equation subject to support motions. The beam equation for uniform flexural stiffness, EI, is given by

$$\frac{\partial^4 y}{\partial x^4} + \frac{\rho A}{EI}\frac{\partial^2 y}{\partial t^2} = p(x,t) \qquad \text{(A1.7)}$$

where ρ is the density of the solid, A is the cross sectional area, x is the position along the length of the beam, y is the transverse position of the beam, t is time, and $p(x,t)$ is the loading applied to the beam and varies over space and time.

Assuming no load is applied and that the boundary conditions correspond to those of a cantilever (fixed-free) with heaving support motion, $g(t)$, at the fixed end, equation A1.6 can be solved using displacement influence functions (Timoshenko *et al* 1974) to give

$$y(x,t) = g(t) - \sum_{i=1}^{\infty} \frac{X_i}{p_i} \int_0^L X_i \, dx \int_0^t \frac{\partial^2 g(t')}{\partial t^2} \sin(p_i(t-t')) \, dt' \tag{A1.8}$$

$$p_i = \left(\frac{k_i}{L}\right)^2 \sqrt{\frac{EI}{\rho A}} \tag{A1.9}$$

$$g(t) = a\sin(\omega t) \tag{A1.10}$$

$$X_i = \frac{1}{\sqrt{\alpha_i}} \left[\cosh(k_i x) - \cos(k_i x) - A_i \left\{ \sinh(k_i x) - \sin(k_i x) \right\} \right] \tag{A1.11}$$

$$\alpha_i = \int_0^L X_i^2 \, dx \tag{A1.12}$$

$$A_i = \frac{\cos(k_i) + \cosh(k_i)}{\sin(k_i) + \sinh(k_i)} \tag{A1.13}$$

where a and ω are the amplitude and angular frequency of the heaving motion of the base, L is the length of the beam, and k_i are the roots of the frequency equation that governs a fixed-free beam: $\cos(k_i)\cosh(k_i) = -1$. For our comparison, we used the first five terms of the series (i = 1 to 5) because we found that the motion of the wing was well described by the first five modes. The first five modes were likely sufficient because we ran our model until it reached steady state and we did not apply our forcing near the higher modes of vibration.

We compared the analytical and FEM results for nine different cases: three frequencies (15 Hz, 40 Hz, and 130 Hz) for each of three flexural stiffnesses (1e-5 Nm^2, 1e-6 Nm^2, and 1e-7 Nm^2). We examined the steady-state results for the case of a damping ratio of 0.15, which we determined to be the damping ratio of *Manduca sexta* wings (figure S3). As shown in figure S8, the analytical results and the experimental results are very similar over this range of stiffnesses and frequencies. We also examined how the model behaves when it is run with no damping near the structural resonance of the beam (figure S9). As expected, the tip displacement exhibits beating when the model is run near the resonant frequency of the beam.

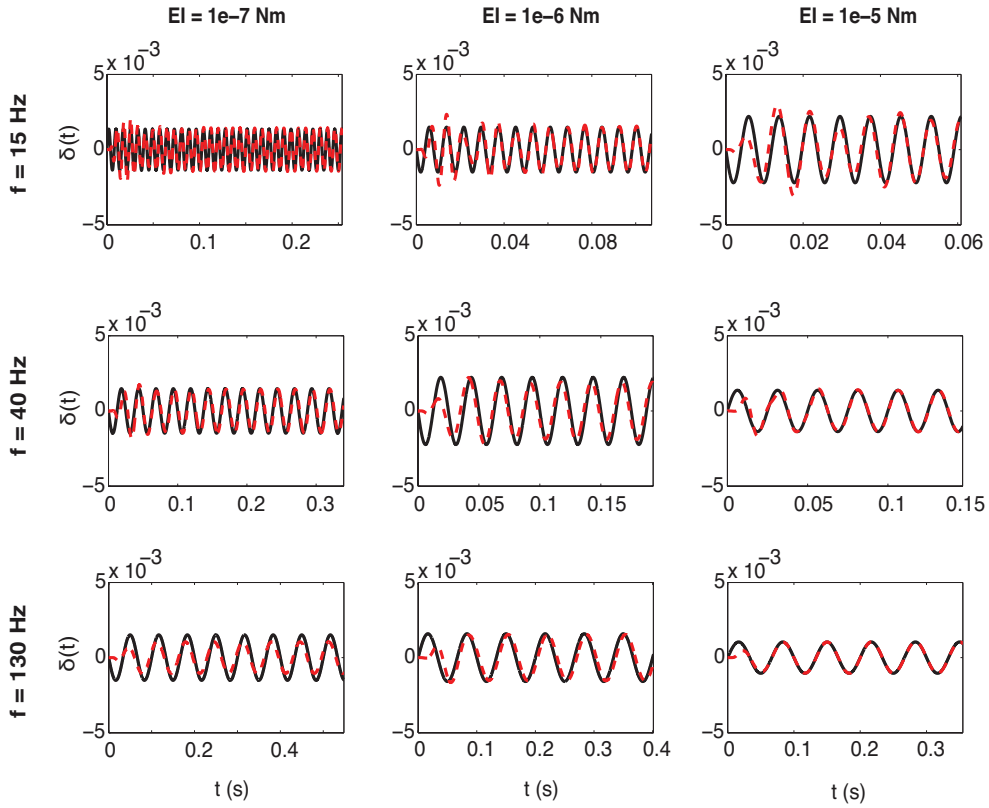

Figure S8. Tip displacement of the model (dashed red) and the analytical solution (solid black) for a beam undergoing vertical ground motions (heaving) at the leading edge (input amplitude equal to 0.001 m). Results in meters are shown over time for three frequencies of oscillation: f = 15, f = 40 Hz, and f = 130 Hz (rows one to three, respectively) and three flexural stiffnesses (EI): 1e-7 Nm^2, 1e-6 Nm^2, and 1e-5 Nm^2 (columns one to three, respectively). All simulations were computed for a beam with four elements along the length, which is consistent with the text.

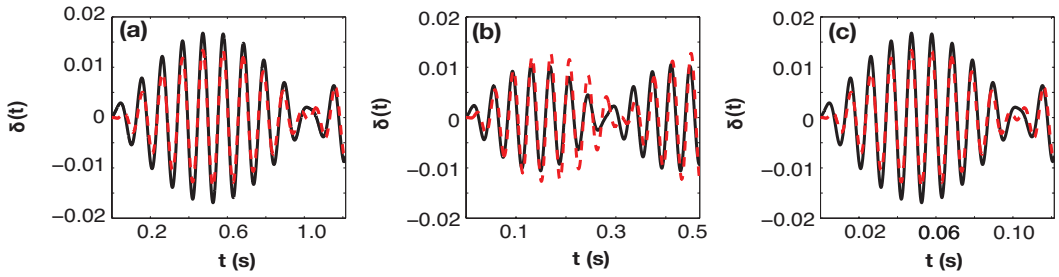

Figure S9. Comparison between tip displacement as computed by the model (dashed red) and by the analytical solution (solid black) for a beam undergoing vertical ground motions (heaving) at the leading edge near the resonant frequency of beams with three different flexural stiffnesses: 1e-7 Nm^2 with f = 10 Hz (a), 1e-6 Nm^2 with f = 25 Hz (b), and 1e-5 Nm^2 with f = 100 Hz (c). Due to the lack of damping in the system, these results were computed using double the number of elements as figure S8.

CONVERGENCE TESTING

In order to determine the critical time step required for our model to converge, we examined how the tip displacement of the solid model and the lift generated by the fluid model varied as we changed the size of our time step. We performed this analysis for nine different simulations that spanned the parameter space of interest to us: three stiffnesses (1e-5 Nm^2, 1e-6 Nm^2, and 1e-7 Nm^2) at each of three frequencies of actuation (10 Hz, 25 Hz, and 100 Hz). As expected, as the stiffness of the solid model increased, the time step size needed for the solid model to converge decreased (figure S10). Additionally, as the frequency of actuation increased, the time step size required for the solid model to converge decreased. Overall, our analysis of the solid model indicated that a reasonable time step size for our range of parameters was around 1e-6 s.

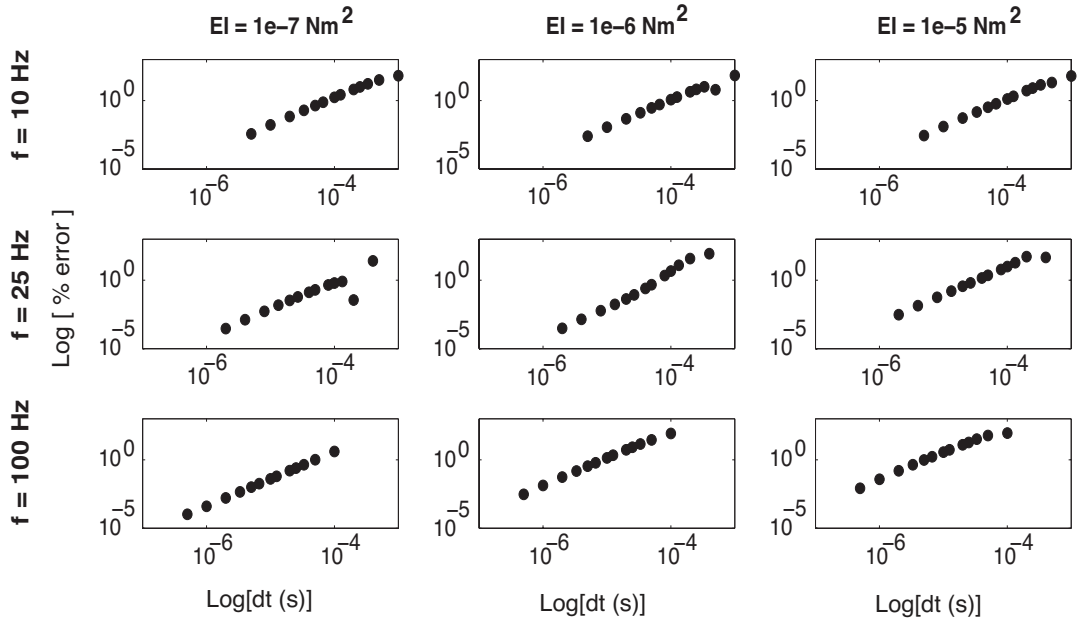

Figure S10. Relative error in the tip displacement of the solid model (as compared to the smallest time step) varies as time step size changes for a plate being pitched and heaved about the leading edge at three frequencies of oscillation: f = 10 Hz (first row), f = 25 Hz (second row), and f = 100 Hz (third row). The columns depict the tip displacement for three different flexural stiffnesses (EI): 1e-7 Nm^2, 1e-6 Nm^2, and 1e-5 Nm^2.

In order to evaluate the importance of spatial error over temporal error, we also performed an analysis of element size in conjunction with time step size (figure S11). We varied both element size and time step size together (*i.e.* time step size was changed linearly with element size) to ensure that temporal error was the dominant factor for the time step chosen. Figure S11 shows that the results remain very similar over the range of element and time step sizes used. As a result, we concluded that a time step size of 4e-6 for the solid model and element number of four were sufficient for our analysis.

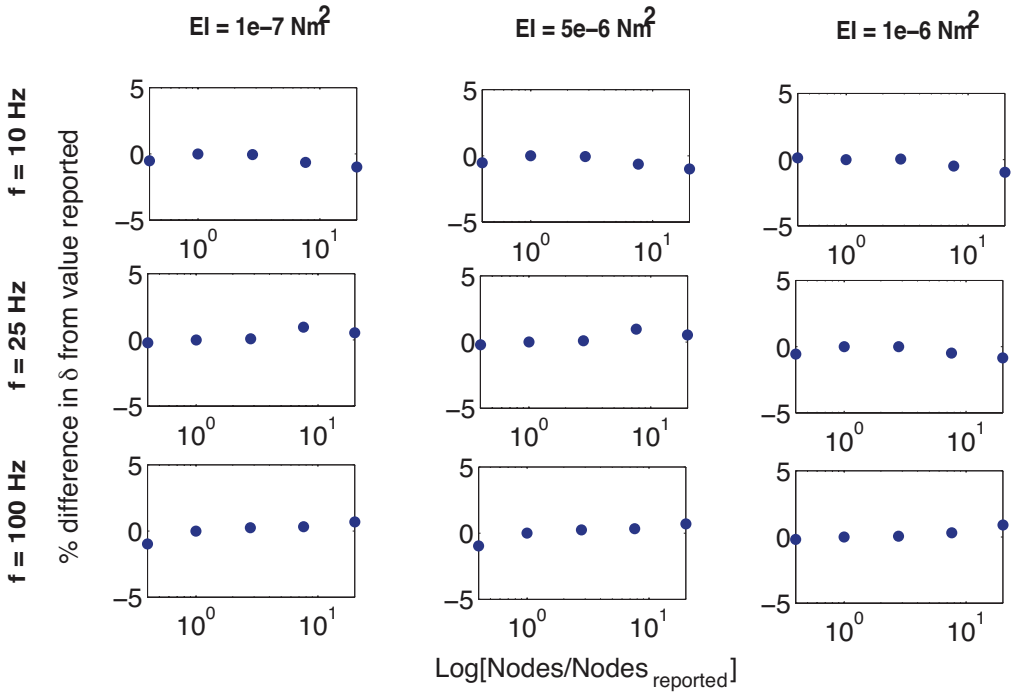

Figure S11. Relative error in the tip displacement of the solid model varies with element size as time step changed linearly with element size. Results presented are for a plate being pitched and heaved about the leading edge at three frequencies of oscillation: f = 10 Hz (first column), f = 25 Hz (second column), and f = 100 Hz (third column). The columns depict the amount of error in the tip displacement (as compared to the smallest time step) for three different flexural stiffnesses (EI): 1e-7 Nm^2, 1e-6 Nm^2, and 1e-5 Nm^2. As above, Nodes$_{reported}$ was set to five. Thus, the range of nodes reported on the x-axis for each plot goes from 2 nodes (1 element) to 100 nodes (99 elements).

On the other hand, the fluid model did not appear to need as small of a time step as the solid model (figure S12). A time step size of 2e-4 s was sufficient to achieve the accuracy we desired. As a result, to maximize the efficiency of our model, we chose to use a fluid time step of 2e-4 and to subsample the solid 50 times at every time step.

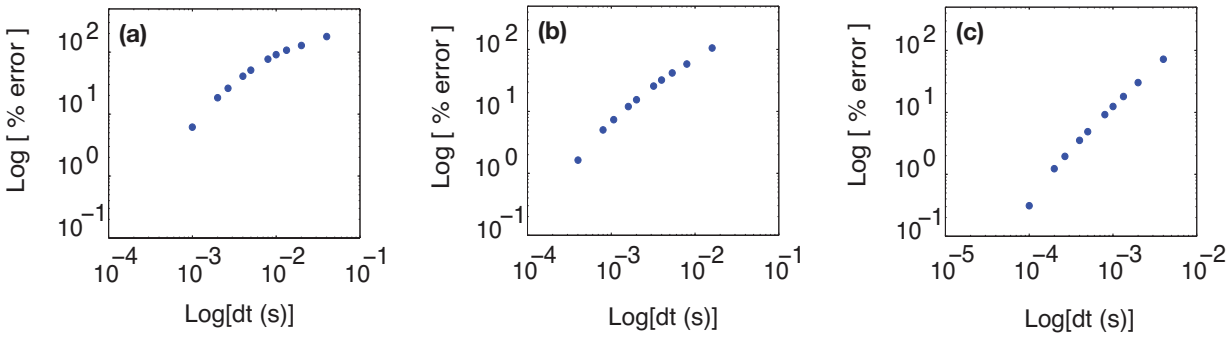

Figure S12. Relative error in the coefficient of lift, C_l, as computed with the fluid model at varying time step sizes for a plate being pitched and heaved about the leading edge at three frequencies of oscillation: f = 10 Hz (a), f = 25 Hz (b), and f = 100 Hz (c). The y-axis is the amount of error in the tip displacement (as compared to the smallest time step) and the x-axis is the size of the time step.

COMPUTING METHODOLOGY

In order to speed up the computation, we launched our simulations through MATLAB's Cloud Center in conjunction with Amazon Web Services (AWS). Using this approach we ran eight 16-core machines via AWS Elastic Cloud Compute, each with 16 MATLAB processes running under MATLAB's Distributed Computing License. As a result, we ran simulations up to 32 times faster than on a 4-core desktop machine.

MODEL ANIMATIONS

We included three animations of model simulations to demonstrate how the wake structure changes as the frequency of actuation varies. We slowed down all three animations by a factor of 100 to improve the viewing experience. While the flexural stiffness used for all three simulations was fixed at 10^{-6} N m^2, we used three different frequencies of actuation: 10 Hz, 48 Hz, and 100 Hz (animations 1, 2, and 3, respectively).

APPENDIX 2:
SUPPLEMENTARY MATERIAL FOR FLAPPING, ROTATING WING MODEL

This appendix contains additional information about the computational model of a flapping, rotating wing that was described in Chapter 4.

SUPPLEMENTAL DETAILS ABOUT COMPUTATIONAL MODEL

We used energy methods to simulate the structural dynamics of a flapping, flexing wing undergoing body rotations. We described the wing deformation by employing a linear combination of shape functions to describe the curvature of the wing and by prescribing a distribution of mass and stiffness over the wing's surface using a plate model. We then derived expressions for the kinetic and potential energies of the plate, including inertial terms generated by rotations of the wing, and used Lagrange's equations to solve for the position and velocity of the wing with kinematics prescribed at the wing base.

We simulated a flapping motion by constraining the two corners at the base of the wing to undergo periodic local rotation about the *x*-axis (see main text for details). We then solved for the deformation of the plate by allowing the other two corners of the plate to have three degrees of freedom (see inset in figure 4.1). Thus, our plate model only had six degrees of freedom given by the generalized coordinate vector

$$\vec{q}(t) = \begin{bmatrix} \delta_1 & \phi_3 & \theta_3 & \delta_4 & \phi_4 & \theta_4 \end{bmatrix}^T \tag{A2.1}$$

where δ_i is the linear displacement of the i^{th} node along the *z*-axis, ϕ_i is the angular displacement of the i^{th} node about the *x*-axis, and θ_i is the angular displacement of the i^{th} node about the *y*-axis (as shown in figure 4.1).

We used the six generalized coordinates given by equation A2.1, along with a vector of shape functions, $\vec{N}(x,y)$, to describe the deformation of the plate

$$w(x,y,t) = \left[\vec{N}(x,y)\right]^T \vec{q}(t) \tag{A2.2}$$

that varied over both space (*x, y*) and time, *t*. We used shape functions derived from fourth-order polynomials that satisfy the boundary conditions. For the i^{th} node, the shape functions, which vary over space (*x, y*), and are given by

$$\vec{n}_i(x,y) = \begin{bmatrix} \frac{1}{8}(1+\xi_0)(1+\eta_0)\left(2+\xi_0+\eta_0-\xi^2-\eta^2\right) \\ \frac{a}{8}\xi_i(1+\xi_0)^2(\xi_0-1)(\eta_0+1) \\ \frac{b}{8}\eta_i(1+\eta_0)^2(1+\xi_0)(\eta_0-1) \end{bmatrix} \tag{A2.3}$$

with normalized coordinates given by

$$\xi = \frac{x-x_c}{a} \tag{A2.3a}$$

$$\xi_i = \frac{x_i-x_c}{a} \tag{A2.3b}$$

$$\xi_0 = \xi\xi_i \tag{A2.3c}$$

$$\eta = \frac{y-y_c}{b} \tag{A2.3d}$$

$$\eta_i = \frac{y_i-y_c}{b} \tag{A2.3e}$$

$$\eta_0 = \eta\eta_i \tag{A2.3f}$$

where 2*a* and 2*b* are the width and length of the plate, respectively, (x_c, y_c) = (0, *b*) is the location of the plate's center, and (x_i,y_i) is the position of the i^{th} node.

Once we described the local deformation of the plate using equation A2.2, we could then describe the position all points on the plate as measured in the plate's reference frame, *A*, as

$${}^A\vec{r}^{\,m}(x,y,t) = \begin{bmatrix} x & y & w(x,y,t) \end{bmatrix}^T \tag{A2.4}$$

where *x* and *y* describe the position of each point of mass in space and *t* is time. As indicated, the *x*- and *y*-coordinates remain constant (the wing is not allowed to stretch in either direction) and the *z*-coordinate varies according to the vertical displacement, or bending, of the wing.

We used the position of the wing's surface given by equation A2.4 to derive the equations of motion when a body rotation was applied to the wing's reference frame (details about the rotation can be found in equations 5 and 6 the main text). We chose to solve this system of equations using energy methods, specifically using Lagrange's equation. To formulate Lagrange's equation, we first computed the Lagrangian

$$L = T - V \tag{A2.5}$$

where T and V are the kinetic and potential energies of the plate model.

The kinetic energy of the plate is given by

$$\mathrm{T} = \frac{1}{2}\rho h \int_{0}^{2b}\int_{-a}^{a} {}^{S}\vec{v}^{m} \cdot {}^{S}\vec{v}^{m} dxdy \tag{A2.6}$$

where r and h are the density and thickness of the plate and ${}^{S}\vec{v}^{m}$ is the velocity of every element of mass, m, in the inertial frame, S. The velocity of a point, m, on the plate's surface in the inertial frame, S, is given by

$${}^{S}\vec{v}^{m} = {}^{S}\vec{v}^{o} + \frac{d}{dt}\left({}^{A}\vec{r}^{m}\right) + \vec{\Omega} \times {}^{A}\vec{r}^{m} \tag{A2.7}$$

where ${}^{S}\vec{v}^{o}$ is the velocity of the origin of the wing's reference frame, which we prescribed to be $[0,\ 0,\ 0]^{T}$ for simplicity, ${}^{A}\vec{r}^{m}$ is the position vector described above, and $\vec{\Omega}$ is the angular velocity of the wing's reference frame. In order to write the angular velocity of the wing's reference frame and the position of the points on the plate's surface in the same coordinate system (*e.g.* the plate's coordinate system), we must multiply the angular velocity vector by a rotation matrix. Thus, the angular velocity of the wing's reference frame, written using the coordinate system of the wing, is given by

$$\vec{\Omega} = R\ {}^{S}\vec{\Omega}^{A} \tag{A2.8}$$

where ${}^{S}\vec{\Omega}^{A}$ is the angular velocity of the wing's reference frame given in the main text, R is a rotation matrix given by

$$R = \begin{bmatrix} \cos(\theta) & -\sin(\theta) & 0 \\ \sin(\theta) & \cos(\theta) & 0 \\ 0 & 0 & 1 \end{bmatrix} \tag{A2.9}$$

and θ is the angle of the body rotation given by

$$\theta = \int \omega(t)\,dt \tag{A2.10}$$

where $\omega(t)$ is the angular velocity of the body.

In addition, the potential energy of the wing is given by

$$V = \frac{h^3}{24}\int_0^{2b}\int_{-a}^{a}\left[\bar{\chi}(x,y,t)\right]^T \bar{D}\left[\bar{\chi}(x,y,t)\right]dxdy \tag{A2.11}$$

where the strain energy is

$$\bar{\chi}(x,y,t) = \begin{bmatrix} \dfrac{\partial^2 w}{\partial x^2} & \dfrac{\partial^2 w}{\partial y^2} & \dfrac{\partial^2 w}{\partial x \partial y} \end{bmatrix}^T \tag{A2.11a}$$

and the stiffness matrix (assuming the wing is isotropic) is

$$\bar{D} = \frac{E}{\left(1-\upsilon^2\right)}\begin{bmatrix} 1 & \upsilon & 0 \\ \upsilon & 1 & 0 \\ 0 & 0 & (1-\upsilon) \end{bmatrix} \tag{A2.11b}$$

where ν is the Poisson's ratio and E is the Young's modulus of the wing.

Once we formulated the Lagrangian, we then solved for Lagrange's equation

$$\frac{d}{dt}\left(\frac{\partial L}{\partial \dot{q}_i}\right) - \frac{\partial L}{\partial q_i} = F_i \tag{A2.12}$$

where q_i are the generalized coordinates and F_i are the generalized forces at each node. The final equation is given by

$$\frac{d^2\bar{q}(t)}{dt^2} = M^{-1}M_a\frac{d\bar{v}_o}{dt} + \left(\frac{d\Phi}{dt}\right)^2\bar{q}(t) - M^{-1}K\bar{q}(t) + M^{-1}I_C R\,{}^S\bar{\Omega}^A - M^{-1}\eta\frac{d\bar{q}(t)}{dt} \tag{A2.13}$$

where $\bar{q}(t)$ is the vector of generalized coordinates given by equation A2.1, ${}^S\bar{\Omega}^A$ is the angular velocity of the wing in the inertial frame given by equation 4.5, R is the rotation matrix given by equation A2.9, Φ is the flapping rotation about the x-axis given by equation 4.1a, η is the damping factor, and the matrices M, M_a, K, and I_C and the vector $\bar{v}_o$ are given below. The mass and stiffness matrices are defined by

$$M_{ij} = \rho h \int_0^{2b} \int_{-a}^{a} \bar{N}_i(x,y)\bar{N}_j(x,y)\,dx\,dy \tag{A2.14}$$

and

$$K_{ij} = \frac{h^3}{12} \int_0^{2b} \int_{-a}^{a} \left(\frac{\partial^2 \bar{\chi}(x,y,t)}{\partial x^2} \right)^T D \left(\frac{\partial^2 \bar{\chi}(x,y,t)}{\partial x^2} \right) dx\,dy \tag{A2.15}$$

respectively, where the shape functions, strain energy, thickness, and stiffness matrix are the same as above. The applied acceleration mass matrix is given by

$$M_{a_i} = \begin{bmatrix} 0 & 0 & \int_0^{2b} \int_{-a}^{a} \rho h N_i(x,y)dxdy & \int_0^{2b} \int_{-a}^{a} y\rho h N_i(x,y)dxdy & -\int_0^{2b} \int_{-a}^{a} x\rho h N_i(x,y)dxdy & 0 \end{bmatrix} \tag{A2.16}$$

and the inertia-like matrix that describes the contribution of the Coriolis force is given by

$$I_C = I_{Cori} \begin{bmatrix} 0 & 0 & 0 \\ 0 & 0 & -\frac{d\Phi}{dt}\cos(\theta) \\ 0 & 0 & -\frac{d\Phi}{dt}\sin(\theta) \end{bmatrix} \tag{A2.17}$$

where θ is the angle of the body rotation described above, Φ is the flapping rotation about the x-axis given by equation 4.1a, and the inertia contributing to the Coriolis force, $I_{Cori,i}$, is given by

$$I_{Cori,i} = \begin{bmatrix} \int_0^{2b} \int_{-a}^{a} \rho h N_i(x,y)\,dx\,dy & \int_0^{2b} \int_{-a}^{a} x\rho h N_i(x,y)\,dx\,dy & \int_0^{2b} \int_{-a}^{a} y\rho h N_i(x,y)\,dx\,dy \end{bmatrix} \tag{A2.17a}$$

and, finally, the vector that describes the linear and angular velocities of the body is given by

$$\bar{v}_o = \begin{bmatrix} 0 & 0 & 0 & \frac{d\phi}{dt}\cos(\theta) & \frac{d\phi}{dt}\sin(\theta) & \omega(t) \end{bmatrix}^T \tag{A2.18}$$

Thus, we generated a system of six, second-order ordinary differential equations. We then used a fourth-order Runge Kutta scheme in MATLAB (The MathWorks, Natick, MA, USA) to solve these equations for the generalized coordinates over ten rotation cycles.

Taking Differences in the Frequency Domain

Due to our limited ability to phase-match the experimental data for the cases of flapping alone (figure S13a) and flapping and rotating (figure S13b), when we compared our computational and experimental results, we chose to take a difference between the amplitude of the signals in the frequency domain (*i.e.* the difference of the amplitudes of the fast Fourier transforms (FFTs), figure S13ai-bi). By computing these differences in the frequency domain, we could ignore the arbitrary phase difference that arises from when we began sampling our signals for the two cases of flapping with and without rotation. Taking this difference also allowed us to subtract out any consistent noise across the trials. Thus, we were able to view only the changes in the signal that occur as a result of the imposed rotation (figure S13c).

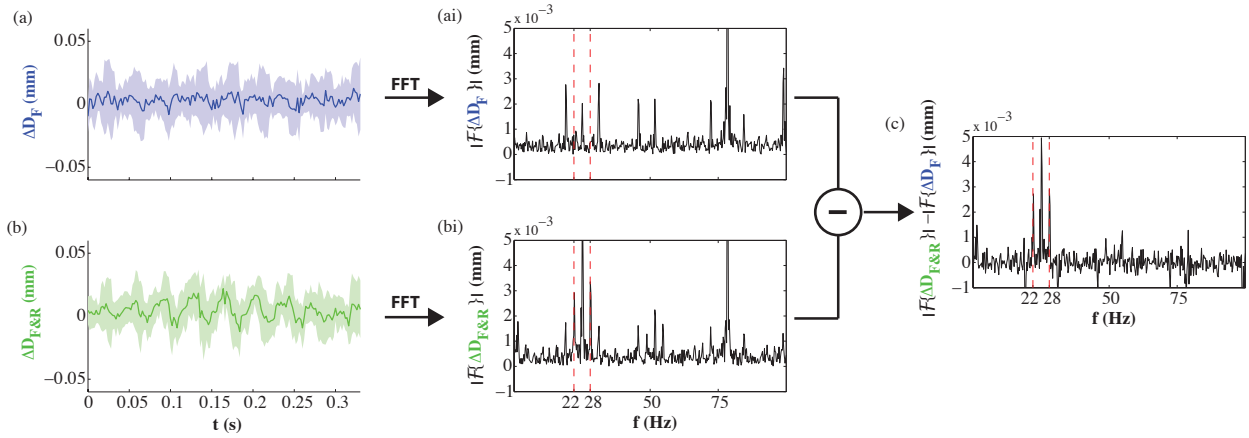

Figure S13. Computing the difference of two signals in the frequency domain. The difference between the displacements of the endpoints (*DD*) for flapping alone (a) and flapping and rotating (b) changes over time during a single rotation cycle. In order to compare these signals, we first compute the amplitude of the fast Fourier transforms (FFTs) of each signals versus frequency (ai and bi, respectively). Finally, we take the difference between the amplitude of these two FFTs to get the difference between the amplitude at every frequency (c). Note the peaks at the flapping frequency (25 Hz) plus and minus the rotation frequency (3 Hz) (highlighted by red dashed lines).

In the main text (figures 4.6-4.8) we only report the difference in the FFTs (*e.g.* figure S1c) and not the raw spectra (figures S13ai-bi). However, we provide the raw spectra for all cases (figures 4.6-4.8) as supplemental figures (figures S14-S16). Because we used an analog function generator in our experimental setup, we did not have the ability to control the flapping frequency to within less than 0.5%. As a result, the frequencies for all of our experimental trials varied by up to 0.125 Hz. These slight variations in flapping frequency, due only to the precision of our function generator, could result in large amplitude differences near the flapping frequency and its harmonics (figures S14c-16c). If the flapping frequency during rotation was even slightly different than the flapping frequency without rotation, taking the difference between the signals in the frequency domain would result in a very large peak near the flapping frequency of ~25 Hz.

To examine the impact of 0.2% or 0.05% error, we ran additional simulations with the flapping frequency set to 25 Hz for flapping and rotating and 25.01 Hz or 25.05 Hz for flapping alone. Our results from this analysis showed that these slight differences in flapping frequencies for flapping with and without rotation do indeed result in large peaks in the difference of the FFTs near the flapping frequency (figure S17).

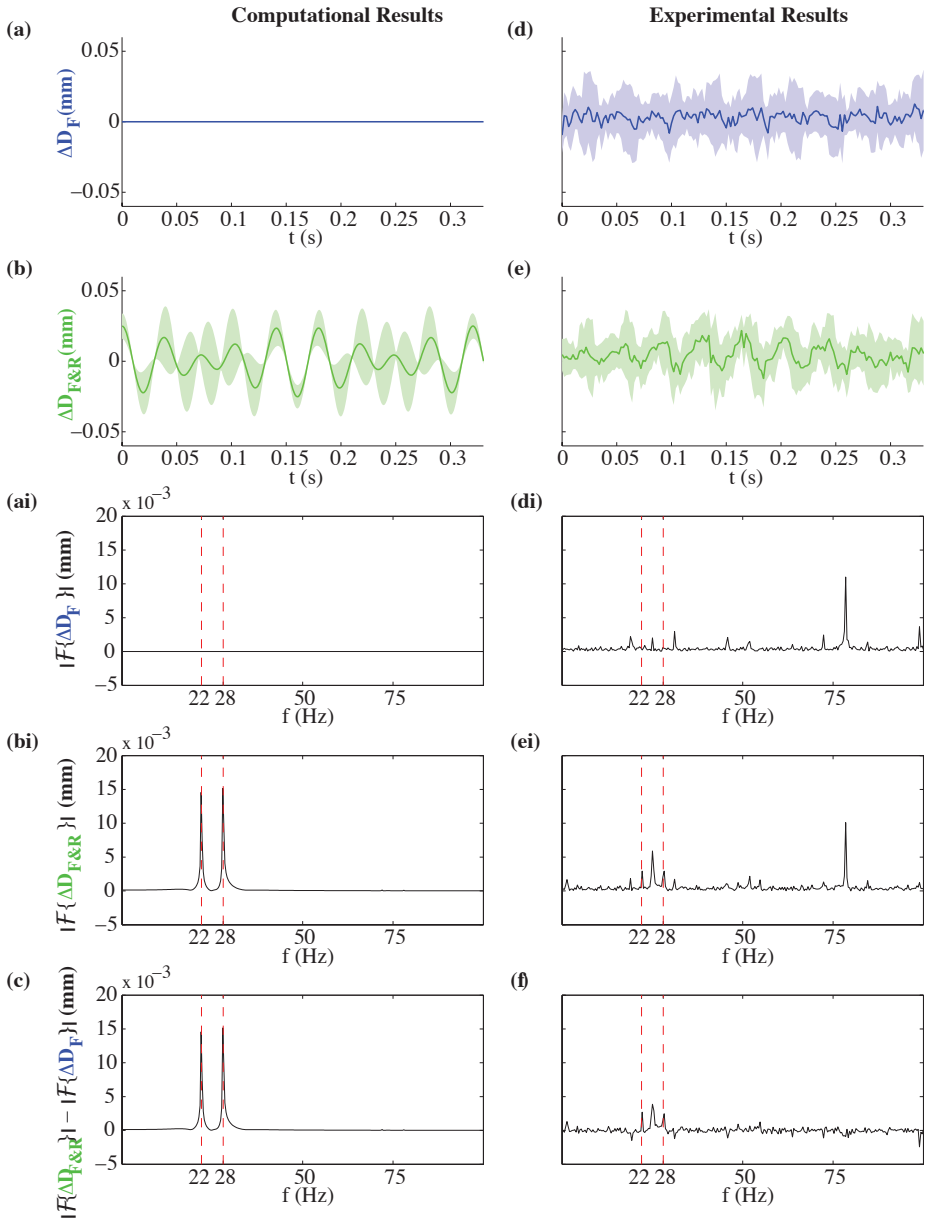

Figure S14. The difference between the displacement of the left (D_L) and right (D_R) endpoints of the wing, ΔD, versus time, t, for flapping alone (a,d) and flapping and rotating with periodic angular velocity (b,e). The subscripts of ΔD are F for flapping alone and $F\&R$ for flapping and rotating. Time domain results for a time-average taken over ten rotation cycles are shown for computational (a-b) and experimental (d-e) models. Shading denotes standard deviation. Frequency domain results of the amplitude of the fast Fourier transform (FFT) of each of the corresponding time-domain signals (ai-bi, di-ei). Finally, the difference in amplitude of the fast Fourier transforms (FFTs) of ΔD for flapping and rotating compared to flapping alone for the computational (c) and experimental (f) models. Note the peaks at the flapping frequency of 25 Hz, plus and minus the rotation frequency of 3 Hz.

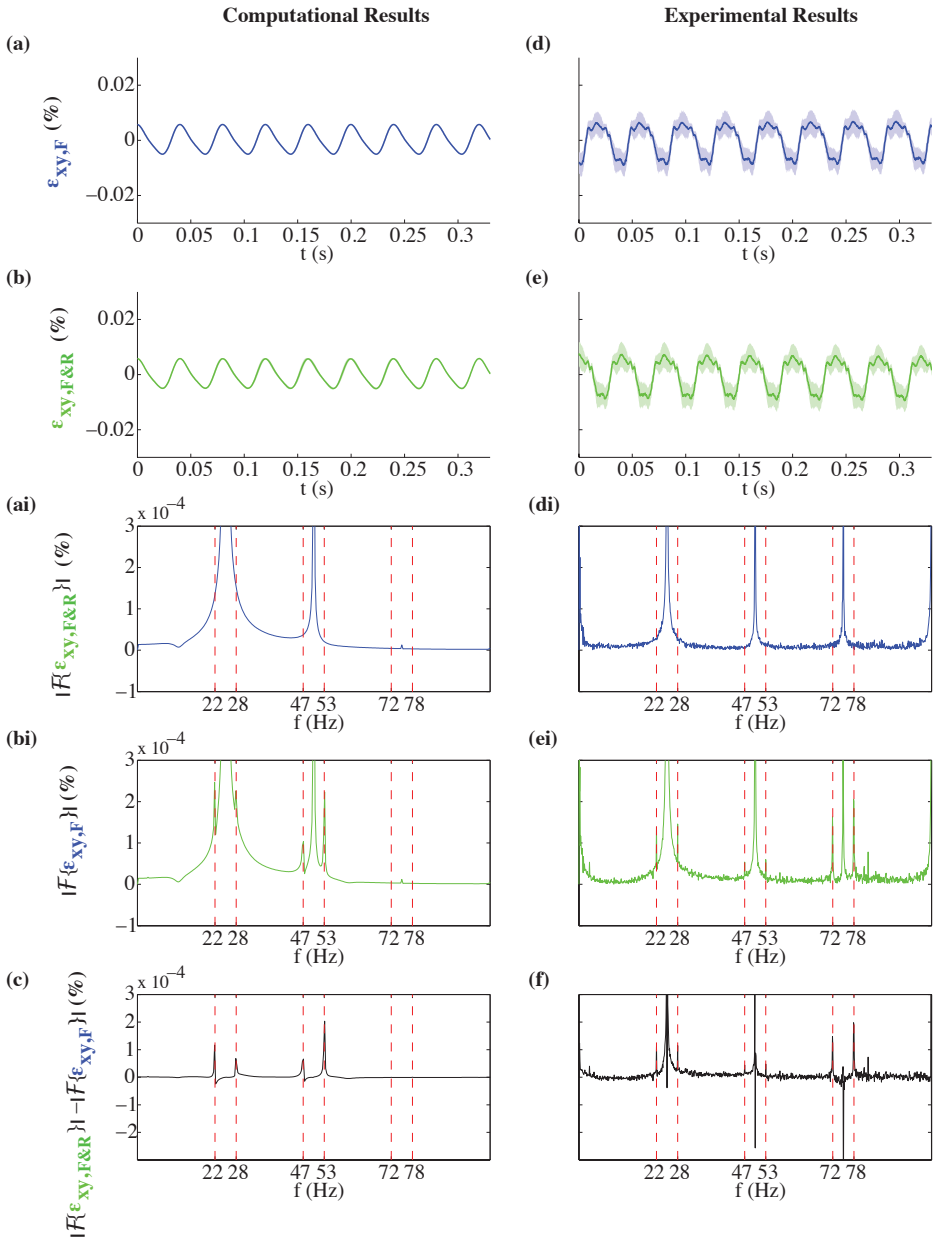

Figure S15. The shear strain at the quarter span along the mid chord ε_{xy} versus time, t, for flapping alone (a,d) and flapping and rotating with periodic angular velocity (b,e). The additional subscripts of ε_{xy} are F for flapping alone and $F\&R$ for flapping and rotating. Time domain results for a time-average taken over ten rotation cycles are shown for computational (a-b) and experimental (d-e) models. Shading denotes standard deviation. Frequency domain results of the amplitude of the fast Fourier transform (FFT) of each of the corresponding time-domain signals (ai-bi, di-ei). Finally, frequency domain results of the difference in amplitude of the fast Fourier transforms (FFTs) of ε_{xy} for flapping and rotating compared to flapping alone for the computational (c) and experimental (f) models. Note the peaks at the flapping frequency of 25 Hz, plus and minus the rotation frequency of 3 Hz, and their harmonics.

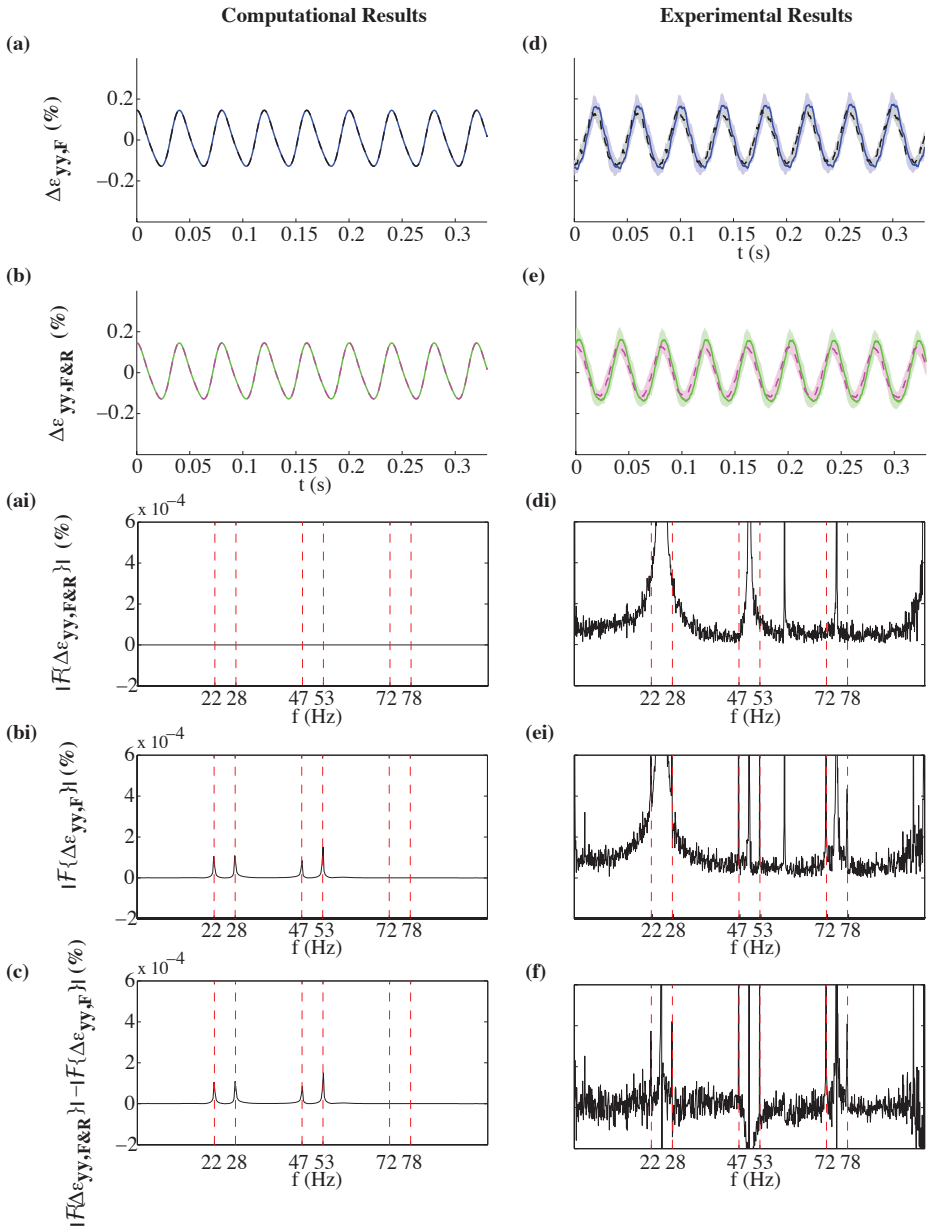

Figure S16. The normal strain along the span wise direction, ε_{yy}, on either side of the wing's chord (lift side - solid; right side - dashed) near the base of a model wing versus time, t, for flapping alone (a,d) and flapping and rotating with periodic angular velocity (b,e). The additional subscripts of ε_{yy} are F for flapping alone and $F\&R$ for flapping and rotating. Time domain results for a time-average taken over ten rotation cycles are shown for computational (a-b) and experimental (d-e) models. Shading denotes standard deviation. Frequency domain results of the amplitude of the fast Fourier transform (FFT) of each of the corresponding time-domain signals (ai-bi, di-ei). Finally, frequency domain results of the difference in amplitude of the fast Fourier transforms (FFTs) of the difference between the left and right normal strains, $\Delta\varepsilon_{yy}$, for flapping and rotating compared to flapping alone for the computational (c) and experimental (f) models. Note the peaks at the flapping frequency of 25 Hz, plus and minus the rotation frequency of 3 Hz, and their harmonics.

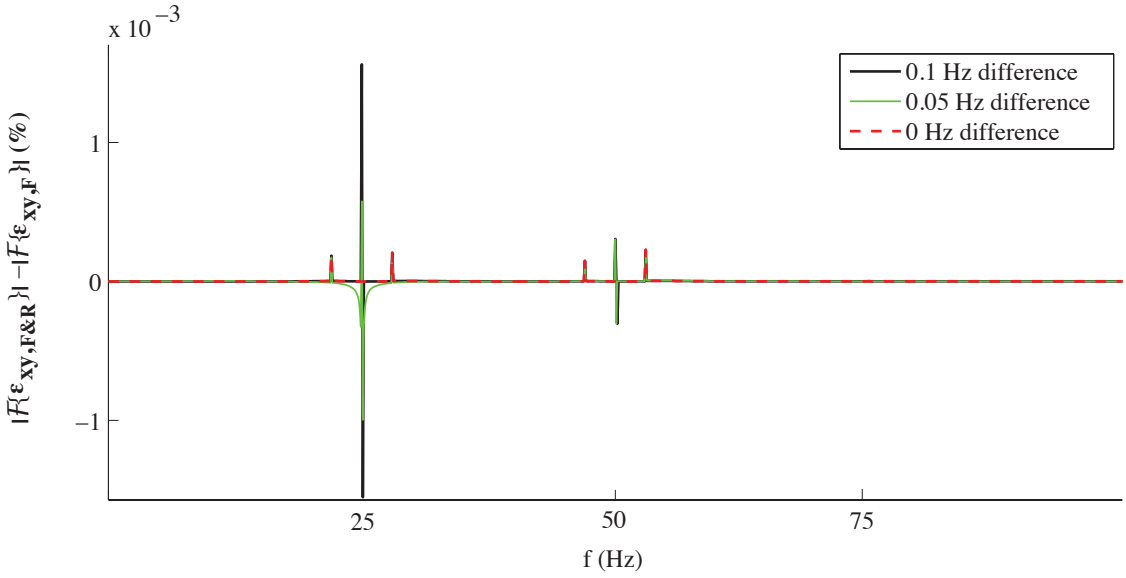

Figure S17. Computational results for the difference in the amplitudes of the FFTs for shear strain at the quarter span along the mid chord ε_{xy} between flapping alone and flapping and rotating with periodic angular velocity. The additional subscripts of ε_{xy} are *F* for flapping alone and *F&R* for flapping and rotating. Each color corresponds to the difference in flapping frequencies input into the model for flapping alone versus flapping and rotating (see legend in upper right corner). Differences of 0.1 Hz and 0.05 Hz are compared to a 0 Hz difference (ideal case, only really achievable theoretically). For the ideal case, there are only four peaks, at the flapping frequency of 25 Hz plus and minus the rotation frequency of 3 Hz and the first harmonics around 47 and 53 Hz. For the other cases (*i.e.* slight differences in flapping frequencies, which would be associated with imprecision of the function generator in the experimental setup), the signals also contain additional peaks at near the flapping frequency (25 Hz) and its first harmonic (50 Hz). These large peaks explain the differences we observe between the computational and experimental model.

SUPPLEMENTAL DATA AND CODE

We supply all data collected from our experimental and computational models along with the code we wrote for the computational wing model at the following link: https://github.com/eberlea/TorsionWing. This repository contains 25 files. We saved all of the data in 'RawData_Experimental_and_Computational.mat', which can be opened using MATLAB (The MathWorks, Natick, MA, USA). The remaining 24 files are scripts that can be executed in MATLAB. We created the following files for the computational model:

List of simulations:	‘runsimulations.m’
Main functions:	‘flappermodel_doublesine.m’
	‘flappermodel_singlesine.m’
Sub functions:	‘createODEfile.m’
	‘PlateODE.m’ (generated by ‘createODEfile.m’)
	‘funcCa.m’
	‘shape2.m’
	‘shapefunc2.m’

We used the rest of the files for post processing, where the main figure plotting scripts are ‘plot_Figures4to8.m’ and ‘plot_FiguresS1-S9.m’.

SUPPLEMENTAL ANIMATIONS

To better illustrate the spatiotemporal variation in strain over the surface of the wing model when the wing is flapped while also rotated, we generated three animations of our computational results. These animations are called ‘constant_2flapcycles_playedback200timesslower.mp4’, ‘periodic_2flapcycles_playedback200timesslower.mp4’, and ‘periodic_2rotcycles_playedback50timesslower.mp4’. As each title indicates, the animations illustrate either constant or periodic angular velocity rotation of the body for either two flapping cycles or two rotations cycles and are played back at either 50 or 200 times slower than real time. For each animation, the title at the top indicates the type of rotation being shown along with the time, in seconds, at which each frame is played. The upper left panel indicates the flapping angle (in radians) and the upper right panel indicates the rotation angle (in radians). The red dots in each of these two upper panels indicate the corresponding angles for each frame. The four panels on the bottom indicate the difference in tip displacement, Dz, between flapping versus flapping and rotating (in mm); the difference in normal strain along the y-axis, De_{yy} (in % strain); normal strain along the x-axis, De_{xx} (in % strain); and shear strain in the x-y plane, De_{xy} (in % strain).

SUPPLEMENTAL FIGURES FOR SPATIAL DISTRIBUTION OF STRAIN

We generated two supplemental figures to show how the actual values, rather than relative values, of strain and displacement vary over the surface of the wing for just flapping (figure S18) and for flapping with constant rotation (figure S19). These figures show that the wing bends when it is flapped and also when it is flapped and rotated. Figure 4.5 in the main text is the difference between figures S18 and S19 and illustrates the difference in the wing dynamics due to flapping with rotation as compared to just flapping alone. As shown in figures S18 and S19, the magnitudes of the displacement and strain are 100 times larger than the difference between them (figure 4.5). Thus, the displacement due to the torsion generated by gyroscopic forces (figure 4.5) is 100 times smaller than the bending displacement of the wing when it is flapped or flapped and rotated (figures S18 and S19).

We also provide two supplemental figures to show how the actual (figure S20) and relative (figure S21) values of strain and displacement vary over the surface of the wing when the wing is flapped and rotated with periodic angular velocity about the z-axis. As shown, for a single flapping cycle, the spatial patterns of the actual and the relative strain and displacement under periodic rotation (figures S20 and S16) are fairly similar to those for constant rotation (figure s S19 and 4.5). However, when the wing is flapped and rotated periodically, the differences in strain and displacement vary over the span of the rotation cycle, in addition to the flapping cycle. While it is difficult to see this variation in a single figure, please refer to our animations for an illustration of the beating that occurs in the difference in strain and displacement under periodic rotation.

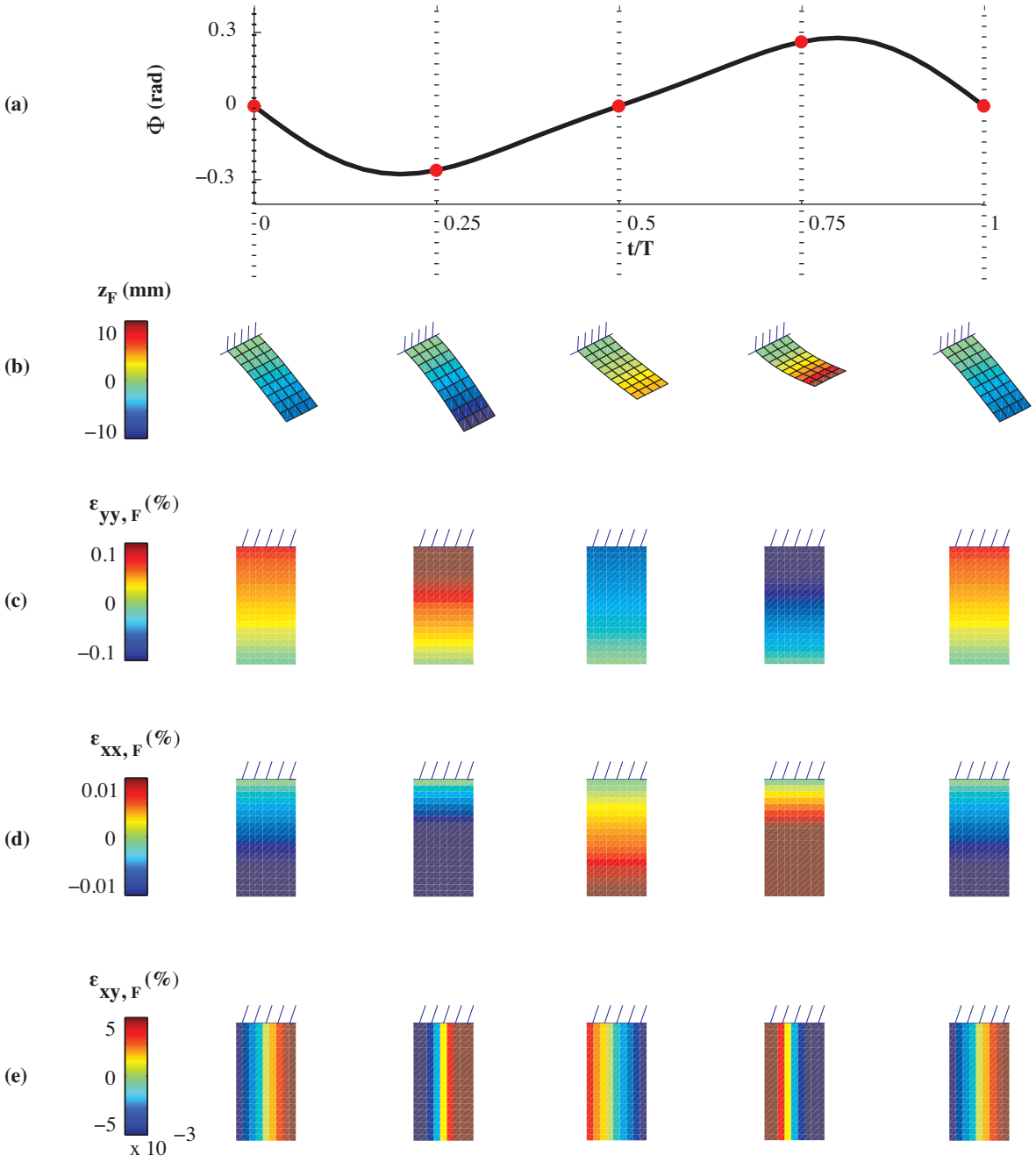

Figure S18. Spatiotemporal patterns of strain emerge in the computational model when the wing is flapped. The input flapping angle, f, varies over the relative time in the flapping cycle, t/T (a). Spatial contours of the magnitudes of the tip displacement, z_F (b), normal strain along the y-axis, $\varepsilon_{yy,F}$ (c), normal strain along the x-axis, $\varepsilon_{xx,F}$ (d), and shear strain in the x-y plane, $\varepsilon_{xy,F}$ (e), are shown at several snapshots in time (indicated by the filled circles and dotted vertical lines in (a)). Colouring indicates the magnitude of each parameter as indicated by the colour bars on the far left.

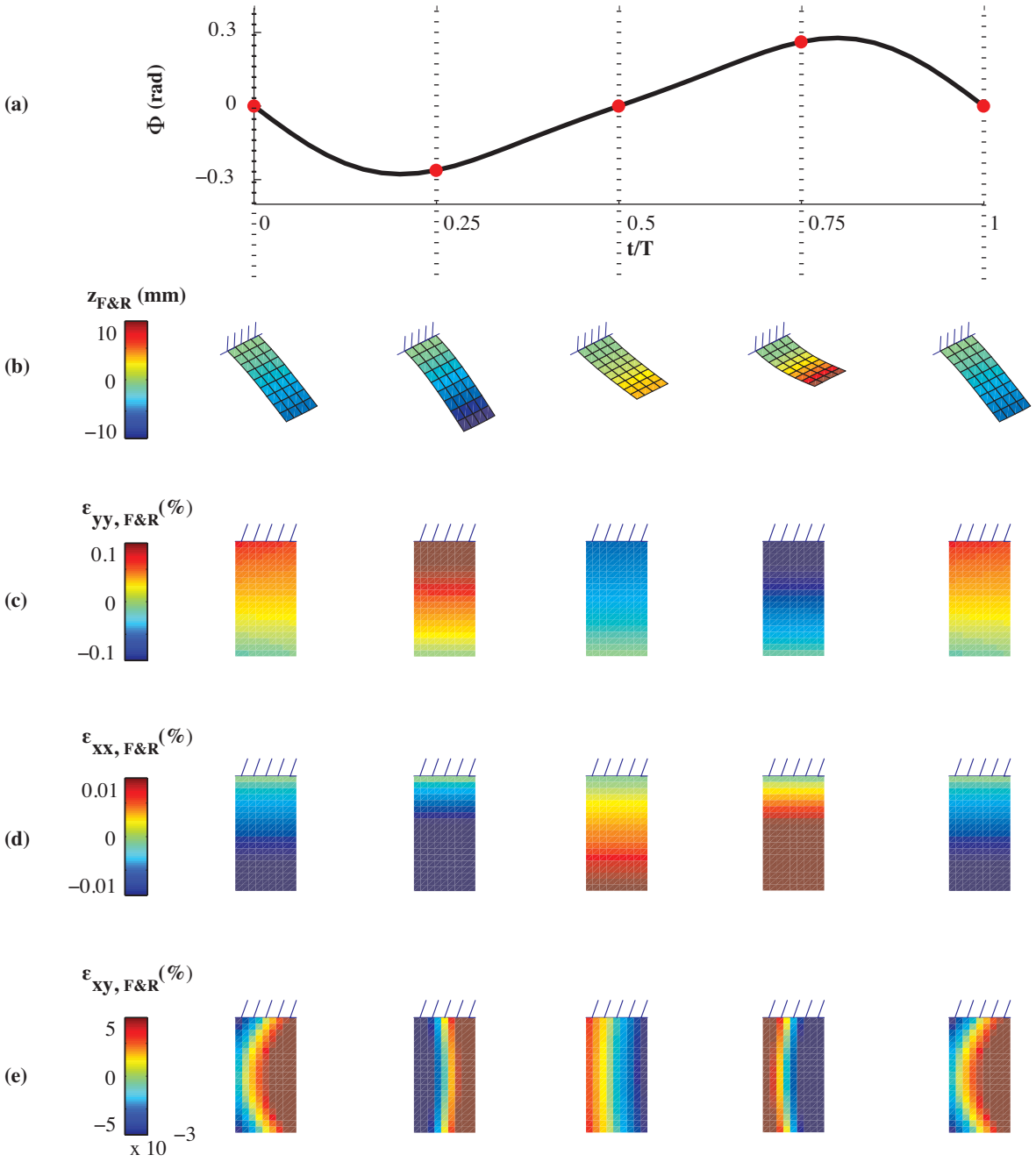

Figure S19. Spatiotemporal patterns of strain emerge in the computational model when the wing is flapped while the body is rotated with constant angular velocity of 800°/s about the *z*-axis. The input flapping angle, *f*, varies over the relative time in the flapping cycle, *t/T* (a). Spatial contours of the magnitudes of the tip displacement, $z_{F\&R}$ (b), normal strain along the *y*-axis, $\varepsilon_{yy,F\&R}$ (c), normal strain along the *x*-axis, $\varepsilon_{xx,F\&R}$ (d), and shear strain in the *x*-*y* plane, $\varepsilon_{xy,F\&R}$ (e), are shown at several snapshots in time (indicated by the filled circles and dotted vertical lines in (a)). Colouring indicates the magnitude of each parameter as indicated by the colour bars on the far left.

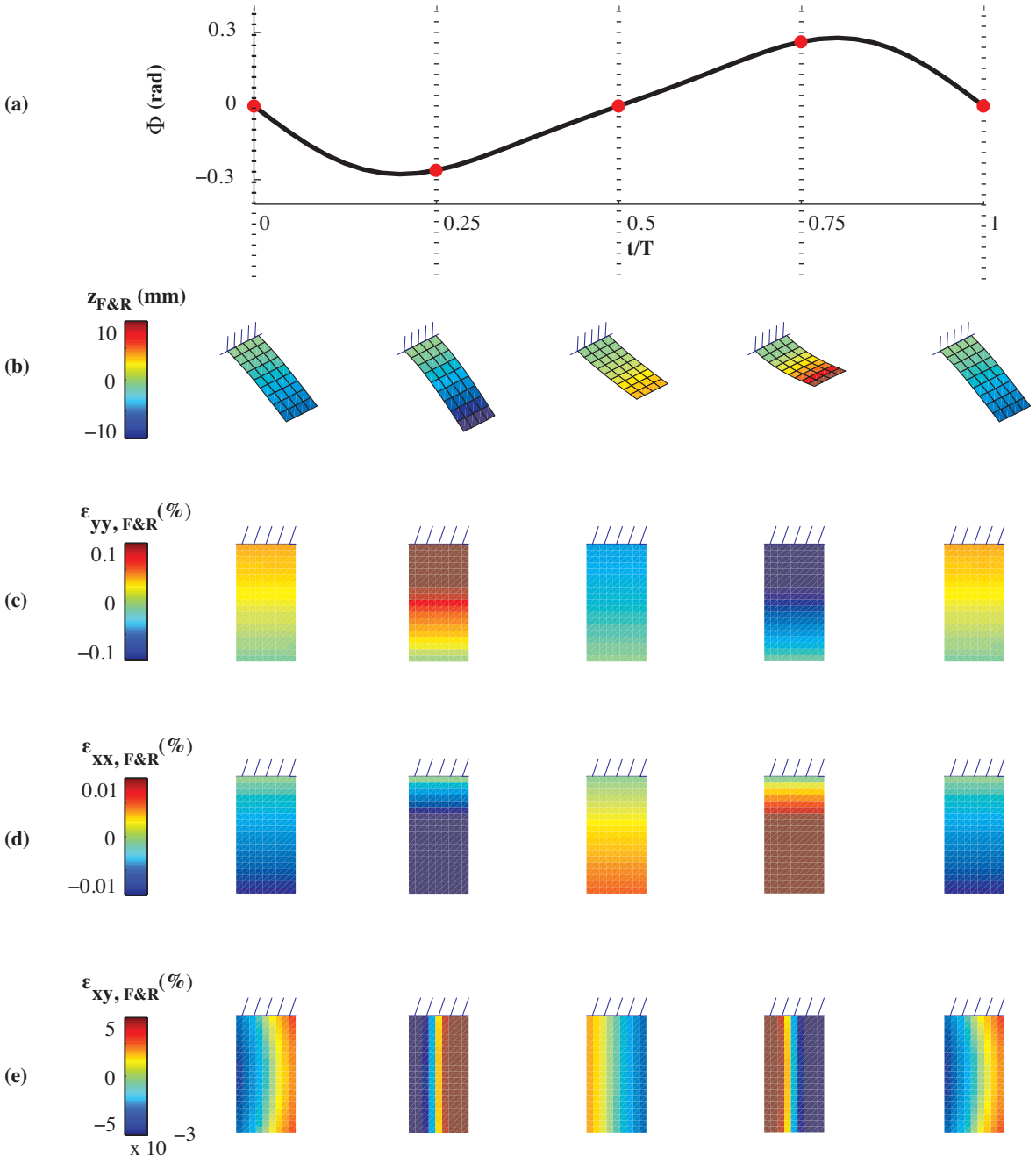

Figure S20. Spatiotemporal patterns of strain emerge in the computational model when the wing is flapped and rotated with periodic angular velocity about the *z*-axis ($f = 25$ Hz, $A = 10°$). The input flapping angle, f, varies over the relative time in the flapping cycle, t/T (a). Spatial contours of the magnitudes of the tip displacement, $z_{F\&R}$ (b), normal strain along the *y*-axis, $\varepsilon_{yy,F\&R}$ (c), normal strain along the *x*-axis, $\varepsilon_{xx,F\&R}$ (d), and shear strain in the *x*-*y* plane, $\varepsilon_{xy,F\&R}$ (e), are shown at several snapshots in time (indicated by the filled circles and dotted vertical lines in (a)). Colouring indicates the magnitude of each parameter as indicated by the colour bars on the far left.

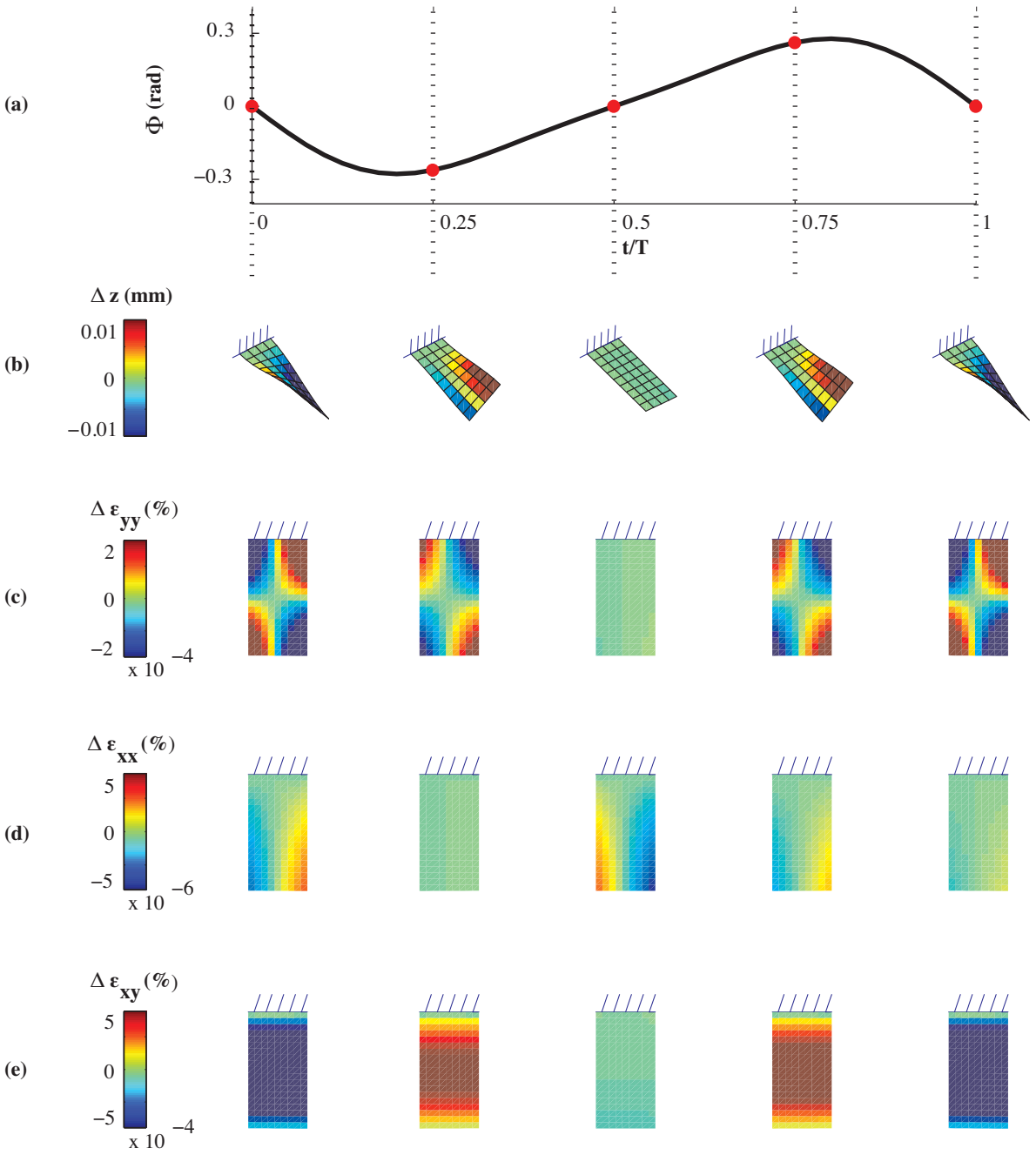

Figure S21. Differences between the spatiotemporal patterns of strain while the wing is flapped versus flapped and rotated with periodic angular velocity about the *z*-axis ($f = 25$ Hz, $A = 10°$). The input flapping angle, Φ, varies over the relative time in the flapping cycle, t/T (a). Spatial contours of the difference between flapping versus flapping and rotating for the tip displacement, Δz (b), normal strain along the *y*-axis, $\Delta\varepsilon_{yy}$ (c), normal strain along the *x*-axis, $\Delta\varepsilon_{xx}$ (d), and shear strain in the *x*-*y* plane, $\Delta\varepsilon_{xy}$ (e) are shown at several snapshots in time (indicated by the filled circles and dotted vertical lines in (a)). Colouring indicates the magnitude of each parameter as indicated by the colour bars on the far left.

APPENDIX 3:
SUPPLEMENTARY MATERIAL FOR LOW-ORDER HALTERE MODEL

DETERMINATION OF SPRING CONSTANTS

To determine the spring constants for bending and torsion, we used the equations for displacement of a beam with an end load and torsion of a beam with a moment applied at the tip. The former is given by

$$F = \frac{3EI_{yy}}{l^3}\delta \tag{A3.1}$$

where F is the applied force at the tip, E is the Young's modulus of the material, I_{yy} is the area moment of inertia, l is the length of the beam, and δ is the deflection. The area moment of inertia of a beam with a circular cross section is given by

$$I_{yy} = \frac{\pi r^4}{4} \tag{A3.2}$$

where r is the radius of the cylinder. The relationship between the force, F, and displacement, δ, is given by

$$F = k_B\delta \tag{A3.3}$$

where k is the spring constant. Thus, we prescribed the spring constant for bending as

$$k_B = \frac{3E\pi r^4}{4l^3}. \tag{A3.4}$$

We know that the natural frequency for such a system is given by

$$\omega_n = \sqrt{\frac{k_B}{M}} \tag{A3.5}$$

where M is the total mass of all of the point masses (we assume the beam is massless). Thus, we set the spring constant to be a function of the natural frequency of the system

$$k_B = M\omega_n^2. \tag{A3.6}$$

On the other hand, for a shaft undergoing torsion, the equation that describes the relationship between a moment applied at the tip, T, and the angle of twist, θ, is given by

$$T = \frac{GJ}{l}\theta \tag{A3.6}$$

where G is the shear modulus and J is the polar moment of inertia. Assuming the beam has a circular cross section, the polar moment of inertia is given by

$$J = \frac{\pi r^4}{2} \tag{A3.7}$$

where r is the radius of the cylinder. In addition, if we assume the beam is homogenous and isotropic, then the shear modulus is given by

$$G = \frac{E}{2(1+\nu)} \tag{A3.8}$$

where E is the Young's modulus and ν the Poisson's ratio of the material. Similar to the derivation for force, the moment, T, is related to the angle, θ by

$$T = k_T\theta. \tag{A3.9}$$

Therefore, the equation for the torsion spring constant is given by

$$k_T = \frac{E\pi r^4}{4l(1+\nu)} = \frac{l^2}{3(1+\nu)}k_B = \frac{Ml^2\omega_n^2}{3(1+\nu)}. \tag{A3.10}$$

VALIDATION

In order to validate our model, we first simulated constant rotations about the z-axis with a flapping frequency equal to and half the natural frequency. We compared our results for the point mass model (figure 5.2b) and the eccentric mass model (figure 5.2c) to those reported previously by Thompson *et al* (2008) (figure S22). In both cases we found that our model was able to exactly reproduce the results from Thompson *et al* (2008).

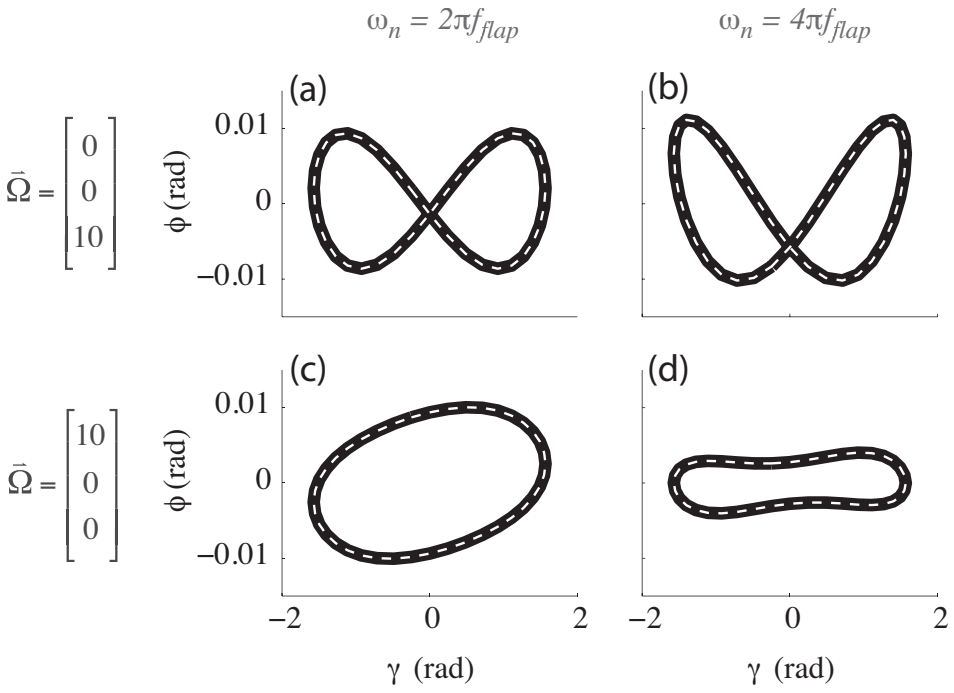

Figure S22. Model validation: out-of-plane displacement, φ, versus input flapping angle, γ, as computed using our haltere model (solid) versus results from Thompson *et al* (2008) (dashed). Similar results were obtained for the COMSOL model (results not shown). Results are shown for four different simulations: flapping at the natural frequency with rotation about the x-axis (roll) (a) or z-axis (yaw) (c), and flapping at half the natural frequency with rotation about the x-axis (b) or z-axis (d) rotations. These results were the same for both the two symmetric mass distributions that we employed: single point mass (figure 6.2b) and symmetric mass (figure 6.2c).

In order to confirm the accuracy of the results from our COMSOL, we examined how the error in the torsion for flapping alone varied with relative tolerance of the solution method (figures S23 and S24). We found that using a relative tolerance of 1e-7 allowed the magnitude of the torsion during flapping alone to converge to less than 1% of the torsion during flapping with rotation (figure S23).

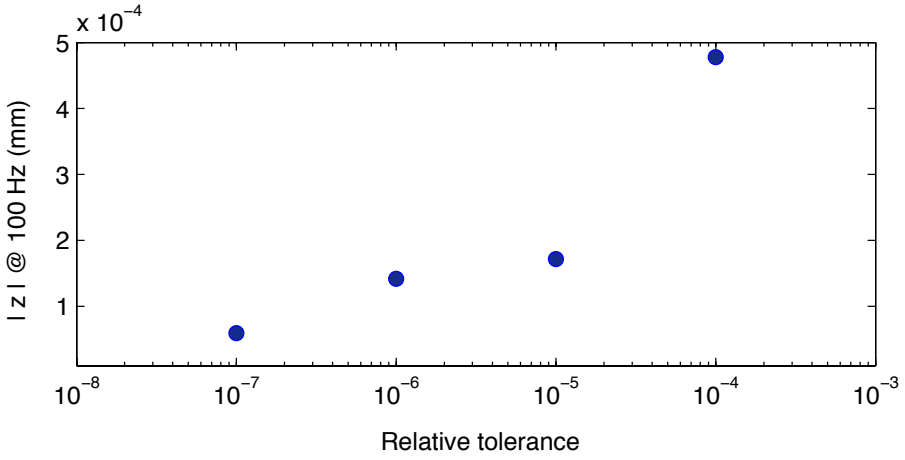

Figure S23. Convergence of COMSOL haltere model as reported by the relative difference in the torsion displacements of the haltere bulb, |z|, at the flapping frequency of 100 Hz versus relative tolerance used for the solution method.

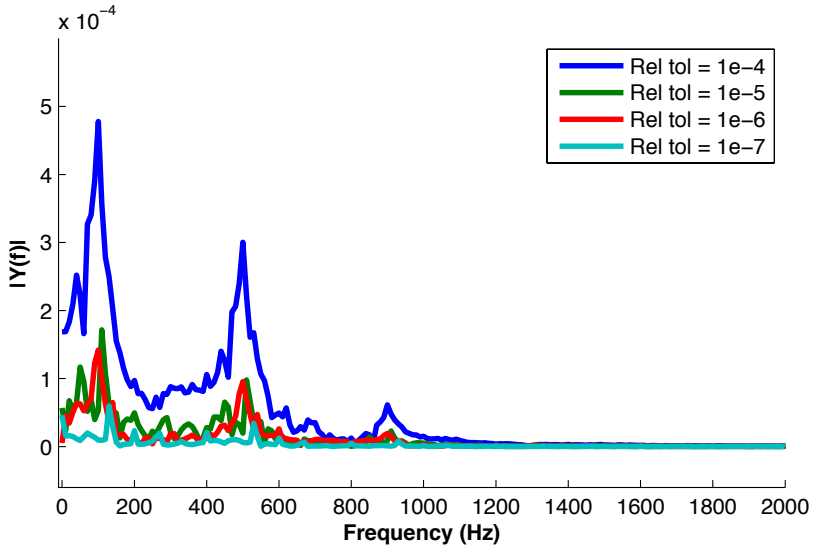

Figure S24. The torsion angle amplitude, |Y(f)|, versus frequency for the COMSOL haltere model under flapping alone. Coloring indicates four different relative tolerances (see inset in upper right). As indicated, the overall response decreases substantially with increasing relative tolerance.

VITA

Annika was born and raised in Denver, Colorado. She moved to California in 2006 to study engineering at Harvey Mudd College. While there, Annika co-founded a chapter of Engineers for a Sustainable World and led two water quality evaluation trips to address issues of brackish water in Kenya and arsenic water treatment in Cambodia. She also worked with Dr. Lori Bassman (Harvey Mudd College) to study the mechanics of plant tendril coiling.

After taking a year off to work at the Boulder Running Company in Colorado, Annika received an NSF Graduate Research Fellowship to start her graduate work in bio-inspired design at the University of Washington. Her research interests include: mechanics of materials, fluid-structure interactions, finite element modeling, renewable energy, and biologically inspired design.

Outside of her graduate research in insect flight and bio-inspired design, Annika is passionate about environmental sustainability. Beyond her experience with Engineers for a Sustainable World, Annika has also worked to forward sustainability efforts on university campuses by performing a sustainability audit of the Claremont Colleges in 2007 and the University of Washington in 2011. In addition to her graduate studies in mechanical engineering, Annika also completed a Certificate in Environmental Management at the University of Washington in 2012.